Politecnico di Milano

Scuola di Ingegneria Industriale e dell'Informazione
Corso di Laurea Magistrale in Ingegneria Fisica

The magnetic phase diagram of the magnetoelectric $EuTiO_3$ studied by neutron powder diffraction

Candidato:
William Capra
Matricola 784300

Relatore:
Prof. Giacomo Claudio Ghiringhelli

Correlatore:
Dott. Claudio Mazzoli

Anno Accademico 2012-2013

The magnetic phase diagram of the magnetoelectric $EuTiO_3$ studied by neutron powder diffraction

William Capra

April 2014

Contents

List of Figures

List of Tables

Abstract

A temperatura ambiente $EuTiO_3$ è una perovskite con un ordinamento magnetico di lungo raggio, che appare al di sotto della temperatura di Néel ($T_N = 5.5$ K). Gli ioni magnetici sono gli atomi di Eu, i cui momenti magnetici si allineano in un un struttura di tipo G. A causa del forte assorbimento dell'europio naturale, gli esperimenti di diffrazione da neutroni risultano estremamente difficoltosi e la qualità dei dati è limitata. Infatti i dettagli della struttura magnetica di $EuTiO_3$ sono stati rivelati solo di recente attraverso diffrazione risonante da raggi X. Al di sotto di T_N $EuTiO_3$ mostra proprietà magnetoelettriche (ME), quali la dipendenza della costante dielettrica dal campo magnetico applicato. I meccanismi microscopici dell'accoppiamente ME sono ancora materia di dibattito. Inoltre una transizione strutturale al di sotto della temperatura ambiente è stata osservata e sulla base misure di magnetometria sono stati sollevati dubbi sulla struttura magnetica determinata attraverso i raggi X. Un nuovo diagramma di fase, che evidenzia uno spin-flop a temperature prossime a T_N, è stato proposto. In questo panorama era necessaria un'indagine sistematica della struttura magnetica di $EuTiO_3$. Questo è lo scopo della tesi e per raggiungerlo si è optato per l'utilizzo della tecnica di diffrazione neutronica da polveri spingendo la tecnica al limite. Per questo le misure sono state realizzate con il diffrattometro ad alta risoluzione D2B a ILL ed un codice per la correzione per assoribimento dei dati è stato sviluppato. I raffinamenti della struttura con il metodo Rietveld, il metodo sperimentale e le strategia di correzione vengono presentati. Sono inoltre discusse l'influenza dell'incertezza sperimentale sulla correzione per assorbimento e le procedure di raffinamento adottate. Sulla base di quanto presentato possiamo affermare che i momenti di spin in $EuTiO_3$ giacciano nel piano (a, b) in tutto l'intervallo di temperature analizzato. Infine vengono discussi i valori del momento magnetico ricavati, più alti rispetto a quelli precedentemente riportati.

Abstract

At room temperature (RT) $EuTiO_3$ is a prototypical perovskite with a long range magnetic order appearing below $T_N = 5.5$ K. The magnetic moments are provided by the Eu ions which arrange in a G-type structure. Due to the strong absorption of natural Eu neutron diffraction experiments on $EuTiO_3$ are difficult, data quality is limited and details of the magnetic structures (moment directions) have been refined only very recently, by resonant x-ray diffraction. Below T_N magnetoelectric (ME) properties appear in the $EuTiO_3$ dielectric constant dependence versus applied magnetic field. Although no long range order of the electric polarisation is realized, in $EuTiO_3$ the microscopic mechanisms source of the ME coupling are still matter of debate. In parallel, a structural phase transition just below RT has been detected and macroscopic magnetic measurements have questioned the magnetic structure deduced by x-rays, proposing a new magnetic phase diagram characterised by a spin-flop state at temperatures close to T_N. Clearly, in this panorama a systematic investigation of the magnetic structure of $EuTiO_3$ by a microscopic technique with great thermal stability was necessary in order to suitably clarify the background for the ME properties development. This is the aim of this thesis. In order to achieve our goal we exploited neutron powder diffraction (NPD) technique as an investigation tool, by pushing the technique to its limits. For this reason specific NPD experiments were performed at the very high-resolution diffractometer D2B of the ILL in a special configuration and a new PYTHON code was develop to finely correct the data. Solution of $EuTiO_3$ structures by Rietveld methods are presented together with the experimental methods employed and the correction strategies developed. An extensive investigation of the influence of absorption correction uncertainties due to experimental parameters and specific procedures implemented are discussed. As a result of our work we can confirm that $EuTiO_3$ spin moments always lies in the a, b-plane over the temperature range investigated. We finally discuss the magnitude of the magnetic moment found higher than the values previously reported.

Prefazione

Le proprietà magnetoelettriche nascono dall'interazione tra i gradi di libertà strutturali, magnetici ed elettrici. Questa interazione tra spin, carica e parametri strutturali apre la via a future possibili applicazioni nei sensori, nelle memorie e nella spintronica. Questo è il motivo per cui la comunità scientifica mostra un grande interesse per la famiglia dei materiali magnetoelettrici. La comprensione delle ragioni microscopiche di tali fenomeni sta spingendo la ricerca con lo scopo di ampliare la conoscenza dei meccanismi di accoppiamento. Questo è un prerequisito per ogni futura applicazione.

Effetti magnetoelettrici possono essere presenti sia in materiali *bulk*, che in film sottili così come in eterostrutture più complesse. Recentemente un crescente interesse è sorto verso il titanato d'europio ($EuTiO_3$). Questo materiale mostra un particolare meccanismo di accoppiamento tra le proprietà dielettriche e quelle magnetiche. La comprensione di questi fenomeni richiede prima di tutto una corretta determinazione della struttura cristallina e magnetica di tale composto, strutture che sono ad oggi materia di dibattito.

Nel capitolo 1 gli aspetti fondamentali dei materiali magnetoelettrici sono presentati e messi in correlazione con la famiglia dei materiali multiferroici, dei quali si introduce la differenza tra propri ed impropri.

Nel capitolo 2 viene discusso il $EuTiO_3$. Questo composto possiede la struttura di una perovskite ed ha un ordinamento antiferromagnetico al di sotto della temperatura di Néel ($T_N = 5.5$ K). Agli inizi degli anni 2000 l'effetto magnetoelettrico è stato osservato sperimentalmente in questo materiale: a basse temperature il valore della costante dielettrica è funzione del campo magnetico applicato. Le proprietà magnetoelettriche sono presentate, mostrando che non solo le proprietà magnetiche possono essere controllate attraverso il campo magnetico, ma anche che la magnetizzazione possa essere controllata attraverso l'applicazione di un campo elettrico.

La struttura del cristallo viene presentata, richiamando che il cristallo sia cubico a temperatura ambiente, mentre appartenga ad un gruppo di spazio tetragonale a basse temperature. La struttura tetragonale in questione, a causa di ragioni di simmetria, è compatibile con due soli ordinamenti

antiferromagnetici: un ordinamento bidimensionale in cui i momenti magnetici giacciono nel piano a, b ed un ordinamento unidimensionale in cui i momenti magnetici giacciono lungo l'asse c.

Diversi autori hanno studiato il problema della determinazione della struttura magnetica della fase antiferromagnetica del $EuTiO_3$. Attraverso l'utilizzo della diffrazione risonante da raggi X, è stato dimostrato che a 2 K i momenti magnetici giacciono nel piano e con la diffrazione neutronica da polveri non sono state notate differenze tra la configurazione a 2 K e quella a 3 K. Altri autori hanno invece utilizzato tecniche macroscopiche, quali misure di magnetizzazione, e proposto un diagramma di fase magnetico più complesso; che contempla l'ordinamento nel piano per temperature inferiori a 3 K e l'ordinamento lungo l'asse c tra 3 K e la temperatura di Néel. Abbiamo di conseguenza deciso di studiare la struttura magnetica a 1.6 K e 3.5 K nell'intento di verificare quale dei due modelli proposti sia corretto a 3.5 K.

Per determinare la struttura cristallina e magnetica del $EuTiO_3$ abbiamo utlizzato la tecnica di diffrazione neutronica da polveri, ma utilizzando un *set-up* sperimentale che permettesse di raggiungere una risoluzione più elevata rispetto a quanto già fatto. La tecnica, presentata nel capitolo 3, permette di determinare la struttura cristallina grazie all'interazione tra i neutroni e le forze nucleari, infatti a causa della loro neutralità i neutroni attraversano un materiale senza interazioni, a meno che non giungano in prossimità dei nuclei e vengano da essi respinti. D'altro canto anche le strutture magnetiche possono essere studiate. Infatti i neutroni posseggono un momento di spin e pertanto possono interagire con il campo magnetico generato dal momento angolare o di spin degli elettroni del cristallo. La teoria dell'interazione nucleare e magnetica viene presentata con lo scopo di ottenere le formule delle *cross-section* di tali interazioni. Le *cross-section* sono strettamente legate alle quantità misurate in un esperimento di diffrazione e contengono le informazioni sulle posizioni degli atomi e sui momenti magnetici. Sono pertanto il collegamento tra ciò che viene misurato e le informazioni strutturali che stiamo ricercando.

I neutroni vengono prodotti attraverso la fissione nucleare (fasci continui) o la spallazione nucleare (fasci pulsati). Gli esperimenti di diffrazione da neutroni qui presentati sono stati svolti all'Istituto Laue-Langevine (ILL) in Grenoble (F). ILL é, nel momento in cui stiamo scrivendo, il più potente reattore nucleare per scopi scientifici al mondo, con più di 50 strumenti.

Viene quindi introdotto il metodo Rietveld. Questo metodo permette di determinare la struttura del composto studiato direttamente dal profilo di intensità dei neutroni diffratti. Si applica direttamente al profilo d'intensità a differenza di altri metodi che richiedono il calcolo delle intensità integrate di ogni riflessione. L'applicazione di questo metodo richiede l'assunzione di un

modello di partenza. Infatti il gruppo di spazio cristallino e le operazioni di simmetria del gruppo di spazio magnetico devono essere dichiarati e, sulla base di questi, il metodo raffina i parametri liberi attraverso un processo di minimizzazione. Questa soluzione è più che adeguata per il nostro caso, in cui la struttura cristallina è nota e due differenti strutture magnetiche devono essere tra loro comparate.

Molte applicazioni sono state sviluppate per il metodo Rietveld qui viene presentato FullProf un programma estremamente versatile sviluppato ad ILL. FullProf è stato scelto, tra il *software* disponibile, anche perchè permette l'introduzione di speciali fattori di correzione, in funzione dell'angolo di *scattering*. Questa possibilità è di estrema importanza nel nostro caso. A causa dell'elevata *cross-section* di assorbimento degli atomi d'europio, il $EuTiO_3$ assorbe fortemente i neutroni. Questo comporta che il segnale di diffrazione sia molto debole e la durata delle misure elevata. Per ovviare a queste difficoltà abbiamo optato per l'utilizzo di un contenitore in cui il campione potesse disporsi a formare un cilindro cavo. Questa soluzione riduce i tempi di conteggio, ma introduce una distorsione nella dipendenza angolare dei picchi di riflessione che non è implementata in FullProf. Di conseguenza abbiamo sviluppato un nuovo codice Python che generasse i fattori di correzione per questa particolare geometria e quindi utilizzato tali fattori per eseguire i raffinamenti. Il codice, i fattori di correzione ed il loro utilizzo vengono presentati.

Nel capitolo 4 il processo di misura ed i risultati sono discussi. Prima di tutto il raffinamento di una misura di diffrazione da polveri da raggi X a temperature ambiente è presentata. Questa misura permette di concludere che a temperatura ambiente la struttura cristallina del campione è coerente con la struttura del $EuTiO_3$ riportata in letteratura. Quindi, attraverso delle misure di caratterizzazione magnetica, vengono identificate la fase antiferromagnetica, la temperature di Néel ed il momento magnetico degli ioni di europio. Dopo queste misure di caratterizzazione, vengono presentati i dati da diffrazione neutronica da polveri ottenuti presso la *beamline* D2B di ILL. Le misure sono state realizzate a 1.6 K e 3.5 K. Come sopra riportato, mentre tutti gli autori concordano sull'ordinamento bidimensionale al di sotto di 3 K, soltanto alcuni fra essi propongono la presenza di un ordinamento monodimensionale tra 3 K e la temperatura di Néel.

I risultati mostrano che, attraverso l'utilizzo della correzione per assorbimento, i raffinamenti Rieltveld possono essere svolti con successo anche in presenza di un forte assorbimento di neutroni. Infatti, prima di tutto, otteniamo un buon accordo tra i dati sperimentali e la struttura cristallografica già determinata con altre tecniche. Secondo, siamo in grado di distinguere tra le due strutture magnetiche proposte, grazie ai fattori di accordo del

raffinamento ed all'analisi di alcune riflessioni significative. Infatti, a 1.6 K, abbiamo trovato, come d'altronde atteso, un miglior accordo tra l'ordinamento bidimensionale e, a 3.5 K, nuovamente l'ordinamento nel piano meglio si adatta ai risultati sperimentali. Pertanto concludiamo che non abbiamo trovato alcun indizio di una configurazione monodimensionale degli spin.

Infine discutiamo a riguardo del modulo del momento magnetico ottenuto attraverso i raffinamenti e della sua dipendenza con la temperatura. Abbiamo trovato che il momento magnetico presenti valori più elevati rispetto a quelli riportati in letteratura. Tuttavia i valori ottenuti sono consistenti con il valore teorico del momento magnetico dello ione di europio Eu^{++} nonché con le misure di magnetometria.

Preface

The magnetoelectric properties derives from the interaction between the structural, electrical and magnetic degrees of freedom. The interplay between the spin, charge and structural parameters paves the way for future applications in sensors, data storage and spintronic. This is why the scientific community shows a great interest in the class of magnetoelectric. The understanding of the microscopical reasons of these phenomena is pushing the research with the purpose of a better knowledge of the coupling system. This is a prerequisite for any application.

The magnetoelectric effects can be observed both in bulk material, in thin films and in complex heterostructures. Recently an increasing interest has been raised on $EuTiO_3$, which shows an unusual coupling between dielectric and magnetic properties. The comprehension of such phenomena requires first of all the determination of the crystallographic and magnetic structure of such system, which is still matter of debate.

In chapter 1 the definitions of multiferroic and magnetoelectric materials are presented, along with a few examples. The distinction between proper and improper multiferroics is outlined.

In chapter 2 we introduce the magnetoelectric $EuTiO_3$. This compound is a perovskite which shows an antiferromagnetic phase under the Néel temperature ($T_N = 5.5$ K). At the beginning of the century magnetoelectric effects in $EuTiO_3$ was observed through the magnetic field dependence of the dielectric constant at very low temperature. The magnetoelectric properties of the compound are then discussed, showing not only that the electrical properties can be controlled via magnetic field, but also the magnetization can be controlled through an applied electric field.

The crystal structure determination is revisited, recalling that the crystal, cubic at room temperature, belongs to a tetragonal space group at low temperature. This low-temperature structure is compatible, due to symmetry reasons, with only two antiferromagnetic spin ordering: a two-dimensional ordering in which the magnetic moments lie in the a, b-plane and a one-dimensional in which the magnetic moments lie along the c-axis.

Different authors studied the problem of the determination of the magnetic structure of the antiferromagnetic phase of $EuTiO_3$. By the use of RXD it has been shown that at 2 K the magnetic moment are *in-plane* and by neutron powder diffraction that the magnetic moment are still *in-plane* at 3 K. Other authors by the use of macroscopic techniques, e.g. dc magnetization and torque magnetometry measurements, proposed a more complicated magnetic phase diagram: a, b-plane ordering below 3 K and c-axis ordering between 3 K and the Néel temperature. We therefore decided to contribute to the discussion investigating the magnetic structure at 1.6 K and 3.5 K, with the intent of deciding which of the two proposed model is correct at 3.5 K.

To solve the crystallographic and magnetic structure of $EuTiO_3$ we decided to use neutron powder diffraction, but with an higher resolution in respect to what previously done. This techniques, presented in chapter 3, allows to determine the crystal structure due to the interaction between the neutrons and the nuclear forces, in fact owing to their neutral electric charge these particles slightly interact with matter. Therefore they almost pass through a crystal without any interaction unless they come really close to the nuclei. On the other hand, also magnetic structure can be determined. In fact neutrons have a spin and therefore can interact with the spin moment of electrons or the magnetic field generated by their motion. The theory of nuclear and magnetic scattering is presented in order to obtain the formula for the cross-section of the diffraction processes. These cross-sections are strictly related, through the form factor, to the quantity actually measured in a scattering experiment and contain the information on the atoms in the system and on their displacements. The cross-sections are therefore the link between what measured and the structural information we are looking for.

Neutrons are obtained through nuclear fission (continuous beam) or spallation (pulsed beam). We performed our experiment at the Institute Laue-Langevine (ILL) in Grenoble (F), which, at the time we are writing, is the most powerful reactor for research purpose with more than 50 instruments.

The Rietveld refinement method is then introduced. This method allows to determine the structure of the compound starting from the diffraction intensity profile of a powder diffraction experiment. It directly applies to the profile intensity instead of other methods dealing with integrated intensity. The application of a such a method requires the assumption of a model. In fact the crystallographic space group and the symmetry operations of the magnetic space group must be defined and then, through a minimization process, the method returns the value of the optimal parameters, within the constrains imposed by the symmetry. This method perfectly applies to our case in which the crystal structure is known and two different magnetic structure have to be compared.

Many applications have been developed for the Rietveld method, here we present FullProf an extremely versatile program developed at ILL. FullProf has been chosen, among the available software, also because it allows to introduce special correction factors as functions of the scattering angle. This tool is fundamental in our case. Due to the large absorption cross-section of europium atoms, $EuTiO_3$ strongly absorbs neutrons. This causes a very weak signal and accordingly high counting time. To overcome this problem we used an annular cylindrical sample holder. This reduces the counting time, but introduces an angular dependence of the scattered peaks which is not implemented in FullProf. Therefore we developed a new Python code to generate the correction factors for such a geometry and then used these corrections factors to perform the refinement. The code, the correction factors and their usage are presented.

In chapter 4 the measurements and the experimental results are outlined. First of all a refinement performed on XPD data at room temperature is presented. This measurement let us conclude that the room temperature crystalline structure of our sample is consistent with $EuTiO_3$ structure reported in literature. Secondly, through a magnetic characterization, we recognize the antiferromagnetic phase, the Néel temperature and the magnetic moment of the europium atoms. After these characterization measurements we present the neutron powder diffraction data collected at the D2B beamline at ILL. The measurements were performed at two different temperature 1.6 K and 3.5 K. As previously discussed, while all the authors agree on a two-dimensional spin ordering below 3 K, only some of them suggest the presence of a one-dimensional spin configuration between 3 K and the Néel temperature.

The results presented show that, by the usage of the absorption correction, Rietveld refinement can be successfully carried out also under strong neutron absorption. In fact, first of all, we obtain a good agreement between the experimental data and the crystallographic structure, which has been already determined with other techniques. Secondly, we are able to distinguish between the two proposed magnetic configuration, due to the agreement factors and to the analysis of the peaks. In fact, at 1.6 K, we found, as expected, a better agreement with the two-dimensional ordering and, at 3.5 K, we again found a better agreement with the *in-plane* ordering. Therefore we conclude that we did not find any evidence of the one-dimensional spin configuration.

Finally we discuss the magnetic moments magnitude, obtained through the refinements, and their temperature dependence. We found magnetic moment's values higher than those reported in literature, but consistent with the theoretical value of the magnetic moment of europium ion Eu^{++} and the

magnetometry measurements.

Chapter 1

Multiferroics and magnetoelectrics

1.1 Multiferroics

If a magnetic field is applied to a material, this can show three different types of response. The material is called diamagnetic if the applied magnetic field induces a magnetic field within the material which is antiparallel to the applied field itself. This contribution is added to the external field thus reducing the total magnetic field in the material. The material is called paramagnetic if the total magnetic field within the material is higher with respect to the applied field. This is due to a magnetization which induces a magnetic field parallel to the applied one. The material is called ferromagnetic if it is capable to show a magnetization also without any applied magnetic field and the magnetization can be switched hysteretically by an applied magnetic field.

Similar behaviour can be shown also by electric field and electrical polarization. In the presence of an electric field an electric polarization is produced into a neutral crystal. The positive and negative charges within the material are separated and a dipolar moment is induced. In the regime of small applied electric field the polarization induced can be proportional to the field itself and along the same direction of the applied field. If the polarization is antiparallel to the external field the material is called dielectric. If the polarization is parallel to the external field the material is called paraelectric. A material is called ferroelectric if it shows a spontaneous polarization also in absence of an external electric field and if an external electric field is capable to reverse the polarization. These behaviours are formally similar to the magnetic behaviours of material.

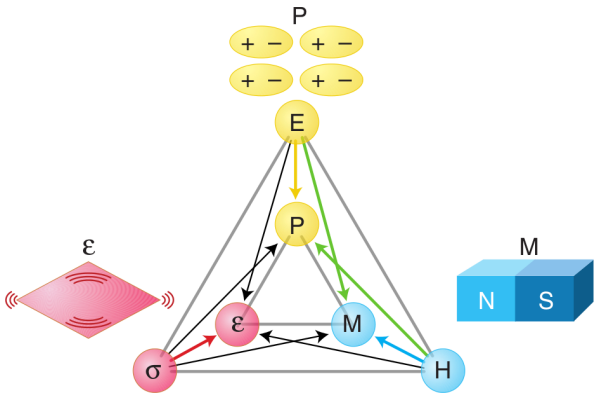

Figure 1.1: Phase control in ferroics and multiferroics. The electric field E, magnetic field H, and stress σ control the electric polarization P, magnetization M and strain ϵ, respectively. In a ferroic material, P, M or ϵ are spontaneously formed to produce ferromagnetism, ferroelectricity, or ferroelasticity, respectively. In a multiferroic, the coexistence of at least two ferroic forms of ordering leads to additional interaction. In a magnetoelectric multiferroic, a magnetic field may control P or an electric field may control M (green arrows). Figure from Ref. [10].

It is important to point out the relation existing between the ferroelectric properties and the crystal structure. In fact the lack of a centre of inversion is a necessary condition for the ferroelectric order to develop. Let us consider a crystal with an inversion symmetry, in which the point $A = (x, y, z)$ is transformed, under the inversion symmetry, into the point $A' = (\bar{x}, \bar{y}, \bar{z})$. If any polarization is present at the position A, an equal and opposite polarization will be present at the position A' resulting in a net contribution to polarization equal to zero[9]. Because this holds for each point within the unit cell, the net polarization of such a cell will be zero, and null will be the polarization of the whole crystal. Although the absence of inversion symmetry is a necessary condition for ferroelectricity, it is not a sufficient condition.

Ferroelectricity and ferromagnetism belong to the so called *ferroics* properties. Also ferroelasticity, which is the capability of a system to display a spontaneous deformation that is stable and can be switched hysteretically by an applied stress, is a ferroic property. Many ferroelectrics are also ferroelastic. That is because a change in their polarization is accompained by a change in their shape. Such materials, which combine two or more ferroic properties (see figure 1.1) in the same phase, are known as multiferroics.

Trend toward device miniaturization hs led to increased interest in combining electronic and magnetic properties into multifuncional materials, so that a

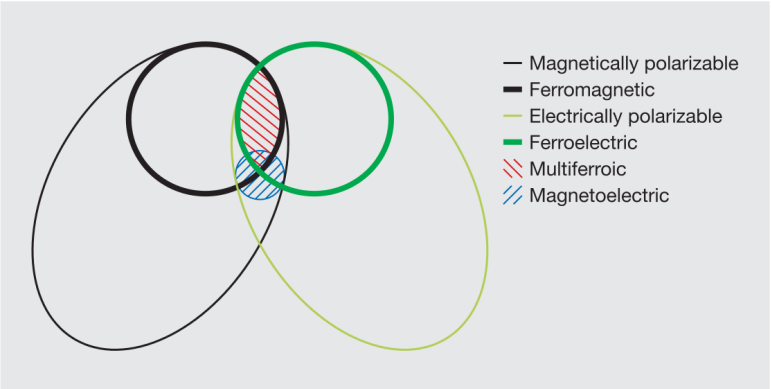

Figure 1.2: The relationship between multiferroic and magnetoelectric materials. Ferromagnets (ferroelectrics) form a subset of magnetically (electrically) polarizable materials such as paramagnets and antiferromagnets (paraelectrics and antiferroelectrics). The intersection (red hatching) represents materials that are multiferroic. Magnetoelectric oupling (blue hatching) is an independent phenomenon that can, but need not, arise in any of thhe materials that are both magnetically and electrically polarizable. Figure from Ref. [11].

single device component can perform more than one task. Ferromagnetic ferroelectric multiferroics are particularly appealing not only because they have the properties of both parent compounds, but also because interaction between the magnetic and electric polarization leads to additional functionalities. For example, the magnetoelectric effect (the induction of a magnetization by an electric field, or of a polarization by a magnetic field) could yield entirely new device paradigms, such as electric field-controlled magnetic data storage.

In figure 1.2 the overlap between ferroic and magnetoelectric properties is shown. On one hand the existence of ferromagnetic and ferroelectric orders in the same compound does not mean that this orders are necessarily coupled. On the other hand, magnetoelectric effect can occur also in material that are neither ferromagnetic or ferroelectric. This is, for example, the case of $EuTiO_3$ which is a paraelectric antiferromagnet.[1]

1.2 Magnetoelectric effect

The coupling between magnetism and electric conduction in metals gives rise to various interesting phenomena, such as colossal magnetoresistant in

[1]Structure and properties of $EuTiO_3$ will be presented in chapter 2.

perovskite maganites[12]. In this class of compounds, itinerant carriers are strongly coupled with localized spin by Hund coupling and the properties of itinerant carriers, such as their effective mass, depend on the configuration of the localised spins. In such a situation, electric conduction can be controlled by magnetic field via the coupling with localised spins, leading to large negative magnetorestistance. In a similar manner, the coupling between magnetism and dielectric properties in magnetic insulators would be possible where the dielectric properties depend on the configuration of localised spins and the dielectric constant can be controlled by magnetic field via the coupling with localised spins. The mutual control of electric and magnetic properties is of fundamental importance and significant interest for application in magnetic storage media and spintronics.

The magnetoelectric effect was first presumed to exist by Pierre Curie[13], and subsequently attracted a great deal of interest in the 1960s and 1970s. In 1957, the magnetoelectric effect was predicted to occur in Cr_2O_3[14] and then, in the 1960s, was experimentally observed[15] below the Néel temperature of 307 K.

The magnetoelectric effect is traditionally described[16] in Landau theory by writing the free energy F of the system in terms of an applied field $\boldsymbol{H}$, whose i-th component is denoted H_i, and an applied electric field $\boldsymbol{E}$, whose i-th component is denoted E_i. Let us consider a non-ferroic material where both the temperature-dependent electrical polarization $P_i(T)$ and the magnetization $M_i(T)$ are zero in the absence of applied fields and there is no hysteresis. The free energy for an infinite, homogeneous and stress-free medium can be written as

$$\begin{aligned} -F(E,\, H) &= \frac{1}{2}\epsilon_0\epsilon_{ij}E_iE_j + \frac{1}{2}\mu_0\mu_{ij}H_iH_j + \alpha_{ij}E_iH_j + \\ &\quad + \frac{\beta_{ijk}}{2}E_ih_jH_k + \frac{\gamma_{ijk}}{2}H_iE_jE_k + \ldots \end{aligned} \tag{1.1}$$

The first term on the right hand side describes the contribution resulting from the electrical response to an electric field, where the permittivity of free space is denoted ϵ_0, and the relative permittivity $\epsilon_{ij}(T)$ is a second-rank tensor that is typically independent of E_i in non-ferroic materials. The second term is the magnetic equivalent of the first term, where $\mu_{ij}(T)$ is the relative permeability and μ_0 is the permeability of free space. The third term describes linear magnetoelectric coupling via α_{ij}; the third-rank tensor $\beta_{ijk}(T)$ and $\gamma_{ijk}(T)$ represent higher-order magnetoelectric coefficients.

In the present scheme, all magnetoelectric coefficients incorporate the field independent material response functions $\epsilon_{ij}(T)$ and $\mu_{ij}(T)$. The magnetoelectric effect can then easily be established in the form $P_i(H_j)$ or $M_i(E_j)$. The

former is obtained by differentiating F with respect to E_i, and then setting $E_i = 0$. A complementay operation involving H_i establishes the latter. One obtains

$$P_i = \alpha_{ij} H_j + \frac{\beta_{ijk}}{2} H_j H_k + \dots \tag{1.2}$$

and

$$\mu_0 M_i = \alpha_{ji} E_j + \frac{\gamma_{ijk}}{2} E_j E_k + \dots \tag{1.3}$$

In ferroic materials, the above analysis is less rigorous because $\epsilon_{ij}(T)$ and $\mu_j(T)$ display field hysteresis.

A multiferroic that is ferromagnetic and ferroelectric is liable to display large linear magnetoelectric effects. This follows because ferroelectric and ferromagnetic materials often (but not always) possess a large permittivity and permeability respectively, and α_{ij} is bounded by the geometric mean of the diagonalised tensors ϵ_{ii} and μ_{jj} such that

$$\alpha_{ij}^2 \leq \epsilon_0 \mu_0 \epsilon_{ii} \mu_{jj} \tag{1.4}$$

Equation 1.4 is obtained from equation 1.1 by forcing the sum of the first free terms to be grater than zero, that is, ignoring higher-order coupling terms. it represents a stability condition on ϵ_{ij} and μ_{ij}, but if the coupling becomes so strong that it drives a phase transition to a more stable state, then α_{ij}, ϵ_{ij} and μ_{ij} take on new values in the new phase.

The nonlinear magnetoelectric coupling appears when the material have small values of either ϵ_{ij} or μ_{ij} or both, so the linear magnetoelectric effect will also be small, given equation 1.4. However, no such restriction applies to higher-order couplings, such as those described by β_{ijk} and γ_{ijk}. For example, in some materials term such as $\beta_{ijk} H_j H_k$ can dominate the linear term $\alpha_{ij} H_j$ in equation 1.2, as first shown experimentally at low temperatures in the piezoelectric paramagnet $NiSO_4 \cdot 6H_2O$[17].

So far, our discussion of linear and higher-order magnetoelectric coupling has ignored the effects of strain (indirect magnetoelectric coupling). Such effects could be significant or even dominant. For example, the inclusion of piezomagnetism[2] or magnetostriction[3] would generate cross terms in equation 1.1 that are proportional to strain and depend by H_i. Analogous expression would arise from piezoelectricity or electrostriction. Furthermore, mixed terms involving products of strain, H_i and E_j have been predicted[18].

[2]Piezomagnetism describes a change in strain as a linear function of applied magnetic field, or a change in magnetization as a linear function of applied stress.

[3]Magnetostriction describes a change in strain as a quadratic function of applied magnetic field.

1.3 Proper and improper multiferroics

We can know better investigate the relationships between ferroics properties and magnetoelectric effect. Most ferroelectrics are transition metal oxides, in which the transition ions have empty d shells (d^0). These positively charged ions like to attract one (or several) of the neighbouring negative oxygen atoms. This collective shift of cations and anions inside a periodic crystal induces bulk electric polarization. The mechanism of the covalent bonding (electron pairing) in such molecules is the virtual hopping of electrons from the filled oxygens shell to the empty d shell of a transition metal ion. Magnetism, on the contrary, requires transition metal ions with partially filled d shells, as the spins of electrons occupying completely filled shells add to zero and do not participate in magnetic ordering. The exchange interaction between uncompensated spins of different ions, giving rise to long range magnetic ordering, also results from the virtual hopping of electrons between the ions. In this respect the two mechanism are not so dissimilar, but the difference in filling of the d shells required for ferroelectricity and magnetism makes these two ordered states mutually exclusive, this is the so called "d^0 paradigm"[19].

This essentially prevents the two conditions to be fulfilled on the same ion, for example the B site of a perovskite structure (ABO_3.) Therefore in a large number of compounds the electric and magnetic ordering are associated with different ions in the unit cell, these compounds are called *proper* multiferroics. For example compounds, such as $BiMnO_3$ or $BiFeO_3$, with magnetic Mn^{3+} and Fe^{3+} ions, are ferroelectric. Here, however, it is the Bi ion with two electrons in the $6s$ orbital that moves away from the centrosymmetric position in its oxygens surrounding inducing the polarization[20]. $BiMnO_3$ shows a ferroelectric transition at $T_{FE} \sim 800$ K and a ferromagnetic transition at $T_{FM} \sim 110$ K, below which the two orders coexist[21]. $BiFeO_3$ shows both electric and magnetic ordered phases above room temperature. However because the ferroelectric and magnetic and magnetic orders in these materials originate in physically different part of the cell, the coupling between them is weak. In the case of $BiMnO_3$ the dielectric constant ϵ shows only a minute anomaly at T_{FM} and is fairly insensitive to magnetic fields: even very close to T_{FM} the change in ϵ produced by a 9 T field does not exceed 0.6%[19].

Nowadays both experimental[22] and theoretical[23] work have relaxed the so called "d^0 paradigm". Interestingly, strong magnetoelectric effects is not forbidden in d^0 pervoskite oxides when A site contributes to magnetism (typically by a rare earth). This is, for example, the case of $EuTiO_3$.

On the other hand, if the polarization is only a part of a more complex lattice distortion or if it appears as an accidental by-product of some other ordering, the ferroelectricity is called *improper*. For example, the hexagonal

manganites $RMnO_3$ (R = Ho-LU, Y) show a lattice transition which enlarges their unit cell. An electric dipole moment, appearing below this transition is induced by a nonlinear coupling to nonpolar lattice distortions, such as the buckling of R-O planes and tilts of manganese-oxygens bipyramids (geometric ferroelectricity)[24, 25]. Although fascinating from the fundamental point of view, these materials have very limited applications due to their extremely low ordering transition temperature and/or tiny electric polarization.

Another group of improper multiferroics are charge-ordered insulators. In many narrowband metals with strong electronic correlations, charge carriers become localised at low temperature and form periodic superstructures. An example is Fe_3O_4, which undergoes a metal-insulator transition at $T \sim$125 K with a complex pattern of ordered charges of iron ions[26]. When charges order in a non-symmetric fashion, they induce electric polarization.

1.4 Two-phases magnetoelectrics

The single-phase multiferroics, described so far, are very attractive for the understanding of the mechanism leading to magnetoelectric coupling. However these material do not combine large and robust electric and magnetic polarization at room temperature. This difficulties can be overcome through the two-phase magnetoelectric system, which will not be studied in this thesis but are here presented for completeness.

In these materials the coupling between the magnetic and electric properties is made indirectly, via strain[27]. For example, the coupling can be done by forming two-phase composite multiferroics that consist of a ferroelectric constituent (such as $PbZr_{1-x}Ti_xO_3$) and a ferromagnetic constituent (such as $Tb_{1-x}Dy_xFe_2$)[28]. In such composites, the magnetoelectric effect arises from the interaction of the elastic components of the ferromagnetic and ferroelectric constituents. For instance, an electric field induces strain in the ferroelectric; this strain is passed on the ferromagnet, where it causes magnetization. The magnetoelectric effect is large if the coupling at the interface is large; therefore, composites with large surface area (such as multilayered thin films) and strongly ferroelastic constituents are particularly effective.

Chapter 2

Europium Titanate

2.1 Magnetoelectricity in $EuTiO_3$

$EuTiO_3$ belongs to the tetravalent perovskite titanates ($ATiO_3$) family. The rare earth ion produces a long range magnetic ordering at very low temperature. On the other hand no spontaneous polarization has been observed. This lack of a bulk polarization has been propose to be due to zero-point vibrations of ions. Therefore $EuTiO_3$ is a quantum paraelectric system. Although $EuTiO_3$ has been known as a G-type antiferromagnet below $T_N = 5.5$ K since the 1960s[29], its magnetoelectric properties were only revealed in 2011 by 7% drop in the dielectric constant at T_N under an applied magnetic field[30]. The presence of the magnetoeletric effect in $EuTiO_3$ have been studied by Wu and Shen[1]. Their model, in accordance with experimental data, has demostrated magnetoelectric effect by the mutual dependence of electric and magnetic properties. This dependence is revealed by the variation of the electric-field-induced polarization with the applied magnetic field as well as the change of magnetic-field-induced spin moments under the application of an electric field.

In figure 2.1 the variation of the dielectric properties of $EuTiO_3$ under applied magnetic field are shown. The filled square in figure 2.1(a) represents the experimental values of the dielectric constant at different temperature and magnetic field. In absence of the magnetic field, the dielectric constant shows a sharp decrease due to the antiferromagnetic ordering below the Néel temperature. For increasing magnetic fields the dielectric constant at low temperature gradually increases and the phase transition indicated by the sharp peak occurs at lower temperature and eventually disappers. In figure 2.1(b) the dielectric constant is depicted as a function of the magnetic field at 2 K. The variation of the dielectric properties is coherent with the presence of

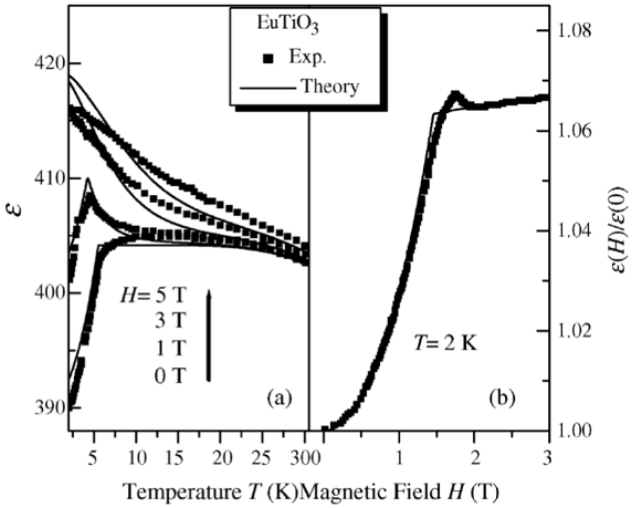

Figure 2.1: (a) Temperature-dependent dielectric constant at 1 kHz in $EuTiO_3$ under various magnetic field. (b) The normalized magnetic field dependence of the dielectric constant to the zero field value in $EuTiO_3$ at 2 K. The experimental data are shown by filled squares and the theoretical reasults by solid curves. Figure from Ref. [1].

an antiferromagnetic ordering. In fact the dielectric constant increases with the magnetic field up to 7%, until the field reaches the saturation value of around 1.5 T, and the antiferromagnetic ordering is completely destroyed. The continous line in figure 2.1 are calculated by a theoretical model for diluited magnetic quantum paraelectric by considering a proper coupling mechanism as presented in Ref [31]. Because the model proposed well reproduces the experimental data, the authors used this model to further investigate the magnetoelectric effect in $EuTiO_3$. If the variation of the dielectric constant due to the magnetic field has been shown, results reported in figure 2.2 (a) and 2.2 (b) manifest the variation the magnetization as a function of the applied electric field, for different values of external magnetic field. The results presented have been calculated for 2 K. In the left panel of figure 2.2 the electric field profile of the spin moment along z-axis ($\langle S_z \rangle$) is shown, whereas in the centre panel the profiles are reported normalised to their values for zero electric field. The magnetization does not show any electric field dependence in two case: zero magnetic field, and saturation magnetic field. In the first case the antiferromagnetic ordering remains unperturbed by the electric field and the magnetization is zero, whereas in the second case the spin parallel alignement remained unperturebated by the electric field and

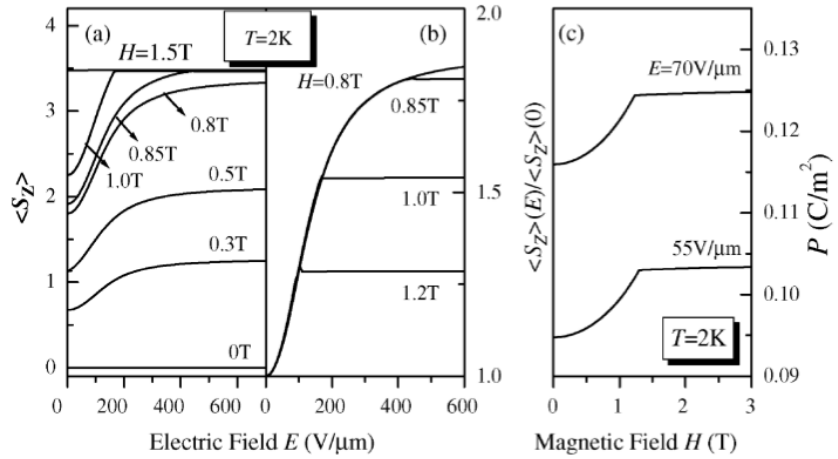

Figure 2.2: (a) Electric-field dependence of the spin momentum along z-axis under various magnetic fields at 2 K. (b) The normalised electrical field dependence of the magnetization to the zero field value in various magnetic field at 2 K. (c) Magnetic-field dependence of the electric-field-induced polarization in $EuTiO_3$ at 2 K. Figure from Ref. [1].

the magnetization is saturated. In the other cases the magnetization is not null for zero electric field and increseas with it, approaching a saturation value which depends by the applied magnetic field. If the magnetic field is greater than 0.85 T the magnetization saturation value is coherent with the parallel alignement of the magnetic moment. In such a case the saturation occurs for an applied electric field of around 400 V/μm. This effect can be explained taking into account the nature of antiferromagnetic ordering in $EuTiO_3$. The presence of a magnetic ground state in this oxide is due to the superexchange interaction. The exchange interaction, which minimizes the energy of the system by the arising of an antiferromagnetic ordering, is not direct, but it is mutuated by the oxigen atoms, through the mediation of their 2p state. Therefore under electrical field parallel to the magnetic field, O ion will be displaced from its equilibrium, resulting in the reduction of the antiferromagnetic coupling, which is proportional to the square of the electric polarization. As a result, except for the ferromagnetic ordering induced by the saturation magnetic field, an additional electric-field-induced ferromagnetic ordering will appear and increase with the electric field due to the antiferromagnetic exchange energy reduction as a consequence of the increasing polarization.

As shown in figure 2.2 (b), at low magnetic field (below 0.85 T), it is

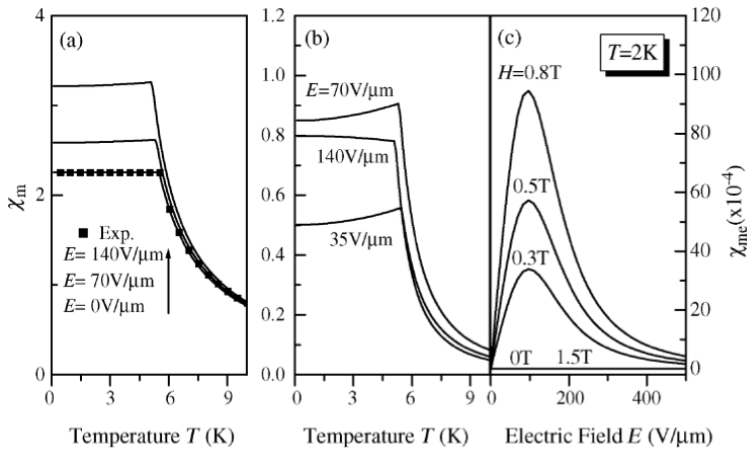

Figure 2.3: Temperature dependence of (a) the magnetic susceptibility χ_m and (b) the magnetoelectric susceptibility χ_{me} under various electric fields. (c) Electric-field dependence of the magnetoelectric susceptibility χ_{me} under various magnetic fields at 2 K. Figure from Ref. [1].

clearly that the magnetization, almost independent of magnetic field, will be significantly enhanced under an applied electric field. However, above 0.85 T, the normalised magnetization decreases with increasing magnetic field due to the saturation of magnetization favoured by the electric field and off course become constant for $H > 1.5\,T$. The results presented provide clear evidence that the magnetization in $EuTiO_3$ can be controlled by the electric fields.

In addition to the dielectric properties, tha magnetic field has an effect on the electric-field-induced polarization in the presence of applied electric field, as shown in figure 2.2 (c). Therefore the results given in figure 2.2 give clear evidence fo the magnetoelectric coupling in the magnetic quantum paraelectric $EuTiO_3$ system. Finally Wu e Shen discuss the magnetoelectric effect in $EuTiO_3$ in relation with the magnetic field, electrical field and temperature. Figure 2.3 (a) and (b) shows the temperature dependance of the magnetic suceptibility χ_m and magnetoelectric susceptibiliy χ_{me} under various electric fields. The magnetoelectric susceptibility is given by

$$\chi_{me} = \frac{\partial \langle S_Z \rangle}{\partial E} \tag{2.1}$$

The experimental magnetic susceptibility without the electric applied field [30] has been depicted in figure 2.3 (a). The model proposed well reproduces the experimental data and can predict the magnetic susceptibility behaviour in different circumstances. In case of applied electric field, the Néel temperature,

evidenced by the rapid change of susceptibility, is shifted to lower values and the susceptibility of the antiferromagnetic phase is increased. This can be explained by the fact that the antiferromagnetic ordering will exist in narrow temperature ranges due to the reduction of the antiferromagnetic coupling, which consequently favors the ferromagnetic ordering parallel to the magnetic field. This reduction is again caused by the electric-field-induced polarization which displaces the oxigen atoms from their equilibrium position.

The magnetoelectric susceptibily which is represented in figure 2.3 (b) shows an interesting behaviour. Above T_N, the magnetoelectric effect tends to vanish, indicating that the thermal perturbation will cause a disordered spin arrangement and an evident decrease of the magnetoelectric effect. Beside that, magnetoelectric susceptibility in the antiferromagnetic phase does not display monotonic behaviour with the applied electric field. In the (c) panel of figure 2.3 the electric-field dependence magnetoelectric susceptibility is investigated under various magnetic fields at 2 K. For 0 T the system does not show any magnetoelectric effect. With increasing magnetic field the effect arises and vanishes again for field approching the saturation magnetic field (1.5 T). On the other hand, for a fixed magnetic field (nor zero or the saturation field), the magnetoelectric susceptibility shows a maximum in function of the applied electric field. This effect is the result of the competition between the electrical polarization and the dielectric susceptibility. The increasing electric field enhances the electrical polarization, which increases the magnetoelectric response. But further increase of the electrical field will decrease the dielectric susceptibility, reducing the magnetoelectric effect.

$EuTiO_3$ can also be deposited as high quality epitaxial films [32], which is a prerequisite for any pratical application in functional devices. Moreover $EuTiO_3$ was predicted to exhibit strong ferromagnetism (sponstaneous magnetization of around 7 μ_B per Eu ion) and strong ferroelectricity (spontaneous polarization of around 10 μC cm^{-2}) simultaneously under large biaxial compressive strain [33]. These values are orders of magnitude higher than those of any known ferroelectric ferromagnet and rival the best materials that are solely ferroelectric or ferromagnetic. Lee *et al.* in absence of a suitable substrate to provide the desired compressive strained, turned to tensile biaxial strain and showed both theoretically and experimentally the emergence of a multiferroic state with such a low strain required to be compatible with the growth of thick high-quality crystalline film [34].

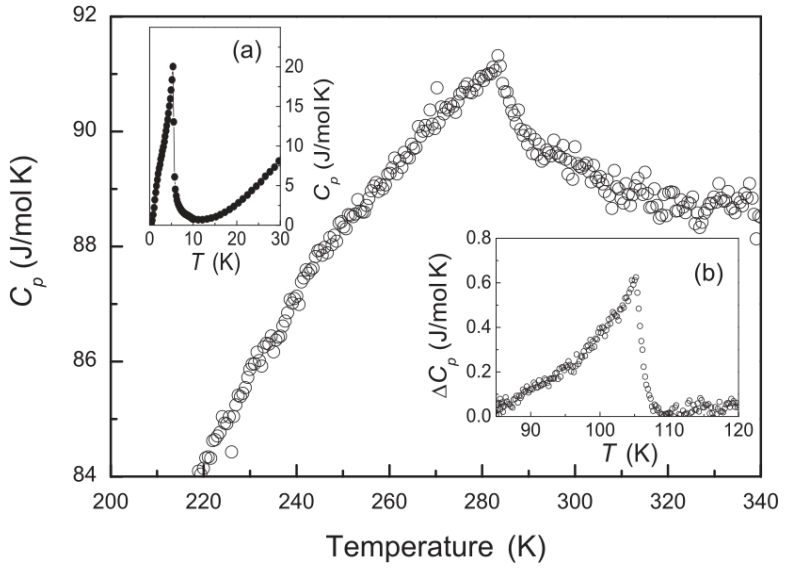

Figure 2.4: Specific heat of $EuTiO_3$ as a function of temperature in the temperature range around thhe phase transition. The insets shows (a) the low temperature region around T_N and (b) the specific heat anomaly ΔC_p of $SrTiO_3$ around the 105 K transition. Figure from Ref. [2].

2.2 Crystallographic Structure

At room temperature, $EuTiO_3$ is isostructural to $SrTiO_3$ (cubic space group $Pm\bar{3}m$, with lattice parameter $a = 3.905$ Å[35, 36]). The cubic cell lattice parameter of $EuTiO_3$ is $a = 3.904$ Å[37]. In this cell the Wickoff position of the atoms are: Ti on $1a$ (0, 0, 0), Eu on $1b$ ($\frac{1}{2}$, $\frac{1}{2}$, $\frac{1}{2}$) and O on $3d$ ($\frac{1}{2}$, 0, 0). Recently Bussmann-Holder *et al.* reported of a structural transition around 280 K[2]. In figure 2.4 the specific heat measurements are reported. The anomaly, which is clearly visible at $T_A = 282(1)$ K, suggests that $EuTiO_3$ undergoes to a cubic-to-tetragonal transition at such a temperature, as $SrTiO_3$ does at $T_c = 106$ K. In the insect (b) is reported, for comparison, the variation of the specific heat of $SrTiO_3$. In insect (a) is reported the specific heat of $EuTiO_3$ near the Néel temperature, clearly identifying the transition to the antiferromagnetic phase. Among the possible mechanism for the structural transition Allieta *et al.*[3] proposed the tilting of corner-linked BO_6 octahedral units[38, 39]. The authors searched among the subgroups of the high-temperature cubic group and found consistent with simmetry constrains and X-rays powder diffraction data only the space group $I4/mcm$[3]. In this group the Wickoff position of the atoms are: Ti at $4c$ (0, 0, 0), Eu at $4b$ (0, $\frac{1}{2}$, $\frac{1}{4}$), O1 at $4a$

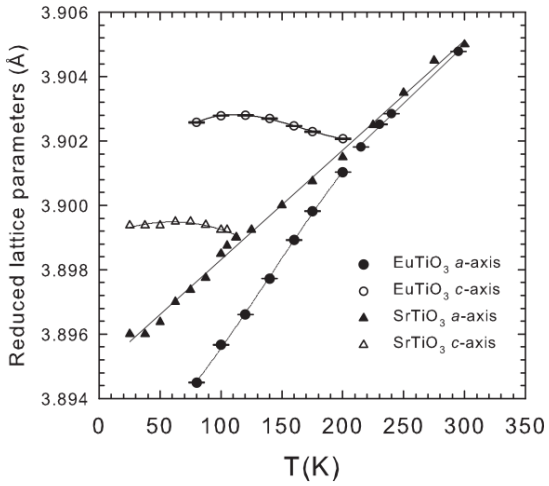

Figure 2.5: Reduced lattice parameters of $EuTiO_3$ and $SrTiO_3$ as a function of temperature. The full and opened circles are the a and c axes of $EuTiO_3$. Full and opened circles are the a- and c-axis values of $SrTiO_3$. The continous lines are guides to the eye. Figure from Ref. [3].

(0, 0, $\frac{1}{4}$), and O2 at $8h$ (x, $x + \frac{1}{2}$, 0) with $x \sim \frac{1}{4}$. In figure 2.5 the reduced lattice parameters of $EuTiO_3$ and $SrTiO_3$ are reported. From the Rietveld analysis of XPD data the authors conclude that a transition takes place at $T^* \sim 235$ K and proposed that the difference between T^* and T_A is due to the correlation length scale evolution of the structural phase transition. In fact the outcome of the PDF analysis at 240 K shows how the correlation length of the tetragonal $I4/mcm$ phase remains confined at the nanoscopic scale (~ 20 Å). At the same temperature the XPD data imply that the structure is cubic. The proposed explanation implies that the tilting of the octahedra changes randomly from one nanoregion to the adjacent one. Anyhow all the measurements agree on the fact that at very low temperature, as in the region in which the antiferromagnetic ordering appears, the transition is completed and the symmetry of the crystal belongs to tetragonal $I4/mcm$ space group. The crystal structure is reported in figure 2.6.

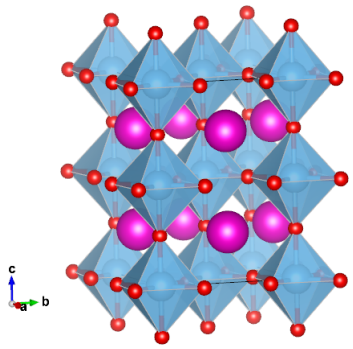

Figure 2.6: $EuTiO_3$ crystal structure. Oxygen atoms are depicted in red, within the oxygens octaedra in blue the titanium atoms, europium ones are in magenta.

2.3 Magnetic structure

2.3.1 Low temperature scattering results

Assumed that at very low temperature the crystallographic structure of $EuTiO_3$ belongs to tetragonal space group $I4/mcm$, Scagnoli *et al.*[4] performed a symmetry analysis using the method of Bertaut[40], as implemented in the BASIREPS program[41], to determine which magnetic configuration is compatible with the given space group. Through the Rietveld refinement of a neutron powder diffraction pattern[1] performed above and under the Néel temperature, the authors found the crystal structure consistent with the reported space group. Under the Néel temperature they observed the magnetic reflections. Those peaks was found consistent with the propagation vector $\boldsymbol{k} = (0, 0, 0)$. This information, together with the localization of the magnetic moment on the Eu ion located at the $4b$ Wyckoff position $(0, \frac{1}{2}, \frac{1}{4})$, allowed to perfomed the Bertaut analysis. The result was that only two antiferromagnetic ordering (irreducible representations) are allowed by Wyckoff position of europium atoms in space group $I4/mcm$, with (0, 0, 0) propagation vector: Γ^6 and Γ^9. Γ^6 is a representation of a one dimensional ordering, in which the magnetic moments lie along th c-axis, whereas Γ^9 is a representation of a two dimensional ordering, in which the magnetic moments lie in the a, b-plane. Both the proposed configurations are G-type configurations. In this type of antiferromagnets starting from one of the magnetic atoms and moving to the nearest neighbors the spin direction is always opposite. By neutron powder

[1]Neutron powder diffraction experiment and Rietveld refinement method are presented in chapter 3.

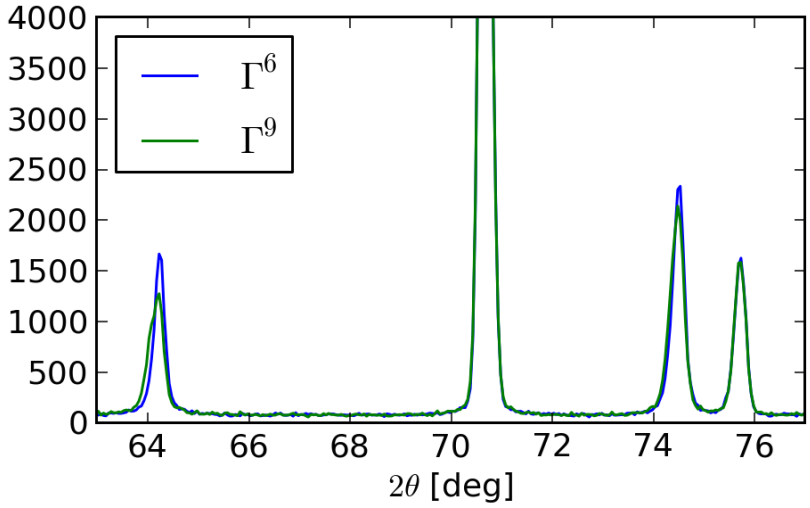

Figure 2.7: Simulation of the neutron diffraction pattern of $EuTiO_3$, the profiles for the two proposed magnetic structure are reported, a focus on the region in which the two differ is shown.

diffraction experiment it is in general possible to distinguish between the two ordering because the magnetic scattering depends on the angle between the magnetic moment and the scattering vector, especially it occurs only if the scattering vector has a component perpendicular to the magnetic moment directon. As an example, the absence of a $(00l)$ reflection would suggest the c-axis ordering, whereas its presence would suggest the a, b-plane ordering. Vice versa, the absence of a $(hk0)$ reflection would suggest the a, b-plane ordering, whereas its presence would suggest the c-axis ordering. Unfortunately the reflections belonging to both $\{00l\}$ and $\{hk0\}$ are forbidden by the space group. The refinement of the neutron powder diffraction data with both the proposed structure did not lead to a final conclusion. The difference between the neutron diffraction pattern expected from the two structure is very little, and it is restricted to the position of the Bragg reflections around 64° and 74° as clearly by the simulation shown in figure 2.7. The resolution provided by the experimental set-up used was not high enough.

To resolve the structure different techniques are available: very high-resolution neutron powder diffraction, neutron single crystal diffraction and resonant X-rays diffraction. Scagnoli *et al.* decided for a RXD experiment.

The magnetic cross-section for X-rays scattering is very weak, but nowadays with synchrotron radiation the magnetic scattering is a widely used

technique, especially in its resonant version. When the incoming photons have an energy resonant with the energy of one of the atomic transitions of the element of the sample, the attention can be focused on a particular electronic shell. In this conditions the atomic scattering factor shows its tensorial nature allowing the appearance of forbidden reflection in non-symmorphic space groups. Therefore the technique has a high sensitivity to the symmetry of the shell investigated. In suitable conditions, focusing on the outer electronic shell, the magnetic properties of the compound studied can be determined. The magnetic sensibility of the resonant diffraction is clearly expressed by the resonant X-rays cross section for the dipole-dipole transition

$$f^{E1}_{\boldsymbol{\epsilon}',\boldsymbol{\epsilon}} = (\boldsymbol{\epsilon}' \cdot \boldsymbol{\epsilon}) F^{(0)} - \mathrm{i}(\boldsymbol{\epsilon}' \times \boldsymbol{\epsilon}) \cdot \hat{\boldsymbol{z}}_n F^{(1)} \tag{2.2}$$

where the first term corresponds to the charge contribution and the second to magnetic diffraction. $\hat{\boldsymbol{z}}_n$ is a unit vector in the direction of the magnetic moment of the n-th ion, and $\hat{\boldsymbol{\epsilon}}$, $\hat{\boldsymbol{\epsilon}}'$ represent the polarization of the incoming and scattered X-rays beam, respectively. In the case of study advantages had been taken by the enhancement of the forbidden reflections arising from tuning the X-rays energy to the Eu L_2 edge (7.612 keV). At this energy a $2p$ electron is excited to the $5d$ empty states and reemits a photon in the decay process. This excitation is sensible to the magnetic motif of the Eu ions due to the hybridization between the $4f$ (partially filled shell) and $5d$. The X-rays magnetic cross section depends on the direction between the magnetic moment and the polarization of the X-rays. This dependence can be investigated through the so-called azimuthal scan. This scan is performed rotating the sample around the scattering vector, while the incident beam is polarized.

For the two proposed magnetic structure (Γ^9 and Γ^6) the magnetic cross section of equation 2.2 can be calculated and the profile of the azimuthal scan can be simulated and compared with the experimental data at 2 K. The intensity observed and calculated is reported in figure 2.8, which clearly proves that the magnetic moment lies in the a, b-plane (compatible with Γ^9 representation). Therefore Scagnoli *et al.* concluded that the magnetic ordering is the one depicted in figure 2.9 at 2 K.

2.3.2 Phase diagram

Petrovic *et al.* studied the magnetic structure of $EuTiO_3$ below the Néel temperature[5]. First of all they perfomed direct current magnetization measurements on a single crystal. The results are shown in figure 2.10. The magnetization and the magnetic susceptibility have been measured along the

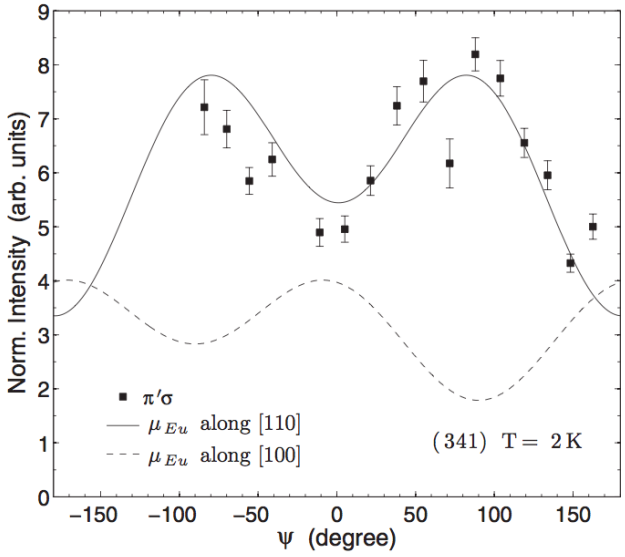

Figure 2.8: Azimuthal angle dependence of the (341) magnetic reflection. The continuos line represents a fit to the data with the magnetic moments along the [110] direction. The dotted line represents a fit with moments along the [100] direction. Measurements were performed in the vicinity of the Eu L_2 edge. The azimuthal angle equals zero when the [001] direction is in the plane perpendicular to the scattering plane. The measurement were performed at 2 K. Figure from Ref. [4].

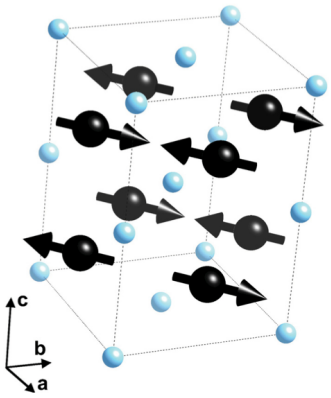

Figure 2.9: The G-type magnetic structure of $EuTiO_3$ as determined by neutron and X-ray magnetic diffraction. Big (black) spheres represent teh Eu ions, small (light blue) spheres represent the Ti atoms. Oxygen atoms are not shown for clarity. The black arrows illustrate the direction of the Eu magnetic moments. Figure from Ref. [4].

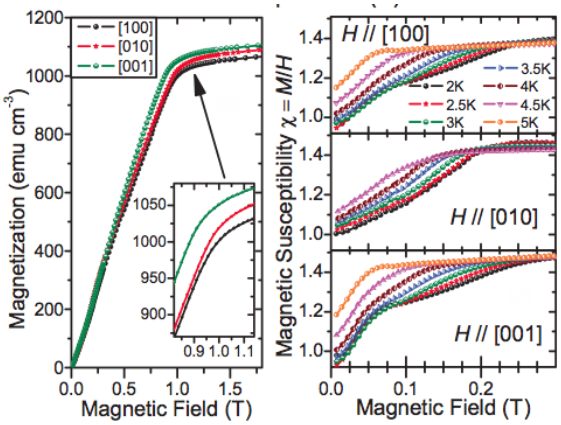

Figure 2.10: DC magnetization along the crystal axes and spin flop transition in χ for field parallel to each axis. Figure from Ref. [5].

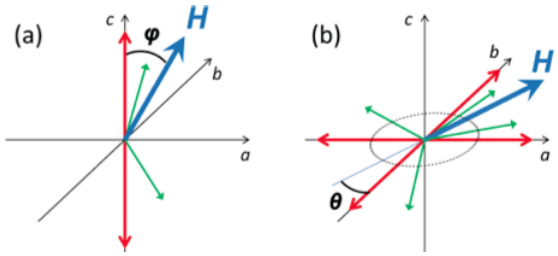

Figure 2.11: Torque experimental schematic, (a) in the case of spin along c-axis, (b) in the a, b-plane. In red are depicted the moment directions for zero applied field, in green the moment directions for the applied field $\boldsymbol{H}$ (blue arrow). Figure from Ref. [5].

three crystallographic directions: [100], [010] and [001]. In the left panel of figure 2.10 the magnetization is shown. In the three crystallographic direction measured, the magnetization saturates at similar value of the magnetic field (around 1 T), with a moment $\mu = 7.08 \pm 0.2\ \mu_B$/unit cell. The anisotropy, which is shown in the insect, is due to the anisotropy of the g tensor in this tetragonal sistem. In fact is the magnetization along the c-axis which mainly differs from the two other axis. Looking at the left panel the authors identifies a spin-flop transition. They start form considering the theoretical form of the magnetic susceptibility of an antiferromagnet. In this phase the temperature dependence of the magnetic susceptibility has a well know behaviour. In fact, if the magnetic field is applied parallel to the spin alignment the magnetic suscpetibility is expected to decrease to zero with decreasing temperature (under the Néel temperature), whereas if the magnetic field is applied perpendicular to the spin alignment the magnetic susceptibility should remain constant. However in this latter case, above a certain field threshold, a spin-flop transition can occur and the magnetization rapidly increases. In the right panel of figure 2.10 the authors identify a spin-flop transitions along all the three crystallographic axis, and this is possible only if the magnetic moments could be aligned both in the a, b-plane and c-axis direction. They conclude that a multiple configuration of the magnetic moment is possible under T_N.

After the direct current magnetization measurement, the authors performed a torque magnetometry measure. By this technique the magnetic anisotropy of the crystal may be determined by rotating a crystal within a constant magnetic field and tracking the temperature dependence of both the amplitude and periodicity of the generated torque signal. In figure 2.11 (a) is outlined the experiment in the case of a one-dimensional AF ordering,

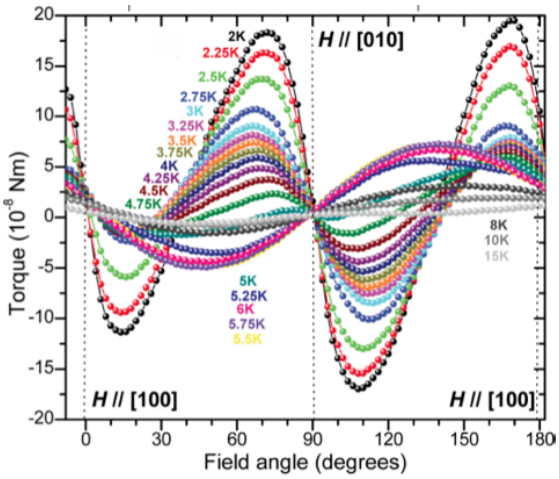

Figure 2.12: Temperature dependence of the torque // [001] for $H = 0.05$ T. Rotating the field in the (100) and (010) planes gives similar results. Figure from Ref. [5].

whereas in 2.11 (b) is outlined the experiment in the case of a two-dimensional AF ordering. If the magnetic moment lies on the c-axis, the torque will be proportional to the $\sin(2\phi)$ when the field rotates in a plane containing the c-axis. On the other hand, if the magnetic moment lies in the a, b-plane, the torque will be proportional to the $\sin(4\theta)$. Anysotropic paramagnetism above T_N will also generate a $\sin(2\phi)$ signal. In figure 2.12 the results of the torque magnetometry experiment are shown. The transition from the $\sin(2\phi)$ behaviour to $\sin(4\theta)$, when the antiferromagnetic phase occurs, is clearly visible. Fitting the curves with a function

$$\tau(\alpha) = A\sin(2\alpha) + B\sin(4\alpha) \tag{2.3}$$

Petrovic *et al.* obtained the fitting parameter A and B whose temperature dependence are shown in the left panel of figure 2.13. As expected B only appears under the Néel temperature and increases rapidly below 3 K, accordingly with a drop in A. This behaviour is explained with a change from the one-dimensional to the two-dimensional ordering structure. On the right panel is shown a spin-flop transition occuring from a a, b-plane ordering at 2 K, confirming that at this temperature the the magnetic structure is Γ^9. Finally we present the phase diagram proposed by Petrovic *et al.* in figure 2.14. The (a) panel is the experimentally determined diagram phase, which shows that for zero applied-magnetic-field between 2.75 K and the Néel temperature the one-dimensional magnetic ordering is favoured with respect to

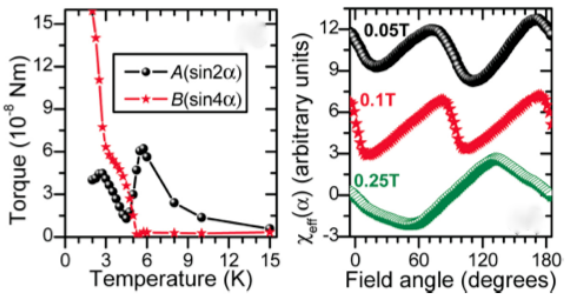

Figure 2.13: (l)Temperature dependence of the separated $\sin(2\alpha)$ and $\sin(4\alpha)$ contributions to the total torque shown in figure 2.12.(r) Field evolution of the effective susceptibility $\chi(\alpha) = \tau(\alpha)/H^2$ revealing the spin flop transition at $T = 2$ K. Figure from Ref. [5].

the two-dimensional magnetic ordering. In panel (b) and (c) are presented the calculated phase diagram from a two-sublattices mean field theory with magnetic field applied along the [100] and [001] directions.

2.4 Sample synthesis

Polycristalline $EuTiO_3$ powder was prepared by solid-state reaction. A stechiometric mixture of Eu_2O_3 (99.9% purity; Metall Rare Earth Limited) and TiO_2 (99%-100%; Sigma-Aldrich) was ball-milled and reacted for 10 h at 1000° C under a flowing mixture of 5% H_2 in Ar (100 ml/min). The resulting phase purity waws checked by laboratory x-ray powder diffraction. Part of the powder was reground and pressed into bars (13 x 2 x 2 mm) using 10^4 Pa uniaxial pressure. Finally the bars were sintered for a further 10 h at 1000° C under a reducing atmosphere (100 ml/min of 5% H_2 in Ar). A small fragment was used to measure the specific heat and the result were found to be consistent with the literature.

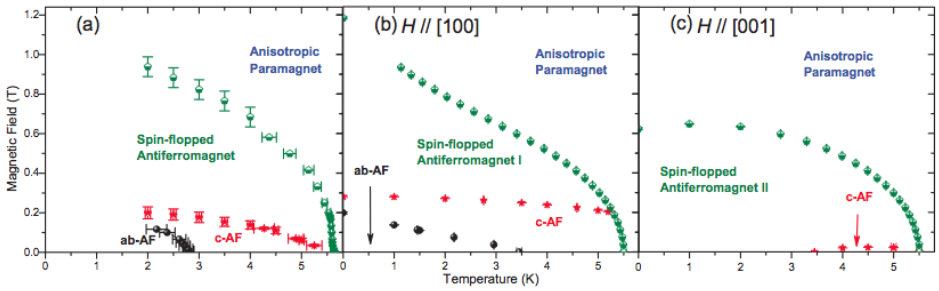

Figure 2.14: (a) Experimentally determined magnetic phase diagram of $EuTiO_3$. (b) and (c) Two-sublattice mean-field phase diagrams for $\boldsymbol{H}$ // [100] and [001]. *ab*-AF refers to zero-field AF order laong the [110] or [1$\bar{1}$0] axis, while *c*-AF describes AF order along [001]. For the spin-flopped AF I phase, the spins order in the a, b-plane with the staggered component of the magnetization perpendicular to the applied field. In contrast, spin-flopped AF II corresponds to AF ordering along [110] or [1$\bar{1}$0], with a uniform magnetization component along the *c*-axis. The emergence of orthogonal domains at low temperature in $EuTiO_3$ implies that our experimentally determined diagram (a) should be superposition of (b) and (c). Figure from Ref. [5]

Chapter 3

Techniques

In order to study the crystallographic and magnetic structure of $EuTiO_3$ we performed a neutron powder diffraction experiment. Neutron scattering and diffraction are among the most powerful and versatile experimental methods to study the structure of materials on the nanometer scale. Neutron can be produced in a number of ways, e.g. as by-products of cosmic radiation or radioactive decay of heavy nuclei. More recently, neutrons have been produced in a laboratory experiment, using a piezoelectric crystal to accelate ions of deuterium to high energies. Neutron sources with flux adequate for neutron scattering investigations of materials are based on one of two principles, also illustrated in figure 3.1:

- *Fission.* A high continuous flux of neutrons is produced in the core of a conventional fission reactor. For neutron scattering purposes, research reactors with compact cores are used rather than the more abundant nuclear power plants.

- *Spallation.* By bombarding target of heavy elements with high-energy particles (typically protons), a very large number of neutrons can be produces. Spallation sources are typically pulsed, but can also be pseudo-continuous, depending on the proton accelerator.

Once produced the neutrons are being moderated to thermal velocities close to the source and then transported to the neutron scattering instruments in neutron guide systems. Different moderators and guiding systems can be implemented in order to select the velocity and the energy resolution required (e.g. short wavelength for high resolution structural experiment and long wavelength for magnetic structure investigation). Both types of neutron sources are built as dedicated facilities, each hosting tens of instruments. Among the reactor sources Insitute Laue-Langevin in Grenoble (France) is the leading one, with its 58 MW of power and more than 50 instruments.

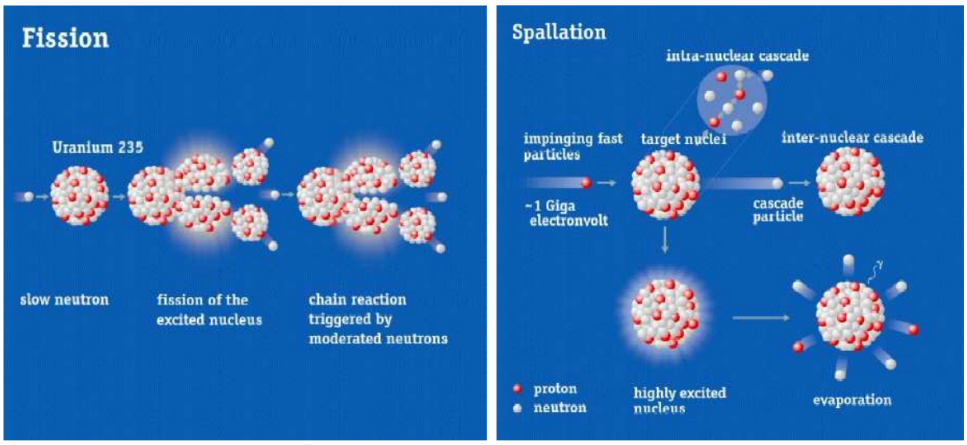

Figure 3.1: The two different ways of neutron production. Left: traditional nuclear reactors make use of production of neutrons for maintaining the chain reaction; extra neutrons can be used for neutron scattering. Right: protons accelerated into the GeV regime can split heavy nuclei with a large neutron surplus, creating free neutrons as a part of the reaction products. Figure from Ref. [6].

The power of neutron scattering techniques can be understood by studying the physical processes involved in the interaction between a neutron and a scattering system. The theory of the neutron scattering, briefly summarised in the following section, can be found in Ref. [42].

3.1 Neutron scattering

Consider a beam of thermal neutrons travelling along the z-axis, all with the same energy E, incident on a *scattering system*. Suppose we set up a neutron counter, of area $\mathrm{d}\Omega$, and measure the number of neutron scattered in a given direction as a function of their energy E'. Let the direction of the scattered neutrons be θ, ϕ, where θ is the polar angle and ϕ is the azimuthal angle. The *partial differential cross-section* is defined by the equation

$$\frac{\mathrm{d}^2\sigma}{\mathrm{d}\Omega\,\mathrm{d}E'} = \begin{array}{l}\text{number of neutrons scattered per second into a} \\ \text{small solid angle } \mathrm{d}\Omega \text{ in the direction } \theta,\phi \text{ with final} \\ \text{energy between } E' \text{ and } E' + \mathrm{d}E'/\Phi\,\mathrm{d}\Omega\,\mathrm{d}E'\end{array} \quad (3.1)$$

where Φ is the flux of the incident neutrons. Suppose we do not analyse the energy of the scattered neutrons, but simply count all the scattered neutron

into the solid angle $\mathrm{d}\Omega$, despite of their energy. In this case the corresponding cross-section is called *differential cross-section* and is defined by

$$\frac{\mathrm{d}\sigma}{\mathrm{d}\Omega} = \int_0^\infty \left(\frac{\mathrm{d}^2\sigma}{\mathrm{d}\Omega\, \mathrm{d}E'} \right) \mathrm{d}E' \tag{3.2}$$

The *total scattering cross-section* is obtained integrating over all direction. This calculation is particularly simple in the case that the partial cross-section does not depend on ϕ

$$\sigma_{tot} = \int_0^\pi \frac{\mathrm{d}\sigma}{\mathrm{d}\Omega} 2\pi \sin\theta \, \mathrm{d}\Omega \tag{3.3}$$

The cross-sections could be actually measured in scattering experiments. Therefore in order to analyse the results of such experiments we have to be able to relate these quantities to the internal structure of the scattering system and the nature of the interaction between the neutron and the system.

Consider a neutron-nucleus system. Let be E the energy of the incoming neutron and $\boldsymbol{k}$ its wave vector. Let be the z-axis along the $\boldsymbol{k}$ direction and the nucleus fixed in the origin. The wavevector of the incoming particle is then

$$\psi_{inc} = \exp(\mathrm{i}kz) \tag{3.4}$$

and if we can consider the range of the forces responsible for the interaction short compared to the wavelength of the neutron, the wavevector of the scattered particle can be written as

$$\psi_{sc} = -\frac{b}{r} \exp(\mathrm{i}kr) \tag{3.5}$$

where b is a constant (which depends from the nucleus spin) and it is called *scattering length*. The wavevector of the incoming and of the out-coming neutron are of the same magnitude. In fact if the nucleus is fixed, it cannot change its kinetic energy. Besides that the energy of a thermal neutron is too low to modify the internal state of the nucleus, therefore the interaction, in this case, must be elastic.

3.1.1 Nuclear scattering

We now start to evaluate the differential cross-section defined in equation 3.1 for the case of the nuclear scattering. Consider a transition in which the scattering system state changes from λ to λ' and the neutron state (which is a plane wave) changes from $\boldsymbol{k}$ to $\boldsymbol{k'}$. The state of the scattering particle

is now fully defined by its wavevector because in this section we will neglect any magnetic interaction. Using the relation known as the *Fermi's golden rule* we can write

$$\left(\frac{\mathrm{d}^2\sigma}{\mathrm{d}\Omega\,\mathrm{d}E'}\right)_{\lambda\to\lambda'} = \frac{k'}{k}\left(\frac{m}{2\pi\hbar^2}\right) |\,\langle \boldsymbol{k'}\lambda'|V|\boldsymbol{k}\lambda\rangle\,|^2\delta(E_\lambda - E'_\lambda + E - E') \quad (3.6)$$

where m is the mass of the neutron and V is the potential describing the neutron-nucleus interaction. The δ-function ensures the energy conservation. We begin evaluating the matrix element $|\,\langle \boldsymbol{k'}\lambda'|V|\boldsymbol{k}\lambda\rangle\,|^2$ in equation 3.6, this means that a form to the potential V must be given. The nuclear interaction is *short-range*, therefore we can model it with a sum of δ-functions each centered in the nuclei positions. Let be $\boldsymbol{r}$ the neutron position and $\boldsymbol{R}_l$ the position of the l-th nucleus. V can be written in the form

$$V = \sum_l V_l\left(\boldsymbol{r} - \boldsymbol{R}_l\right) = \frac{2\pi\hbar^2}{m}\sum_l b_l\delta\left(\boldsymbol{r} - \boldsymbol{R}_l\right) \quad (3.7)$$

Using 3.7 and performing the integration over the neutron position in equation 3.6, we obtain

$$\left(\frac{\mathrm{d}^2\sigma}{\mathrm{d}\Omega\,\mathrm{d}E'}\right)_{\lambda\to\lambda'} = \frac{k'}{k}\left|\sum_l b_l\,\langle\lambda'|\exp(\mathrm{i}\boldsymbol{\kappa}\cdot\boldsymbol{R}_l)|\lambda\rangle\right|^2\delta(E_\lambda - E'_\lambda + E - E') \quad (3.8)$$

where we introduced the *scattering vector* $\boldsymbol{\kappa} = \boldsymbol{k} - \boldsymbol{k'}$. In $\boldsymbol{k'}$-direction we count all the neutrons regardless to the nucleus transition involved: the conservation of energy is the only constrain. Therefore we have to evaluate the right-side of 3.8 summing over all final states λ', keeping the initial state λ fixed, and then averaging over all λ.

$$\begin{aligned}\left(\frac{\mathrm{d}^2\sigma}{\mathrm{d}\Omega\,\mathrm{d}E'}\right) &= \frac{k'}{k}\frac{1}{2\pi\hbar}\sum_{ll'} b_l b_{l'}\int_{-\infty}^{\infty}\langle\exp\{-\mathrm{i}\boldsymbol{\kappa}\cdot\mathbf{R}_{l'}(0)\}\exp\{\mathrm{i}\boldsymbol{\kappa}\cdot\boldsymbol{R}_l(t)\}\rangle \\ &\quad\times\exp\left(-\mathrm{i}\omega t\right)\mathrm{d}t \end{aligned} \quad (3.9)$$

where ω is defined by

$$\hbar\omega = E - E' \quad (3.10)$$

and we introduced the Heisenberg operator $\boldsymbol{R}_l$, given by

$$\boldsymbol{R}_l(t) = \exp\left(\mathrm{i}Ht/\hbar\right)\boldsymbol{R}_l\exp\left(-\mathrm{i}Ht/\hbar\right) \quad (3.11)$$

Equation 3.9 is the basic expression for the partial differential cross-section for nuclear scattering. It is a compact expression and it can be

directly measured. However it is far from being simple. In fact the knowledge of the eigenstates $|\lambda\rangle$ of the scattering system is still required for using this formula, they are simply hidden in the Heisenberg operator which contains the Hamiltonian describing the system.

Consider a scattering system of a single element in which the scattering length b_l varies from one nucleus to another owing to nuclear spin or the presence of isotopes or both. The partial cross-section sperimentally measured is an average over all these values of b present in the system. If we assume that no correlation exists between the values of the scattering length for any two nuclei, the partial cross-section can be split in two terms, the first known as *coherent* and the second as *incoherent* scattering cross section, defined as

$$\left(\frac{\mathrm{d}^2\sigma}{\mathrm{d}\Omega\,\mathrm{d}E'}\right)_{coh} = \frac{\sigma_{coh}}{4\pi}\frac{k'}{k}\frac{1}{2\pi\hbar}\sum_{ll'}\int_{-\infty}^{\infty}\langle\exp\{-\mathrm{i}\boldsymbol{\kappa}\cdot\boldsymbol{R}_{l'}(0)\}\exp\{\mathrm{i}\boldsymbol{\kappa}\cdot\boldsymbol{R}_l(t)\}\rangle \times\exp\left(-\mathrm{i}\omega t\right)\mathrm{d}t \tag{3.12}$$

$$\left(\frac{\mathrm{d}^2\sigma}{\mathrm{d}\Omega\,\mathrm{d}E'}\right)_{inc} = \frac{\sigma_{inc}}{4\pi}\frac{k'}{k}\frac{1}{2\pi\hbar}\sum_{l}\int_{-\infty}^{\infty}\langle\exp\{-\mathrm{i}\boldsymbol{\kappa}\cdot\boldsymbol{R}_l(0)\}\exp\{\mathrm{i}\boldsymbol{\kappa}\cdot\boldsymbol{R}_l(t)\}\rangle \times\exp\left(-\mathrm{i}\omega t\right)\mathrm{d}t \tag{3.13}$$

where

$$\sigma_{coh} = 4\pi(\bar{b})^2, \qquad \sigma_{inc} = 4\pi\{\overline{b^2} - (\bar{b})^2\} \tag{3.14}$$

We see from equation 3.12 that the coherent scattering depends on the correlation between the positions of the *same* nucleus at different times, and on the correlation between the position of *different* nuclei at different times. It therefore gives *interference* effects. The incoherent scattering, defined in equation 3.13 depends only on the correlation between the position of the *same* nuclei at different times. It does not give interference effects. In the following sections we will focus only on the coherent part of the scattering cross-section, because is the one of interest in a diffraction experiment.

3.1.2 Nuclear diffraction

Up to now we did not put any constrains to the position of the nuclei in the scattering system. However, if neutron scattering is used to study a crystal, the generic position of nucleus can be written as

$$\boldsymbol{R}_l = \boldsymbol{l} + \boldsymbol{u}_l \tag{3.15}$$

where $\boldsymbol{l}$ is a lattice vector and $\boldsymbol{u}_l$ the displacement of the l-th nucleus from its equilibium position ($\boldsymbol{l}$), due to thermal motion. Consequently the Heisenberg operator of equation 3.11 becomes

$$\boldsymbol{R}_l(t) = \boldsymbol{l} + \boldsymbol{u}_l(t) \tag{3.16}$$

where $\boldsymbol{u}_l(t)$ is an operator and $\boldsymbol{l}$ is a constant. We assume that the potential describing the inter-atomic forces in the crystal is harmonic. For such potential the displacements $\boldsymbol{u}_l$ can be expressed as a linear combination of the normal modes of vibration of the crystal. The periodicity of a Bravais lattice let us simplify the summation over l and l' in equation 3.12, in fact, for each value of l' the summations over l are identical and therefore

$$\begin{aligned} &\sum_{ll'} \langle \exp\{-\mathrm{i}\boldsymbol{\kappa}\cdot\boldsymbol{R}_{l'}(0)\} \exp\{\mathrm{i}\boldsymbol{\kappa}\cdot\boldsymbol{R}_l(t)\}\rangle \\ &\quad = N\sum_l \exp(\mathrm{i}\boldsymbol{\kappa}\cdot\boldsymbol{l}) \langle \exp\{-\mathrm{i}\boldsymbol{\kappa}\cdot\boldsymbol{u}_0(0)\} \exp\{\mathrm{i}\boldsymbol{\kappa}\cdot\boldsymbol{u}_l(t)\}\rangle \end{aligned} \tag{3.17}$$

where N is number of scattering centres in the system. The form and the properties of the normal modes are well known and combined with equation 3.17, allow us to express the differential cross-section as

$$\begin{aligned} \left(\frac{\mathrm{d}^2\sigma}{\mathrm{d}\Omega\,\mathrm{d}E'}\right)_{coh} &= \frac{\sigma_{coh}}{4\pi}\frac{k'}{k}\frac{N}{2\pi\hbar}\exp\langle U^2\rangle \sum_l \exp(\mathrm{i}\boldsymbol{\kappa}\cdot\boldsymbol{l}) \\ &\quad \times \int_{-\infty}^{\infty} \exp\langle UV\rangle \exp(-\mathrm{i}\omega t)\,\mathrm{d}t \end{aligned} \tag{3.18}$$

where

$$U = -\mathrm{i}\boldsymbol{\kappa}\cdot\boldsymbol{u}_0(0) \tag{3.19}$$

$$V = \mathrm{i}\boldsymbol{\kappa}\cdot\boldsymbol{u}_l(t) \tag{3.20}$$

Let's focus our attention on the integrand of right term of equation 3.18. If we expand the exponential term we obtain

$$\exp\langle UV\rangle = 1 + \langle UV\rangle + \frac{1}{2!}\langle UV\rangle^2 + \ldots + \frac{1}{p!}\langle UV\rangle^p + \ldots \tag{3.21}$$

The first term of right-hand side represents the elastic process, in other words a process in which the state of the scattering system remains unchanged. The second term represents the one-phonon process, and the p-th term gives the cross-section for all p-phonons processes.

If we consider only the elastic scattering, the sum over l can be written, due to the Bravais lattices' properties, in the form

$$\sum_l \exp\left(\mathrm{i}\boldsymbol{\kappa}\cdot\boldsymbol{l}\right) = \frac{(2\pi)^3}{v_0}\sum_\tau \delta(\boldsymbol{\kappa}-\boldsymbol{\tau}) \tag{3.22}$$

where $\boldsymbol{\tau}$ is a reciprocal lattice vector and v_0 is the volume of the crystallographic cell.

Finally, integrating 3.18, considering 3.22 and the only the first term in right-hand side of 3.21, with respect to energy E', we get

$$\left(\frac{\mathrm{d}\sigma}{\mathrm{d}\Omega}\right)_{coh\ el} = \frac{\sigma_{coh}}{4\pi}N\frac{(2\pi)^3}{v_0}\exp\left(-2W\right)\sum_\tau \delta(\boldsymbol{\kappa}-\boldsymbol{\tau}) \tag{3.23}$$

which is the cross-section fo elastic coherent neutron scattering, where

$$2W = -\left\langle U^2\right\rangle \tag{3.24}$$

is known as *Debye-Waller factor*. The δ-functions in 3.23 tell us that a reflection occurs only if

$$\boldsymbol{\kappa} = \boldsymbol{k}-\boldsymbol{k'} = \boldsymbol{\tau} \tag{3.25}$$

The Debye-Waller factor is related both to the scattering vector and to the motion of the nuclei from their equilibrium positions. For a cubic crystal can be proved that

$$2W = \tfrac{1}{3}\kappa^2\left\langle u^2\right\rangle \tag{3.26}$$

where u is the modulus of the displacement of a nucleus from the lattice point, and the average is performed over all nuclei. For non-cubic crystal equation 3.26 does not apply but still it is a good approximation. The vibrations of nuclei usually extent for very short distances and, especially at low temperature, the Debye-Waller factor is approximately constant, unless the lattice is undergoing a transition, e.g. a melting transition. We can generalise the results above to the case of crystal with a basis (more than one atom per unit cell). The position of the scattering center can be written as

$$\boldsymbol{R}_{ld} = \boldsymbol{l}+\boldsymbol{d}+\boldsymbol{u}\binom{l}{d} \tag{3.27}$$

where $\boldsymbol{l}+\boldsymbol{d}$ is the equilibrium position of d-th atom in the cell centred in $\boldsymbol{l}$ and $\boldsymbol{u}\binom{l}{d}$ is the displacement from equilibrium. In this case the the scattering cross-section for elastic processes is given by

$$\left(\frac{\mathrm{d}\sigma}{\mathrm{d}\Omega}\right)_{coh\ el} = N\frac{(2\pi)^3}{v_0}\sum_{\boldsymbol{\tau}} \delta(\boldsymbol{\kappa}-\boldsymbol{\tau})|F_N(\boldsymbol{\kappa})|^2 \tag{3.28}$$

where

$$F_N(\boldsymbol{\kappa}) = \sum_d \bar{b}_d \exp\left(\mathrm{i}\boldsymbol{\kappa}\cdot\boldsymbol{d}\right)\exp\left(-W_d\right) \tag{3.29}$$

$F_N(\boldsymbol{\kappa})$ is known as the *nuclear unit-cell structure factor*, and W_d is the Debye-Waller factor of the d-th atom, and is still related to the scattering vector and the mean squared displacement of the atom from its equilibrium position.

Different methods had been developed for measuring the cross section of equation 3.28: the Laue method, the rotating crystal method and the powder or *Debye-Scherrer* method[43]. All these techniques, firstly developed for X-rays, immediately applied to the neutron case. In the powder method, which is the one we actually used, the incoming neutron beam needs to be monochromatic and the scattering sample is a powder made of crystallites on the order of a micron. Because small crystal are present in all orientations in the sample, the net effect is a series of ring of scattering peaks, corresponding to every reciprocal lattice vector of magnitude less than twice that of the incoming beam. The the cross-section for each ring is

$$\sigma_{tot\boldsymbol{\tau}} = \frac{V}{v_0^2}\frac{\lambda^3}{4\sin\theta}\sum_{\boldsymbol{\tau}}\left|F_N(\boldsymbol{\tau})\right|^2 \tag{3.30}$$

where the sum over $\boldsymbol{\tau}$ is the sum over all reciprocal lattice vectors with the same value of $|\boldsymbol{\tau}|$, and V is the sample volume.

3.1.3 Magnetic scattering

We now consider the cross-section due to magnetic interaction between the neutron and the crystal. Whereas the nuclear scattering occurs because of the short-range nuclear forces and so is always present, the magnetic scattering occurs because of unpaired electrons in the atoms of the crystal. As done in the nuclear scattering description, we can apply the Fermi's golden rule to the case of magnetic scattering, leading to

$$\left(\frac{\mathrm{d}^2\sigma}{\mathrm{d}\Omega\,\mathrm{d}E'}\right)_{\lambda\to\lambda'} = \frac{k'}{k}\left(\frac{m}{2\pi\hbar^2}\right)\left|\,\langle\boldsymbol{k'}\sigma'\lambda'|V_m|\boldsymbol{k}\sigma\lambda\rangle\,\right|^2\delta(E_\lambda - E'_\lambda + \hbar\omega) \tag{3.31}$$

where the interaction potential can be written as

$$V_m = -\boldsymbol{\mu}_n\cdot\boldsymbol{B} \tag{3.32}$$

and $\boldsymbol{\mu}_n$ is the magnetic dipole moment of the neutron given by

$$\boldsymbol{\mu}_n = -\gamma\mu_n\boldsymbol{\sigma} \tag{3.33}$$

where

$$\mu_n = \frac{e\hbar}{2m_p} \tag{3.34}$$

and $\boldsymbol{\sigma}$ is the Pauli spin operator for the neutron. The magnetic field in equation 3.32 is generated from the electrons and can be expressed as the sum of two terms. The first describing the magnetic field generated from the spin of the electrons and the second from its orbital motion. Their sum is given by

$$\boldsymbol{B} = \boldsymbol{B}_S + \boldsymbol{B}_L = \frac{\mu_0}{4\pi}\left\{\nabla \times \left(\frac{\boldsymbol{\mu}_e \times \hat{\boldsymbol{R}}}{R^2}\right) - \frac{2\mu_B}{\hbar}\frac{\boldsymbol{p} \times \hat{\boldsymbol{R}}}{R^2}\right\} \tag{3.35}$$

where

$$\boldsymbol{\mu}_e = -2\mu_B \boldsymbol{s} \tag{3.36}$$

is the magnetic moment of an electron, associated to its spin angular momentum and $\mu_B = \frac{e\hbar}{2m_e}$ is the Bohr magneton. The right-hand term of 3.31 can now be developed and we have for the magnetic cross-section

$$\begin{aligned}\frac{\mathrm{d}^2\sigma}{\mathrm{d}\Omega\,\mathrm{d}E'} &= \frac{(\gamma r_0)^2}{2\pi\hbar}\frac{k'}{k}\sum_{\alpha\beta}(\delta_{\alpha\beta} - \hat{\kappa}_\alpha\hat{\kappa}_\beta)\sum_{l'd'ld}\tfrac{1}{4}g_{d'}g_d F^*_{d'}(\boldsymbol{\kappa})F_d(\boldsymbol{\kappa}) \\ &\quad\times\int_{-\infty}^{\infty}\langle\exp\{-\mathrm{i}\boldsymbol{\kappa}\cdot\boldsymbol{R}_{l'd'}(0)\}\exp\{\mathrm{i}\boldsymbol{\kappa}\cdot\boldsymbol{R}_{ld}(t)\}\rangle \\ &\quad\times\langle J^\alpha_{l'd'}(0)J^\beta_{ld}(t)\rangle\exp(-\mathrm{i}\omega t)\,\mathrm{d}t\end{aligned} \tag{3.37}$$

where

$$r_0 = \frac{\mu_0}{4\pi}\frac{e^2}{m_e} \tag{3.38}$$

α and β stand for x, y and z, $\delta_{\alpha\beta}$ is the Kronecker delta, $\hat{\kappa_\alpha}$ is the α-component of a unit vector in the direction of $\boldsymbol{\kappa}$, g_d is the Landé factor of the d-th atom, $F_d(\boldsymbol{\kappa})$ is the *magnetic form factor*, and J^β_{ld} is the operator corresponding to the α-component of total angular momentum for the ion l, d. The expression we have presented is valid under a few restrictions. First we assumed that the scattering system is a crystal, and the unpaired electrons are localised close to the equilibrium positions of the ions, this is the reason why in the equation appeared the Heisenberg operators $\boldsymbol{R}_{ld}(t)$. This is known as *Heitler-London* model. Secondly we assume LS coupling and the angular momentum of the ion is therefore specified by the total angular momentum operator $\boldsymbol{J} = \boldsymbol{L} + \boldsymbol{S}$.

The magnetic form factor is related to the distribution of the unpaired electrons, for the simple case in which the scattering is due only to spin

($L = 0$, or angular momentum quenched as in 3^d metals) it is given by

$$F_d(\boldsymbol{\kappa}) = \int \rho_d(\boldsymbol{r}) \exp\left(\mathrm{i}\boldsymbol{\kappa} \cdot \boldsymbol{r}\right) \mathrm{d}\boldsymbol{r} \tag{3.39}$$

where the scalar function $\rho_d(\boldsymbol{r})$ is the normalised density of the unpaired electrons in the ion d. Equation 3.39 is the Fourier transform of the normalised density of unpaired electrons. A more general result have been given by Johnston[44], and is presented in section 3.3.

3.1.4 Magnetic diffraction

As done in the nuclear case we can apply equation 3.37 to a magnetically ordered crystal such as an antiferromagnet and only consider the elastic scattering processes. Let's describe such material as the sum of two ferromagnetic sublattices. Denote the mean spin direction in the two sublattices by $\pm\hat{\boldsymbol{\eta}}$. Let be $\langle J^\eta \rangle$ the mean total angular momentum along η-direction of one of the sublattices (the mean total angular momentum of the other sublattice will be opposite, giving a vanishing average over all ions in the crystal). The expression for the cross-section is thus

$$\begin{aligned}\left(\frac{\mathrm{d}\sigma}{\mathrm{d}\Omega}\right)_{el} &= (\gamma r_0)^2 N_m \frac{(2\pi)^3}{v_{0m}} \sum_{\boldsymbol{\tau_m}} |F_M(\boldsymbol{\tau}_m)|^2 \exp\left(-2W\right) \\ &\quad \times\{1 - (\hat{\boldsymbol{\tau}}_m \cdot \hat{\boldsymbol{\eta}})^2_{av}\}\delta(\boldsymbol{\kappa} - \boldsymbol{\tau}_m)\end{aligned} \tag{3.40}$$

where

$$F_M(\boldsymbol{\tau}_m) = \tfrac{1}{2} g \langle J^\eta \rangle F(\boldsymbol{\tau}_m) \sum_d \sigma_d \exp\left(\mathrm{i}\boldsymbol{\tau}_m \cdot \boldsymbol{d}\right) \tag{3.41}$$

In these equation N_m is the number of magnetic cells, which is half the number of crystallographic cells, v_{0m} is the volume of magnetic cells, which is double the number of crystallographic cells, $\boldsymbol{\tau}_m$ is a reciprocal magnetic lattice vector and $\hat{\boldsymbol{\tau}}_m$ a unit vector along $\boldsymbol{\tau}_m$-direction. $\sum_d$ means sum over the ions in the magnetic unit cell and σ_d has the value ± 1 for ions with mean total angular momentum direction $\pm\hat{\boldsymbol{\eta}}$ respectively. Comparing equations 3.28 and 3.40, we can appreciate the differences between nuclear and magnetic scattering. Firstly, in nuclear scattering, reflections can occur only when the scattering vector belongs to the nuclear reciprocal lattice, whereas in magnetic scattering reflections can occur when the scattering vector belongs to the magnetic reciprocal lattice. Secondly the magnetic scattering is strongly temperature dependent, in fact $\langle J^\eta \rangle$ falls rapidly to zero when approaching Néel temperature (T_N), whereas the only temperature

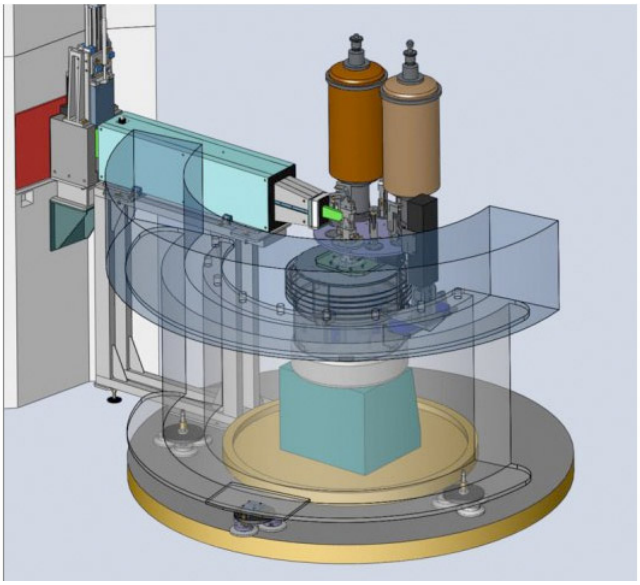

Figure 3.2: D2B seen from behind the detector. Figure from Ref. [7].

dependence of nuclear scattering is given by the Debye-Waller factor (which is approximately constant in suitable conditions). Thirdly the magnetic form factor quickly decreases when increasing $|\boldsymbol{\tau}_m|$. In fact the magnetic form factor is, in the case presented in equation 3.39, the Fourier transform of the electron density and therefore as the spatial displacement of the electron is comparable with the neutron wavelength the magnetic form factor decreases with $\boldsymbol{\kappa}$. On the other hand, the nuclei displacement is very little, compared with the neutron wavelength, and its Fourier transform is approximately constant in $\boldsymbol{\kappa}$.

3.2 D2B beamline at ILL

Through the cross-sections and the form factors we can relate the scattered intensity to the structural information we are looking for. Here we describe the instrument used for measuring the scattering intensity. We performed our neutron powder diffraction experiment at D2B (figure 3.2) beamline at ILL[45, 46, 7]. D2B is a very high-resolution powder diffractometer designed to achieve the ultimate resolution, limited only by powder particle size ($\frac{\Delta d}{d} \sim 5 \cdot 10^{-4}$). The layout of the instrument is *Debye-Scherrer* in the sense that it uses a cylindrical sample with transmission geometry. This instrument has four main applications:

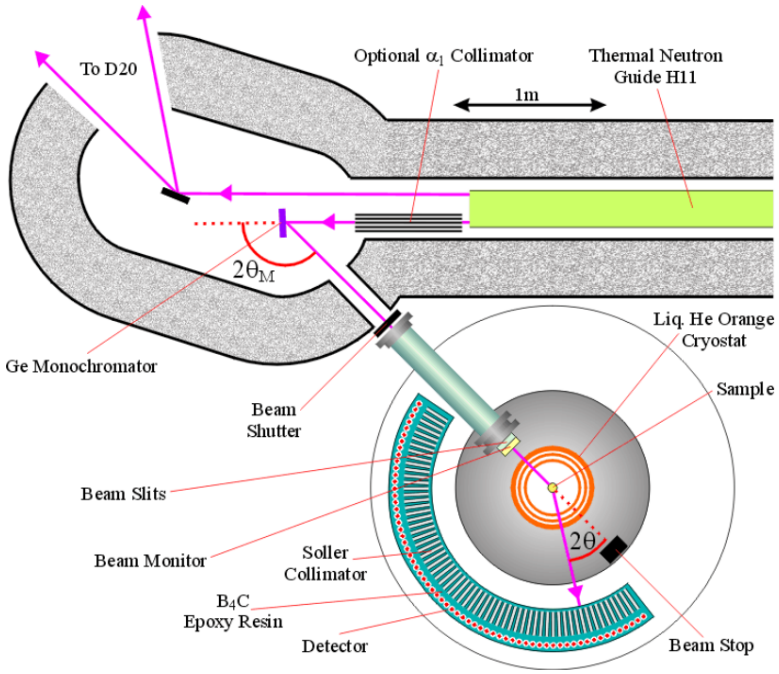

Figure 3.3: Schematic representation of D2B beamline. Figure from Ref. [8].

- the structural chemistry of non-rigid molecules;
- ab-initio structure solution from powders;
- crystal and magnetic structure determination of powder compounds (even small sample);
- dependance in temperature/pressure/magnetic-field structural (or magnetic) studies for powder.

Low temperature measurements are possible due to the liquid He cryostat, which can be used to achieve sample temperatures as low as 1.5 K.

The term high-resolution refers not to the smallest peak width in the powder diffraction pattern, but to the fact that the instrumental resolution function results in narrow peaks at high scattering angle (2θ). This is achieved by having large monochromator take-of angles as shown in figure 3.3, which for this instrument is 135° (Ge monochromator). Six different neutron wavelength can be selected by a simple rotation of the monochromator within the $[hhl]$ plane. The large value of the monochromator angle is required so that the wavelength dispersion, $\Delta\lambda$, of the incident beam is kept small. In order to achieve high resolution, the instrument must be able to count neutrons with a

very precise Bragg angle. For this reason Soller collimators are placed in front of each detector. Finally, given the relatively low flux available at neutron sources, instrument efficiency is greatly imporoved by using many detectors at the same time: the large multi-detector collects the neutrons scattered at all angles. It is made by 128 high resistive linear wire detectors, which are 30 cm height. The 128 linear detectors collect bidimensional images of the scatterd neutron. An example of these images is shown in figure 4.4, where the diffraction rings are clearly visible. The bidimensional image allows correction for curvature of the diffraction cone. A complete diffraction pattern is obtained after about 25 steps of 0.05° in 2θ, since the detectors are spaced at 1.25° intervals. Such scans take typically 30 minutes and they are repeated to improve statistics. The bidimensional images are integrated over the rings and avereged. The result is the profile intensity as function of 2θ (see for example figure 4.5).

3.3 Rietveld Refinement

Rietveld refinement is a method of determination of the structure of a compound. It does not use the integrated intensities, but it directly applies to profile intensity of a powder diffraction experiment[47]. In the case of neutron powder diffraction experiments, nuclear as well magnetic structures can be refined. To apply this method, first of all we must assume a model describing the sample: the crystallographic and magnetic phases present and their symmetries. Then, through a minimization process, the model is fitted onto the observed data and the optimal value of the refinable parameter (e.g: lattice constant and atoms' position) are returned. In the following sections we will present the software used to perform the Rietveld refinement and a more general formulation of the form factors which is necessary to deal with the $EuTiO_3$ case.

3.3.1 FULLPROF suite for Rietveld refinement

Several programs have been developed in the past decades to perform Rietveld refinements, among these we chose FULLPROF[48].[1]

Due to the finite size of the detectors the diffraction profile is discretize in n steps, as a function of the scattering variable 2θ. The observed profile can be modeled using the calculated counts $y_{c,\,i}$ at the i-th step by summing the

[1] In the this section the notation will be slightly changed to be consistent with FULLPROF manual[49].

contribution from the neighboring Bragg reflections plus the background

$$y_{c,\,i} = \sum_{\phi} S_{\phi} \sum_{\boldsymbol{h}} I_{\phi,\,\boldsymbol{h}} \Omega(2\theta_i - 2\theta_{\phi,\,\boldsymbol{h}}) + b_i \tag{3.42}$$

The vector $\boldsymbol{h} = \boldsymbol{H} + \boldsymbol{k}$ labels the Bragg reflections, where $\boldsymbol{H}$ identifies the crystallagraphic reflections and $\boldsymbol{k}$ is the propagation vector, which indicates the magnetic reflections[2]. The subscript ϕ labels the phase and vary from 1 up to the number of existing phase in the model. S_ϕ represents the scale factor of phase ϕ, $I_{\phi,\,\boldsymbol{h}}$ is the integrated intensity of $\boldsymbol{h}$ reflections owed to phase ϕ, Ω is the reflection profile function that models both instrumental and sample effect, centred in the angular position of the Bragg reflection $2\theta_{\phi,\,\boldsymbol{h}}$ for phase ϕ. The general expression of the integrated intensity is

$$I_{\phi,\,\boldsymbol{h}} = \{LAPCF^2\} \tag{3.43}$$

where L contains the Lorentz, polarisation and multiplicity factors, A is the absorption correction, P is the preferred orientation function, C includes special corrections and F is the structure factor[3].

The absortion correction A takes into account the neutron absorption, but only in the case of a simple cylindrical sample holder. The preferred orientation function P corrects the calculated profile when the distribution of the crystallites is not isotropic. For example plate-like crystallites have a tendency, at least in part of the sample, to align their normals along the axis of sample holder. C allows the user to manually control the calculated pattern if special correction are needed. This possibility is crucial in our case. In fact, due to the strong neutron absorption of europium atoms we did not use the simple cylindrical sample holder, but the double walled sample holder. The absorption correction for such a geometry cannot be controlled through the A factor and therefore we used the C factor.[4]

The Rietveld method consists of refining crystallographic and magnetic structures minimising the weighted squared difference between the observed intensities and the calculated pattern, against the parameter vector $\boldsymbol{\alpha} = (\alpha_1,\, \alpha_2,\, \ldots,\, \alpha_p)$, where p is the number of refined parameters. The function minimized in the method is

$$\chi^2 = \sum_{i=1}^{n} w_i \{y_i - y_{c,\,i}(\boldsymbol{\alpha})\}^2 \tag{3.44}$$

[2]The propagation vector is discussed in the following section.

[3]The general formulation of the structure factor is presented in section 3.3.2.

[4]The determination of the C factor is discussed in section 3.4.

with $w_i = \frac{1}{\sigma_i^2}$, being σ_i^2 the variance of the observation y_i, calculated supposing a Poissonian distribution.

The quality of the agreement between observed and calculated profiles is measured by a set of conventional factors

- Profile factor
$$R_p = 100 \frac{\sum_i^n |y_i - y_{c,\,i}|}{\sum_{i=1}^n y_i} \tag{3.45}$$
This factor simply measures the agreement between the observed profile and the calculated profile.

- Weighted profile factor
$$R_{wp} = 100 \left[\frac{\sum_i^n w_i |y_i - y_{c,\,i}|^2}{\sum_{i=1}^n w_i y_i^2} \right]^{1/2} \tag{3.46}$$
The weighted profile factor corrects the profile factor taking into account the Poissonian distribution, the contribution of the peaks is therofore moderated with respect to R_P.

- Expected weighted profile factor
$$R_{exp} = 100 \left[\frac{n-p}{\sum_i^n w_i y_i^2} \right]^{1/2} \tag{3.47}$$

- Reduced χ^2
$$\chi_\nu^2 = \left[\frac{R_{wp}}{R_{exp}} \right]^2 = \frac{\chi^2}{n-p} \tag{3.48}$$
where n is the number of 2θ step observed and $n-p$ the number of degrees of freedom of the refinement. This factor allows the comparison among refinements of the same structure, performed with the same model, but with a different number of refinable paramenters. Moreover χ_ν^2 is proportional to the function χ^2 minimized in the method.

- Bragg factor
$$R_B = 100 \frac{\sum_{\boldsymbol{h}} |I_{obs,\,\boldsymbol{h}} - I_{calc,\,\boldsymbol{h}}|}{\sum_{\boldsymbol{h}} |I_{obs,\,\boldsymbol{h}}|} \tag{3.49}$$

With the exception of the last item in the list, all the agreement factors presented are calculated using all the observed and calculated points, whereas the Bragg factor is calculated only using those points where there are Bragg contributions taken into account, moreover the Bragg factor is calculated

separately for each phase included in the model. The *observed* integrated intensities $I_{obs,\,\boldsymbol{h}}$ are not actually observed, in fact they are calculated using the Rietveld formula

$$I_{obs,\,\boldsymbol{h}} = I_{calc,\,\boldsymbol{h}} \sum_i \left\{ \frac{\Omega(2\theta_i - 2\theta_{\boldsymbol{h}})(y_i - b_i)}{(y_{c,\,i} - b_i)} \right\} \tag{3.50}$$

3.3.2 Structure factor

With respect to the formula presented in section 3.1.3, here we present a more general result for the structure factor, which is the one used by FullProf. It can be expressed as the sum of the crystallographic and the nuclear component:

$$F^2_{\boldsymbol{h}} = F^2_{c,\,\boldsymbol{h}} + J^2_{m,\,\boldsymbol{h}} \tag{3.51}$$

The crystallographic structure factor $F_{c,\,\boldsymbol{h}}$ is calculated by using the formula

$$\begin{aligned} F_{c,\,\boldsymbol{h}} \;=\; & \sum_{j=1}^{n} O_j f_j(\boldsymbol{h}) \exp\left(-B_j|\boldsymbol{h}|/4\right) \sum_{s=1}^{m} T_{js}(\boldsymbol{h}) \exp\left\{2\pi \mathrm{i}\left(\boldsymbol{h}^T S_s \boldsymbol{r}_j + \boldsymbol{h}^T \boldsymbol{t}_s\right)\right\} \\ & \times \exp\left\{-B_{ov}|\boldsymbol{h}|/2\right\} \end{aligned} \tag{3.52}$$

where n is the number of atoms in the asymmetric unit, m is the number of the reduced set of symmetry operators of the crystal space group. O_j is the occupation number factor, $f_j(\boldsymbol{h})$ is the scattering length, B_j is the isotropic temperature parameter and $\boldsymbol{r}_j$ is the position vector of atom j. $T_{js}(\boldsymbol{h})$ is the anisotropic temperature factor. B_{ov} is the isotropic overall temperature parameter.

The magnetic phase $J_{m,\,\boldsymbol{h}}$ is calculated using the general formula of Halpern and Johnson

$$J^2_{m,\,\boldsymbol{h}} = \left(|\boldsymbol{F}_m(\boldsymbol{h})|^2 - \left(\boldsymbol{e} \cdot \boldsymbol{F}_m(\boldsymbol{h})\right)^2\right) \exp\left\{-B_{ov}|\boldsymbol{h}|/2\right\} \tag{3.53}$$

where $\boldsymbol{F}_m(\boldsymbol{h})$ is the magnetic structure factor, $\boldsymbol{e}$ is the unit vector along the scattering vector $\boldsymbol{h}$ and B_{ov} is the isotropic overall temperature factor. The magnetic structures that can be refined with FullProf must have a distribution of magnetic moments that can be expanded as a Fourier series

$$\boldsymbol{\mu}_{lj} = \sum_{\boldsymbol{k}} \boldsymbol{S}_{\boldsymbol{k}j} \exp\left\{-2\pi \mathrm{i} \boldsymbol{k} \boldsymbol{R}_l\right\} \tag{3.54}$$

where l labels the cell within the crystal, j the atoms in the crystallographic unit cell, $\boldsymbol{k}$ is the propagation vector, $\boldsymbol{S}_{\boldsymbol{k}j}$ is the $\boldsymbol{k}j$ Fourier component and $\boldsymbol{R}_l$ is the position fo the l-th cell. In the case of the antiferromagnetic phase of

$EuTiO_3$ the magnetic unit cell is the same as the chemical cell and therefore the translational symmetry of the magnetic structure is identical to that of the crystal structure. In such a case the propagation vector is $\boldsymbol{k} = (0, 0, 0) = \mathbf{0}$. The Fourier coefficients are real and can be identified to magnetic moments directly:

$$\boldsymbol{m}_{lj} = \boldsymbol{S}_{\mathbf{0}j} \exp\left(-2\pi \mathrm{i} \mathbf{0} \boldsymbol{R}_l\right) = \boldsymbol{S}_{\mathbf{0}j} = \boldsymbol{m}_{\mathbf{0}j} \tag{3.55}$$

Back to the general case, if we also consider thermal motion and the the simmetry relations for coupling the different Fourier component $\boldsymbol{S}_{\boldsymbol{k}j}$ are established, we obtain the general expression of the magnetic structure factor

$$\begin{aligned} \boldsymbol{F}_m(\boldsymbol{h}) = \frac{\gamma r_0}{2} \sum_{j=1}^{n} O_j f_j(\boldsymbol{h}) \exp\left(-B_j |\boldsymbol{h}|/4\right) \\ \times \textstyle\sum_s M_{js} \boldsymbol{S}_{\boldsymbol{k}j} T_{js} \exp\left\{2\pi \mathrm{i} \left[\boldsymbol{h} \left\{S|\boldsymbol{t}\right\}_s \boldsymbol{r}_j - \psi_{\boldsymbol{k}js}\right]\right\} \end{aligned} \tag{3.56}$$

The largest part of terms in equation 3.56 has been already explained. Here we focus on M_{js} and $\psi_{\boldsymbol{k}js}$. M_{js} is the symmetry operators which transforms the Fourier component of the atom $j1$ suitably in all the equivalent position (labeled with s)in the crystallographic space group. The phase $\psi_{\boldsymbol{k}js}$ has two component

$$\psi_{\boldsymbol{k}js} = \Phi_{\boldsymbol{k}j} + \phi_{\boldsymbol{k}js} \tag{3.57}$$

$\Phi_{\boldsymbol{k}j}$ is a phase factor that is not determined by symmetry. It is a refinable parameter and it is significant only for an independent set of magnetic atoms with respect to another one. $\phi_{\boldsymbol{k}js}$ is a phase factor determined by symmetry, in fact the Fourier component $\boldsymbol{k}$ of the magnetic moment of atom $j1$, $\boldsymbol{S}_{\boldsymbol{k}j}$, is transformed to

$$\boldsymbol{S}_{\boldsymbol{k}js} = M_{js} \boldsymbol{S}_{\boldsymbol{k}j} \exp\left\{-2\pi \mathrm{i} \phi_{\boldsymbol{k}js}\right\} \tag{3.58}$$

3.4 Absorption correction

Due to the presence of Europium, $EuTiO_3$ strongly absorbs neutrons($\sigma_{abs}^{\mathrm{Eu}} = 4530\,\mathrm{b}$). This represents the very first challenge, which has to be overcome, to our experiment and to the following data treatment. Absorption leads to high counting time, in order to have intense reflections, and also distorts the intensities of reflections, introducing a particular angular dependence. Consider two different neutrons which scatter in the sample, the first being back-scattered and the second forward-scattered. On average, the forward-scattered neutron has an higher probability of being absorbed, owing to its longer path through the sample. Therefore the intensity of a peak at a given angle is affected from absorption, and the intensity of two peaks at two

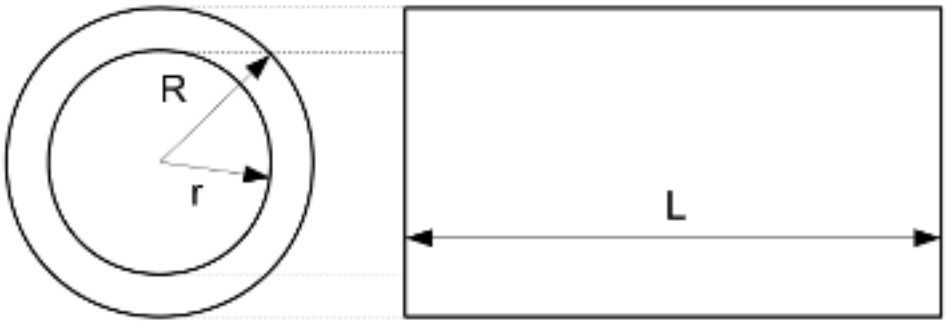

Figure 3.4: Schematic representation of the annular cylindrical sample holder.

different angles could be correctly compared only taking this into account. The absorption problem could be solved using enriched Eu instead of natural Eu, but the process of enrichment would be too expensive.

In order to increase the intensity of the signal, compatibly with the allowed experimental time, we decided to use a double walled sample holder, shown in figure 3.4, which decreases the neutrons path within the sample, decreasing then the absorption. The double walled sample holder is an experimental geometry not implemented in FullProf, which is only able to treat absorption in a simple cylindrical sample holder. The software accepts, as an input, a correction file in which we can write the correction for absorption, as two arrays, the first containing the angles and the second the correction factors for the given angles. Unfortunately, the absorption as a function of the diffraction angle in the case of a double walled sample holder (but also in the case of a simple cylindrical sample holder) cannot be written in an analytical form. Therefore we have to calculate numerically these correction factors.

3.4.1 Transmission factor

Transmission factors for neutron powder diffraction have been tabulated for several geometry situations, in particular for spherical, simple cylindrical and annular cylindrical sample holder[50, 51, 52].

Generally speaking the transmission factor is defined as

$$A(2\theta) = \frac{I(2\theta)}{I_0} \tag{3.59}$$

where I_0 is the intensity of the incident neutron beam, $I(2\theta)$ is the intensity of the diffracted neutron beam and θ is the Bragg angle. A is given by the integral

$$A = \frac{1}{V} \int_V \exp(-\mu l)\, \mathrm{d}v \tag{3.60}$$

where μ is the linear absorpion coefficient, V the total volume of the sample and l the total path of neutron through it. For diffraction in the equatorial plane from a cylinder of radius R, the transmission factor can be exactly calculated for only $2\theta = 0°$ and 180°[50]. For other values of 2θ, it must be obtained by numerical integration. The numerical integration is *a fortiori* required for the case of the double walled sample holder. In both cases (simple and annular cylindrical) can be found that the transmission factor at a given angle only depends from two parameters: μR (here R is the radius of the outer cylinder) and ρ, the ratio between radius of the inner and the outer cylinders[51, 52]. Schmitt and Ouladdiaf reported the transmission factor calculated for different Bragg angles, for integer values of μR ranging from 1 to 30 and for $\rho = 0.8$, 0.85, 0.90 and 0.95[52]. However the values reported in literature does not fit our case (which is presented is section 3.4.2). Thereafter we developed a new PYTHON code capable to perform the integral of equation 3.60, for any values of μR, ρ and 2θ. We checked the results of the new code and found coherent with those reported in literature. Finally we used the code for the case of interest. The most important task for such calculation is the determination of the total path length for a given Bragg angle θ. For each integration point, the actual neutron path in the annular cylinder is obtained by subtracting from the total path within the outer cylinder, the path corresponding to the inner cylinder if needed. In order to decide if this latter contribution must be subtracted, four cases must be considered, combining the possibilities for a neutron to go through the inner cylinder before and after the scattering event.

Because the purpose of this code is to arrange a useful tool for treating the data of a neutron diffraction powder experiment, we are interested in having a correction curve for 2θ ranging from 0° to 180°, for given μR and ρ. Although it is in principle possible to calculate the correction factors for an arbitrarily high number of angles in the range of interest, we decided to generate the correction curves interpolating twenty calculated points between 0° and 180°, making a trade-off between accuracy and computational time. We verify the sustainability of such restriction comparing a transmission curve interpolated starting from twenty points to one interpolated starting from two hundreds points. The maximum relative difference between the two curves, in the range of interest, is lower than 10^{-4}. This difference is acceptable for our case, because other measured parameters, e.g. the dimensions of the double

Quantity		
Cylinder outer radius	R	0.54(1) cm
Cylinder inner radius	r	0.40(1) cm
Cylinder length	L	6.1(4) cm
$EuTiO_3$ mass	m	3.83(1) g
Volume of the sample	V_{sample}	2.59 cm^3
Eu atoms per unit cell	n_{Eu}	4
Ti atoms per unit cell	n_{Ti}	4
O atoms per unit cell	n_{O}	12
Cell parameters	$a = b$	5.507 Å
	c	7.813 Å
Volume of the unit cell	V_{cell}	237 $Å^3$
Eu absorption cross section	σ_{Eu}	4530 b
Ti absorption cross section	σ_{Ti}	6.09 b
O absorption cross section	σ_{O}	0.00019 b
Density of $EuTiO_3$, crystal	$d_{\mathrm{EuTiO_3},\,crystal}$	6.95 g/cm^3

Table 3.1: List of physical and geometrical quantities needed to calculate the absorption parameters.

walled sample holder, have higher relative uncertainty[5].

3.4.2 Europium titanate absorption parameters

The code developed for dealing with every possible case of double walled sample holder, of course, could be used for the case of interest. Considering that only tho parameters μR e ρ define the absorption function, we have to calculate those parameters starting from the geometry of the sample holder and the mass of $EuTiO_3$. What is needed is listed in table 3.1.

First of all we can calculate the linear absorption coefficient of $EuTiO_3$ in the crystalline phase $\mu_{crystal}$ from

$$\mu_{crystal} = \frac{n_{Eu}\sigma_{Eu} + n_{Ti}\sigma_{Ti} + n_O\sigma_O}{V_{cell}} \tag{3.61}$$

where n_x is the number of x atoms in the unit cell of volume V_{cell} and σ_x its absorption cross-section. Secondly we have to consider that the sample is not an $EuTiO_3$ single-crystal, but it has been powdered, therefore, in order to

[5]For the measured parameters see table 3.1 on page 44.

calculate μR we have to take into account the packing fraction f given by

$$f = \frac{\frac{m_{\mathrm{EuTiO_3}}}{V_{sample}}}{d_{\mathrm{EuTiO_3},\,crystal}} \tag{3.62}$$

where $m_{\mathrm{EuTiO_3}}$ is the mass of powdered sample insert in the sample holder, V_{sample} its volume and $d_{\mathrm{EuTiO_3},\,crystal}$ the density of $EuTiO_3$ in the crystalline form. Multiplying equations 3.61, 3.62 by the external radius R of the sample (which is the internal radius of the sample holder), we finally get the parameter of interest

$$\mu R = f \mu_{crystal} R \tag{3.63}$$

Whereas ρ is simply given by:

$$\rho = \frac{r}{R} \tag{3.64}$$

where r is the internal radius of the sample. From equations 3.63 and 3.64 and the data in table 3.1, we get μR = 8.826 and $\rho = 0.738$.

As all the parameters measured are affected by uncertainty, also μR and ρ will be uncertain. In figure 3.5 all the parameters but one are kept fixed to their nominal values, the last is varied within its uncertainty region as declared in table 3.1.

The mass of $EuTiO_3$ (blue line) and the length of the sample holder (light-blue line) only act on the packing fraction of the sample, therefore they do not change the ρ value. To higher values of the mass correspond higher values of μR, whereas to higher values of sample holder's length correspond lower values of μR. The external radius R (green line) and the internal radius r (red line) influence both the μR and ρ in a form which seems to be similar, but by higher values of R we move downward along the green line and by higher values of r we move upward along the red line.

Of course this is a raw model because it let vary only one parameter keeping fixed the others, but allows us to understand that the variation of the mass of $EuTiO_3$ is negligible. So we can develop an analysis which allows all parameters varying within their uncertainty regions at the same time, but in this analysis we can neglect the contribution of the mass uncertainty. The result of this analysis is reported in figure 3.6. The twenty seven blue points sample the region of the μR-ρ space which is compatible with the uncertainty of the measured quantities. As shown the absorption parameters could vary up to a 4% for ρ and up to a 15% for μR from their nominal values.

3.4.3 Transmission curve of interest

In figure 3.6 we reported twenty seven points. For each of those we calculated the corresponding transmission curves. As explained in section 3.4.1, in order

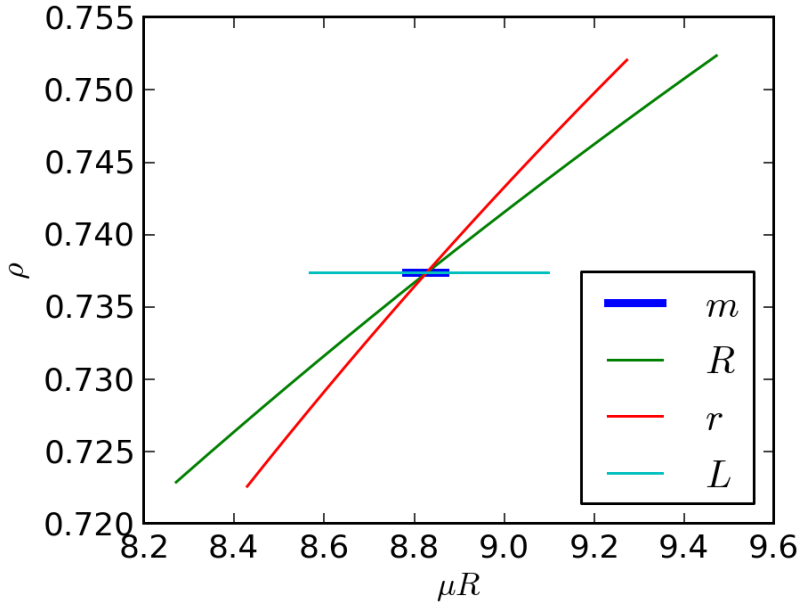

Figure 3.5: Dependence of the absorption parameters μR and ρ from the measured parameters, m, R, r and L, compatible with their uncertainty. For each of the parameters varying the others are kept fixed to their nominal values.

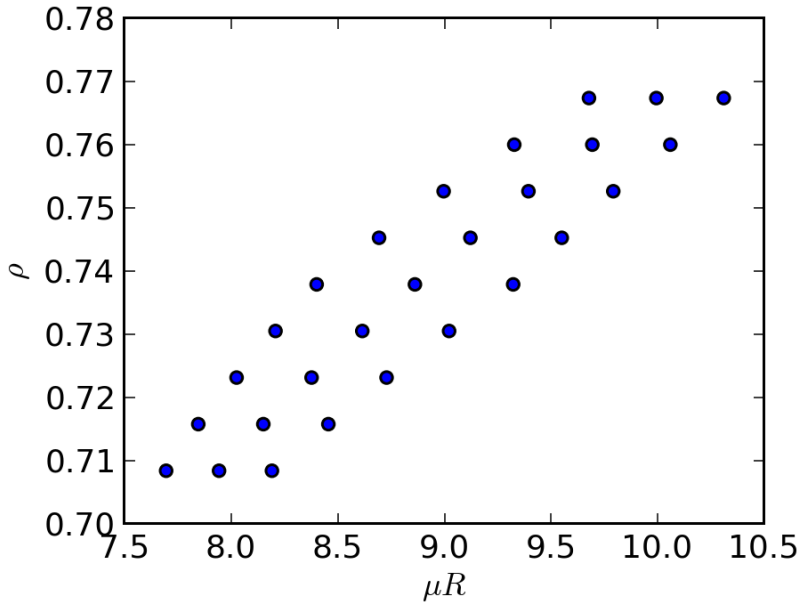

Figure 3.6: Sampling of the μR-ρ space compatible with the uncertainty on the measured parameters.

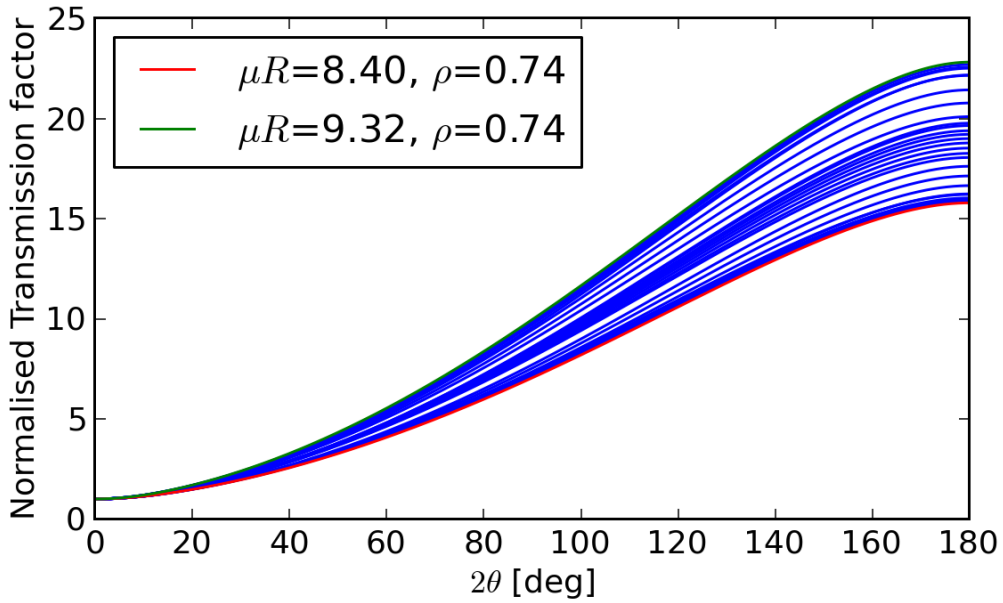

Figure 3.7: Normalised transmission curve compatible with the uncertainty on the measured parameters.

to obtain a single curve a non negligible computational time is required, therefore we choose only these twenty seven points to investigate the whole region of interest. The corresponding transmission curves are depicted in figure 3.7. From these curves we can extract the correction files *FullProf* needs to treat correctly $EuTiO_3$ absorption in our case. The curves are normalised: for each of them the transmission at $2\theta = 0°$is 1. The code developed for the calculation of these curves usually returns a non-normalised curve, in which the value of the transmission could be interpreted as the probability for a neutron, scattered at a given angle, to be not absorbed during his path through the sample. The reason why the curves are presented normalised is related to the way FullProf refines the data. In FullProf the very first parameter which is refined is a scale factor which uniformly applies at the model at all scattering angle. Let's assume that two transmission curves only differ for a multiplying constant, then if they are used for a refinement, the two results will be equivalent. The only difference would be the scale factor. For this reason what matter for the refinements is not the absolute value of transmission, but the relative value of the transmission at two different angles. Considering that all the curves are normalised at $2\theta = 0°$, we can

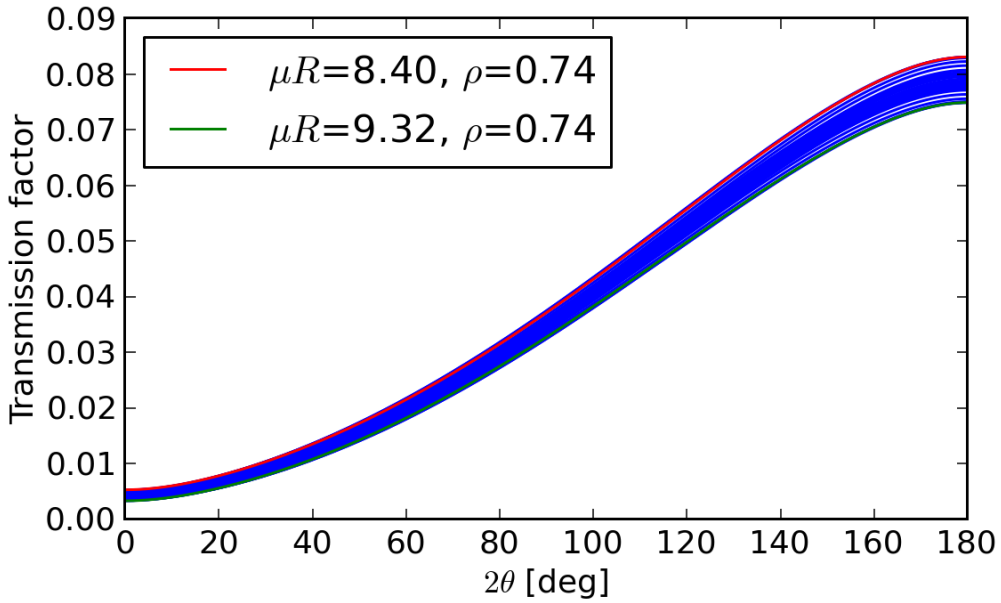

Figure 3.8: Non normalised transmission curve compatible with the uncertainty on the measured parameters.

distinguish the curves by the transmission at $2\theta = 180°$. We can observe that there are two *extreme* correction which correspond to the same value of ρ (0.74) and two different values of μR (8.40 and 9.32). The transmission curves of these two corrections are colored in figure 3.7. The green line (at the top) represents the curve for the higher value of μR, whereas the red line (at the bottom) represents the curve for the lower value of μR. Of course for higher values of μR the absorption is stronger as can be seen in figure 3.8, where the transmission curves are displayed non-normalised. The correct information that can be derived from figure 3.7 is only that for higher values of μR the neutrons scattered at higher angles are less absorbed with respect to those scattered at lower angles. This as expected from the relative path through the sample, longer for smaller diffraction angles. It is important to point out that both the *extreme* corrections are obtained for the same values of ρ. Therefore in order to explore all the possible corrections within the μR-ρ space, compatible with the uncertainty on the parameters, we can reduce the investigation to different points with $\rho = 0.74$, which actually is only 0.4% higher than the nominal value, and μR varying between the values allowed for the given ρ. The points selected are shown in figure 3.9.

In the previous simulation (figure 3.6) there are three points for the ρ of interest (0.74) with μR between 8.40 and 9.32. In figure 3.9 there are seven points with μR between 8.16 and 9.61, plus a point for μR = 7.70 for reasons which will be clear in the next chapter. To these eight points correspond the eight transmission curves which are shown in figure 3.10. These curves can be considered a good representation of all the possible transmission curves compatible with the uncertainty on μR and ρ, therefore these will be used to generate the correction files needed for the refinements.

3.5 Data and calculated profile correction

At the beginning of the current section, we introduced the purpose of the calculation of the correction factor: provide a correction file which can be used by FullProf. Generally speaking two options are available. First, it is possible to correct the collected data for absorption and perform a Rietveld refinement, supposing a non-absorbing sample. Second, to perform the refinement of raw data, specifying to the program how to correct the calculated model, to take into account absorption. In figure 3.11 we investigate the differences between the two procedures. In the upper left panel, the raw data are presented. The behaviour of an absorbing sample is evident due to the increasing intensity of the diffracted peaks with the Bragg angle. To make this behaviour even more evident should be considered that the very first peak is not a reflection, but are counts corresponding to the diffusion (air and sample environment) of the direct beam, and that the intense peak around 40°, it is not due to $EuTiO_3$, but to the sample environment. Actually it is a Bragg reflection due to the crystallites of the vanadium sample holder. In the upper right panel is shown the simulation of the diffraction pattern of a fictitious non-absorbing $EuTiO_3$ sample. The lack of the absorption is testified by the flat behavior of the reflections. In the left lower panel the absorption correction is directly applied to the measurements. The inconsistency of the solution is self-evident. The background is strongly enhanced at low angle and, on the other hand, the reflections for large scattering vectors are still too low (with respect to the theoretical pattern shown in the right upper panel). A better result can be obtained subtracting before a linear interpolated background and then applying the correction. However due to the impossibility of an exact subtraction of the background, its variance is still increased, and the best solution is to apply the correction to the calculated pattern, as shown in the right lower panel.

Giving the correction file as an input to FullProf, let us to manually control the C factor of equation 3.43, applying the correction Bragg peaks,

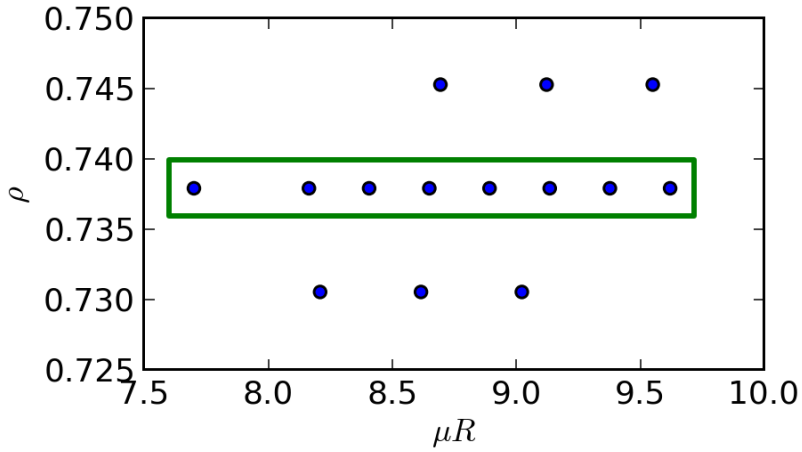

Figure 3.9: Points of interest within the region compatible with the parameters' uncertainty. The correction curves corresponding to the points enclosed in the green rectangle can be considered a good representation of all the possible transmission curves compatible with the uncertainty on μR and ρ can be considered a good representation of all the possible transmission curves compatible with the uncertainty on μR and ρ.

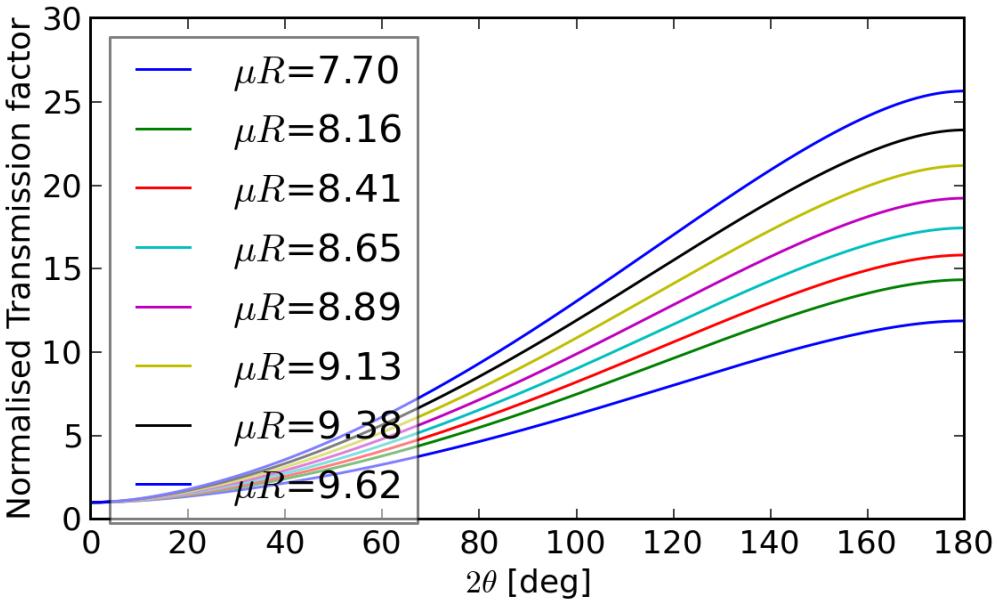

Figure 3.10: Normalised transmission curves corresponding to the points of interest within the region compatible with the parameters' uncertainty.

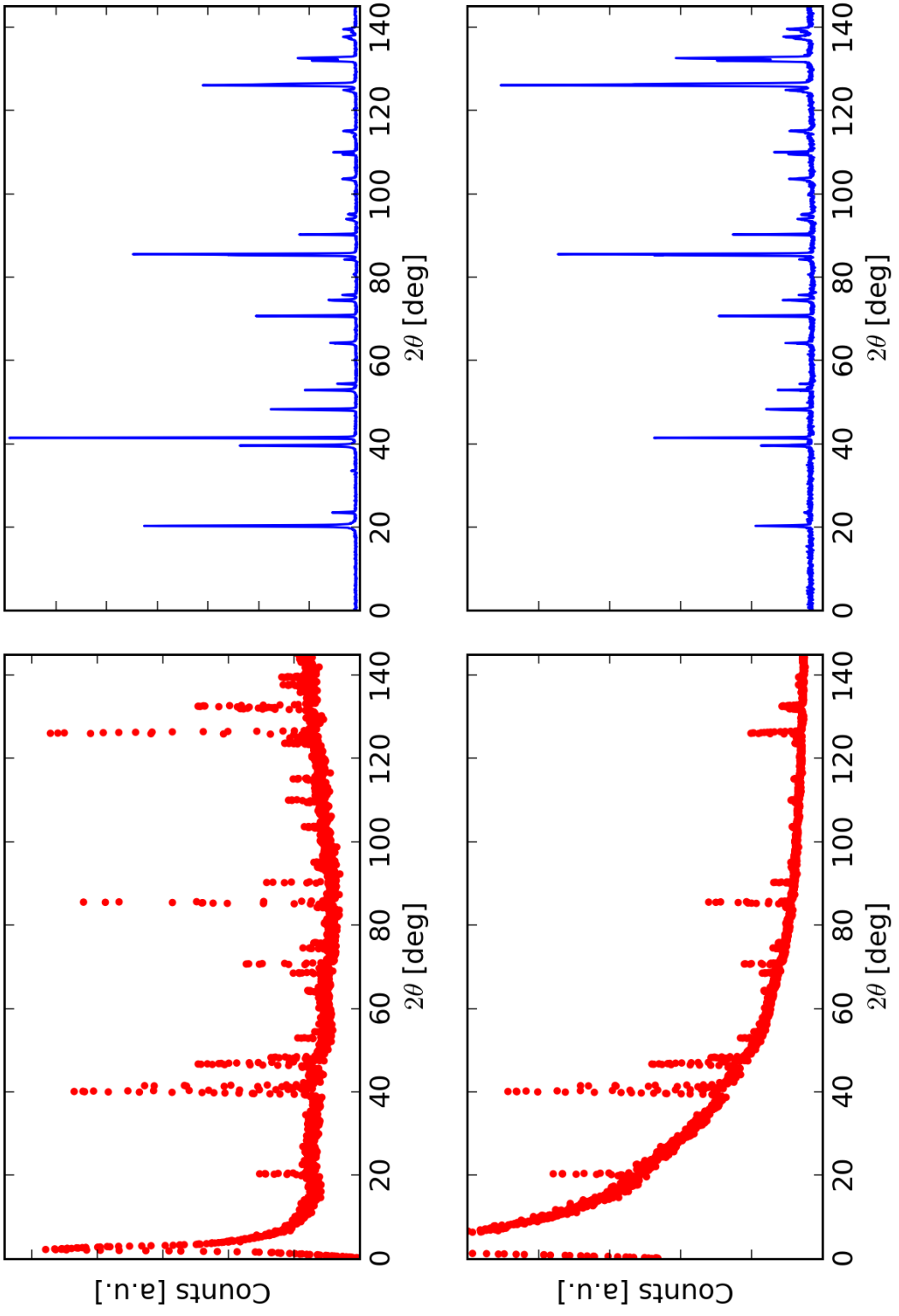

Figure 3.11: Results of the application of the correction factors to data and to calculated pattern. In the left upper panel the neutron powder diffraction on $EuTiO_3$ presented in chapter 4 are shown, whereas in the right panel the calculated pattern of the diffraction pattern without absorption is depicted. In the lower panels the correction is applied, on the left to the data, on the right to the calculated pattern.

but not to the background, which is added to the model after the correction, as defined in equation 3.42.

Chapter 4

Measurements and results

4.1 Sample preparation and characterization

The sample was grinded directly at Institute Laue-Langevin in Grenoble (France), where the measurements have been performed. $EuTiO_3$ was always kept in controlled atmosphere during all the processes. We were concern of preventing oxidation or contamination of the compound during its delivery, and its preparation. A fraction of the $EuTiO_3$ available was insert in the double-walled sample holder in a glove-box. This sample was used for the neutron powder diffraction experiment (presented in section 4.2), the remaining for other characterization measurements.

Among these characterization measurements we performed X-rays powder diffraction at ID15 beamline at ESRF in Grenoble[53]. Those measurements were performed at several temperature between 90 K and 400 K. The purpose was to check that the crystalline structure at room temperature and at low temperature is the one reported in literature. Cubic space group $Pm\bar{3}m$ above 282 K, and tetragonal space group $I4/mcm$ under 235 K[1]. For each temperature a series of images of the diffracted photons were collected with a two-dimensional detector. One of these images is shown in figure 4.1. The rings of the Bragg reflections are clearly visible.

The methods of analysis of powder diffraction experiment usually apply to a one dimensional profile. In this profile the diffracted intensity is reported versus the scattering angle. Therefore starting from the image of figure 4.1, we performed azimuthal integrations over the rings, in order to obtain the 2θ-dependency of the diffraction peaks and use the PDF method to solve the structure. The azimuthal integrations were performed using a new PYTHON package called PYFAI[54]. Those data are still in the process of

[1]The crystal structure of $EuTiO_3$ is discussed in section 2.2.

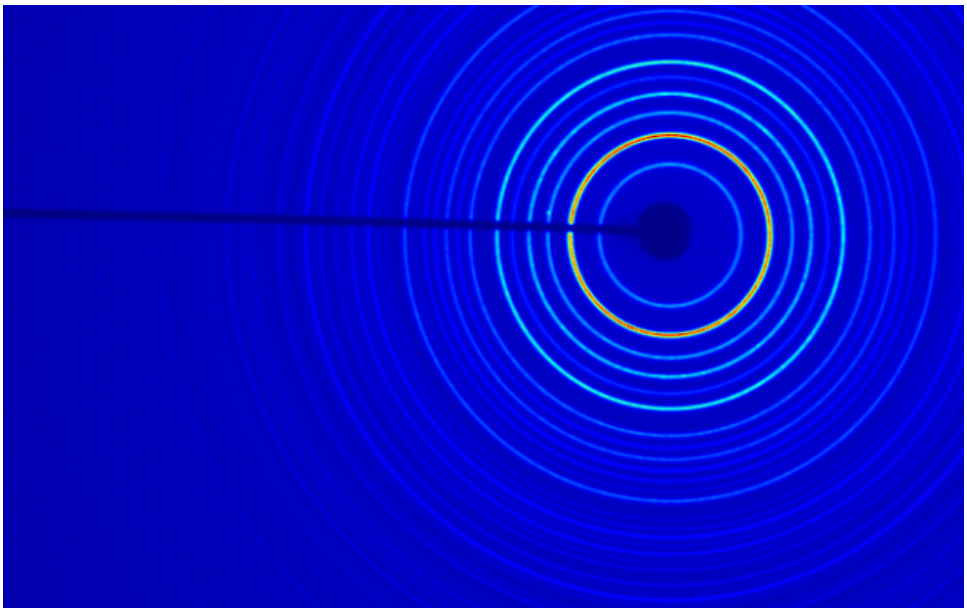

Figure 4.1: Image of diffraction rings of $EuTiO_3$ collected at ID15 beamline at ESRF.

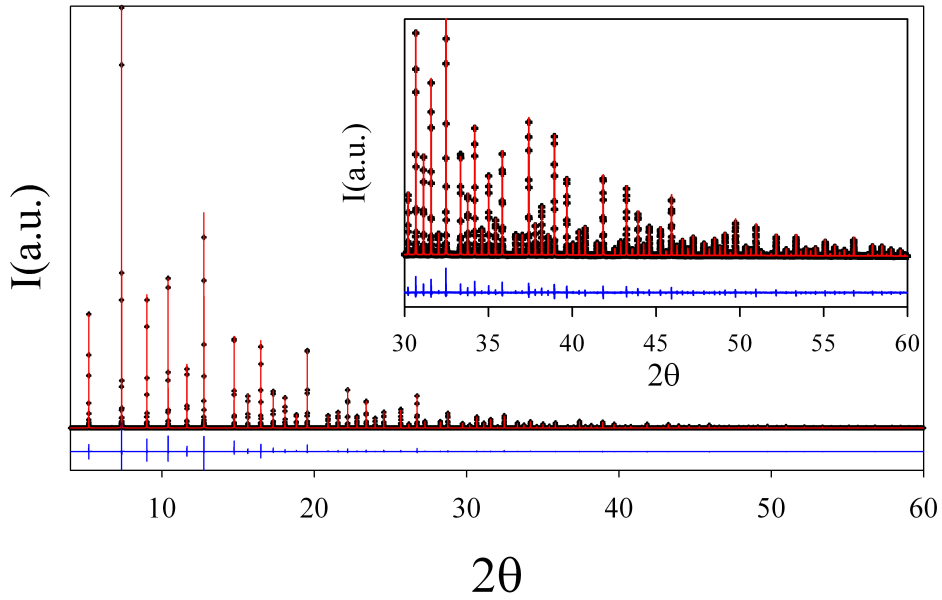

Figure 4.2: Diffraction patterns collected at room temparature of $EuTiO_3$ at ID31 beamline at ESRF. Black symbols are the experimental data, the red line is the calculated pattern and the blue line is the difference between the two.

being analysed, but a room temperature measurement has been performed at ID31 beamline at ESRF by our collaborators to our $EuTiO_3$ project from Università degli Studi of Milan.

The collected data and the Rietvield refinement are depicted in figure 4.2. The room temperature structure of this sample has been found consistent with the sample studied in Ref. [3]. Therefore we concluded that the room temperature of our sample is $Pm\bar{3}m$, and reasonbly assumed the low temperature structure to be $I4/mcm$. The figure shown let us briefly discuss the difference between X-ray powder diffraction and neutron powder diffraction, whose results are represented in figure 4.5.

Firstly neutrons interact with the nuclei in the scattering system, whereas X-rays interact with electrons. This leads to a different Bragg-angle dependence of the diffracted intensities of the two techniques, because the form factor contains the Fourier transform of the scattering system. If we deal with nuclear scattering, the physical dimension of a nucleus is little compared with the wavelength of the incoming nuetron and the form factor will be a constant; whereas if we deal with electron scattering, the Fourier transform of the electron density (whose displacement is much larger than the nuclear one), and consequently the Bragg peaks, will decrease with 2θ. Secondly, neutrons, due to their spins, are sensitive to the magnetic moments of the atoms of the sample, and can therefore be used to solve magnetic structures[2]. Thirdly figure 4.2 let us appreciate the instrumental advantages of X-rays. The dinamical range is impressively high: very intense peaks are superimposed to a very low background. The very-high resolution provides extremily sharp reflections. The high flux of synchrotrones sources allows to collect diffraction patterns with counting time lower than neutron case.

A small quantities of the sample was also measured by SQUID (Superconductive QUantum Interference Device) in Dipartimento di Fisica e Scienze della Terra "Macedonio Melloni" of the Università di parma, PaRMA group. The measurements are shown in figure 4.3. In panel (a) the antiferromagnetic phase is revealed by the temperature dependence of the magnetization at very low temperature and the Néel temperature, $T_N = 5.5$ K, is identified by the clearly visible anomaly. Panel (b) focuses on the paramagnetic phase of $EuTiO_3$. Fitting the blue points (from T 65 K $\div$ 300 K) with a function of the form

$$\frac{1}{\chi} = \frac{1}{C}(T - T_W) \tag{4.1}$$

we get $C = 3.6(0.3)\cdot 10^{-2}$ emuK/g and $T_W = 3.1(1.5)$ K. The Weiss tempereture

[2]Actually X-rays magnetic scattering is nowaday a widely used tecniques in synchrotrones, but the magnetic signal cannot be detected in the experimental setup used at ID31.

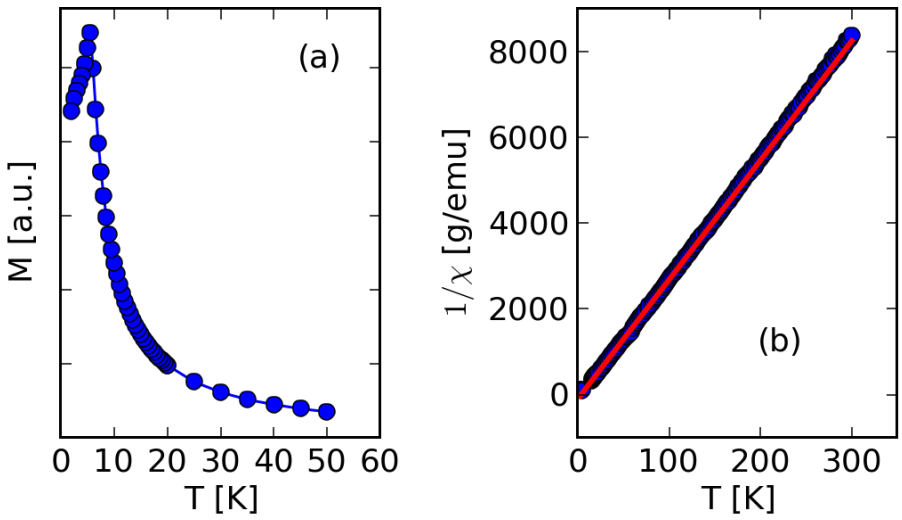

Figure 4.3: Magnetic characterization of $EuTiO_3$ sample. (a) Magnetization temperature dependence and (b) reciprocal of the magnetic susceptibility temperature dependence.

is uncertain due to the fact that the interpolation is perform far away from the transition, but it is consistent with the Néel temperauture previously identified. The Curie constant let us to evaluate the magnetic moment of europium atoms as $\mu = 8.4\ \mu_B$, which is actually higher than the values reported in literature around $7\ \mu_B$[29]. However, in spite of the values reported in literature, the theoretical value, compatible with the expected electronic configuration of the free ion Eu^{++} is $\mu = g\sqrt{J(J+1)} = 7.93\ \mu_B$ and it compare well with our experimental result. In fact Eu^{++} normally has bigger magnetic moment due to its electronic perculiarities.

4.2 Measurements

The neutron measurements have been performed at D2B beamline at the Insitute Laue-Langevin in Grenoble, France. D2B is a high-resolution powder diffractometer whose resolution is limited only by powder particle size ($\frac{\Delta d}{d} \sim 5 \cdot 10^{-4}$). Such a high resolution was needed in order to resolve between the two proposed antiferromagnetic structures of $EuTiO_3$ (described in section 2.3). Four measurements have been perfomed. The neutron wavelength was set at $\lambda = 1.595$ Å for the entire data set. A preliminary measurement in the

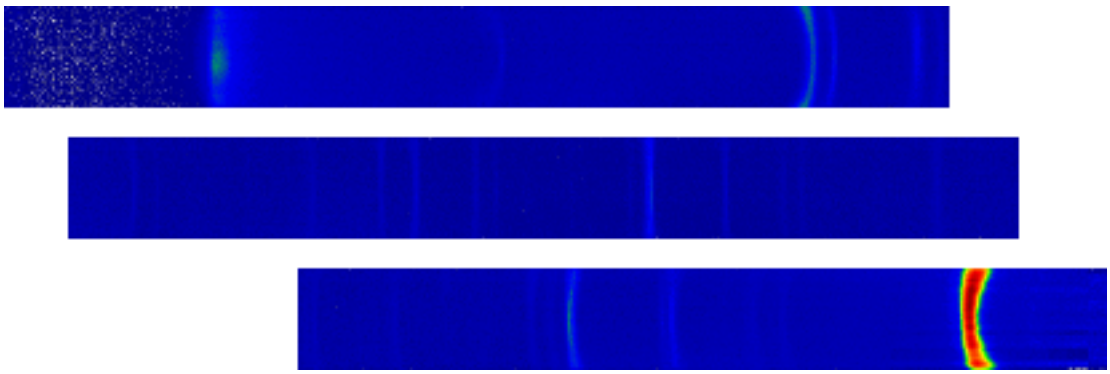

Figure 4.4: Image of a single scan collected on $EuTiO_3$ sample at D2B beamline at ILL. The scan has been cut into three slices for printing need.

high flux mode (10^7 neutrons/s), at 3.5 K, was taken to check the powder for the presence of contaminants and the actual absorption of the sample in order to determine the measurement time for the following acquisitions. Thereafter a set of three measures at very high-resolution were taken. Slits 200 were introduced. The slits reduces the angular dispersions of the neutron beam improving the resolution but reducing the flux (10^6 neutron/s). This set-up was chosen as a trade-off between the requirement of high resolution and time constrain. Priority was given to the set-up ensuring highest resolution at low angles were the magnetic contribution is stronger, and were the peaks discriminating between to proposed magnetic structures are localized. The first measure was performed at 3.5 K, then the second at 1.6 K, and the last at 3.5 K again. All the measurements in high resolution mode took roughly 24 hours, no more temperature points were then compatible with the available experimental time. In figure 4.4 the image of single scan collected on $EuTiO_3$ is shown. The detector height is approximately 30 cm. In order to improve the resolution the integrations of the diffraction rings[3] were performed only on the central 10 cm of the detector. Then all the single scans of a single measure were averaged and the results are shown in figure 4.5. The two different measures at 3.5 K, one before and the other after the one at 1.6 K, were carried out in the possibility of the existence of an hysteresis cycle in the phase diagram (if two different antiferromagnetic phase exists). However the two measurements at 3.5 K does not show any relevant differences, therefore there is not any evidence of an hysteris cicle. This can be evicend looking at the difference between the two measurements (blue line in figure 4.5). This let us consider the two different measures describing the same phase,

[3]Actually due to the height of the detector only archs are visible.

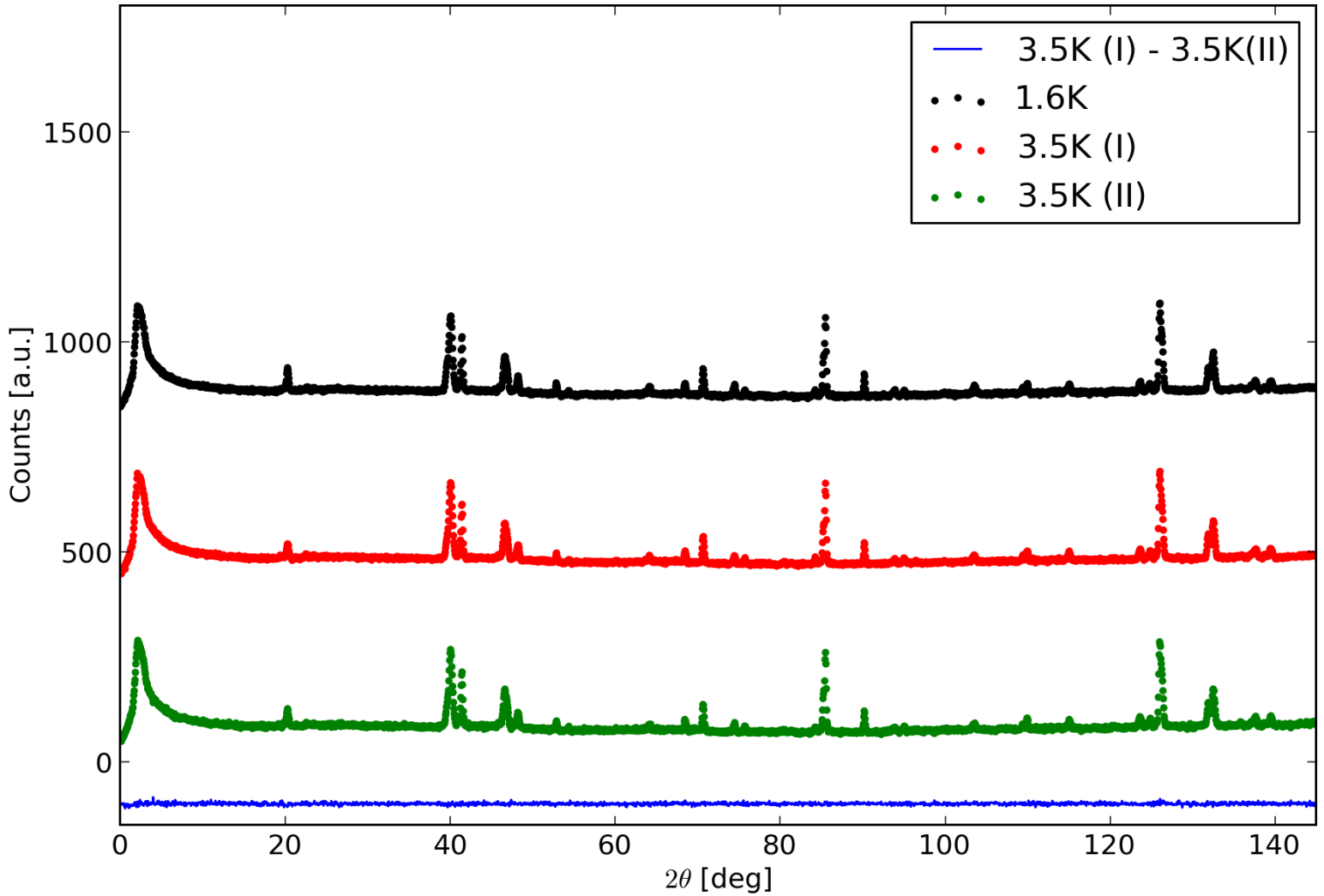

Figure 4.5: Neutron powder diffraction on $EuTiO_3$. The difference between the 3.5 K data before (red point) and after (green point) the measure at 1.6 K (black point) is shown (blue continous line). Data are shifted and shown up to 145° for clarity(a very intense peak due to the sample holder at higher Bragg angle have been excluded).

therefore we averaged them. The averaged data at 3.5 K correspond to an equivalent measurement of roughly 48 hours. This lead to an improvement of the signal-noise ratio, important at this temperature for two main reasons. Firstly because the magnetic signal is lower at higher temperature due to the decrease of the mean value of the magnetic moment approaching T_N. Secondly because the measure at 3.5 K is crucial to the purpose of our investigation, because it is at this temperature that doubts have been raised on the magnetic structure of $EuTiO_3$.

In figure 4.6 is shown the difference between the measure at 1.6 K and the measurement at 3.5 K. The peaks corresponds to reflections changing their intensities with temperature. This identifies the magnetic reflections, or at least the reflections with a magnetic contribution, especially at low angle where the magnetic scattering is stronger.

4.3 Refinements

We recall that this analysis has been done in order to contribute to the determination of the crystallographic and magnetic structure of $EuTiO_3$. Within all the information which can be obtain by Rietveld refinement, we are focused on the determination of the orientation of the spins localised on Eu atoms. To perform a Rietveld refinement an hypothesis of the structure is required. This made the method adequate to our case. In fact the crystallagraphic unit cell have been proved to belongs to $I4/mcm$ space group below 235 K, after the cubic to tetragonal transition. The antiferromagnetic ordering is reported to be Γ^9 (spin moments in the *a, b* plane) at 1.6 K by all the authors and reported to be Γ^9 from Scagnoli *et al.* and Γ^6 (spin moments slong the *c*-axis) from Petrovic *et al.* at 3.5 K. The strategy is therefore to refine the data with both the proposed structure at both temperature. From the refinement at 1.6 K we will be capable to see whether the resolution is sufficient to distinguish the two structure. If so, from the refinement of 3.5 K data we will be capable to determine which of the two magnetic structure is in better agreement with the experimental data.

4.3.1 Preliminary

It is first of all necessary an evaluation of the *background*. FullProf provides different solutions: determination from refinable background functions, or linear interpolation between manually selected points. We chose the second.

Secondly we have to consider that the neutrons measured by the counters are not only due to the scattering processes which take place in $EuTiO_3$

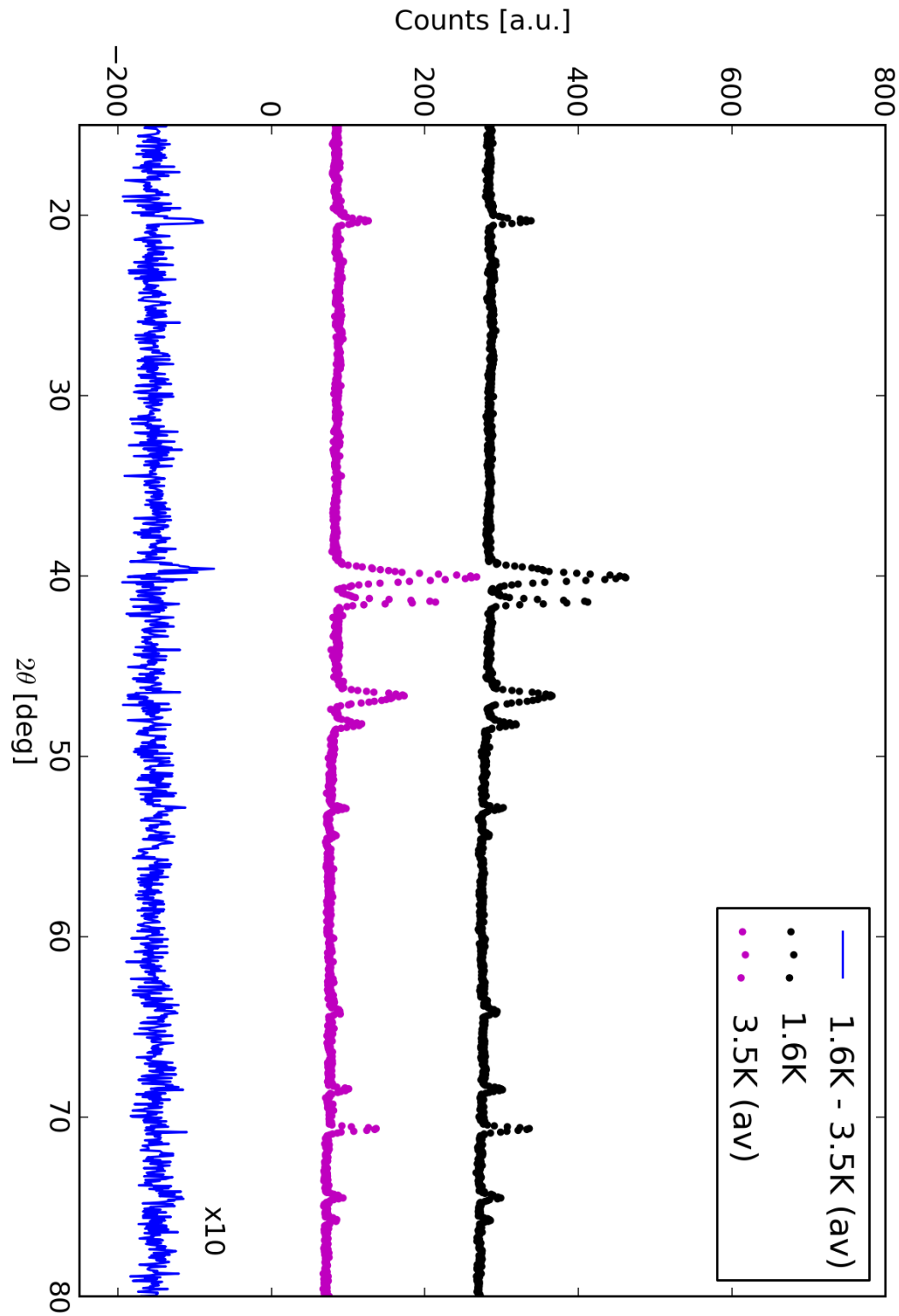

Figure 4.6: Data are shifted and the difference between the two measurements is amplified.

T = 1.6 K		T = 3.5 K	
$2\theta_i$	$2\theta_f$	$2\theta_i$	$2\theta_f$
-0.10	10.00	-0.10	15.00
39.20	48.75	39.20	49.65
68.00	68.91	68.00	68.91
123.23	124.22	123.23	124.22
145.00	180.00	145.00	180.00

Table 4.1: Region excluded from the refinements.

sample. Neutrons can reach the detector without any reflection or after being scattered by other materials in the sample environment. Contributions can be found from the sample holder or from contaminants accidentally drop in the sample holder. Therefore, before performing the refinements, it is crucial to identify these contributions and neglect the corresponding regions during the refinement process. Through a first refinements at both temperature, we detected these contributions, that can be located far from the $EuTiO_3$ peaks, or in the worst case in the same position. Table 4.1 presents the list of the *excluded regions* for the two temperatures.

The first excluded region is related to the neutrons of the incident beam, which go through the sample without scattering. This region extends up to 10°, due to the size of the beam spot. The other regions, but the last, are owed to the vanadium and alluminium Bragg peaks. These materials are present because constitute the sample holder. The last region has been excluded because of the vanadium and alluminium contributions become dominant with respect to $EuTiO_3$ peaks.

4.3.2 1.6 K

We first see the results of refinements at 1.6 K with Γ^9 as magnetic structure. The refinements have been performed using the correction factors obtained as described in section 3.4.3 from curves depicted in figure 3.10. For each possible correction different combinations of parameters have been refined.

In FullProf the crystallographic and the magnetic structure are described as two separated phases. Although there are significant differences between the declaration of structural phases from magnetic ones, we can state that for each phases the following parameters are defined:

- space group and related symmetry operations;

	Peak shape	B_{iso}	B_{ov}
zero	same	same	none
tp	diffent	same	none
biso	different	different	none
1bov	different	none	same
2bov	different	none	different

Table 4.2: Refinement combinations description.

- atoms within the cell: position, thermal motion parameters (B_{iso}) and magnetic moment (in magnetic phases only);
- scale factor;
- overall thermal motion parameter B_{ov};
- peak shape parameters ($U,\ V,\ W,\ X,\ Y$);
- lattice parameters ($a,\ b,\ c,\ \alpha,\ \beta,\ \gamma$).

Other parameters describing strain, preferred orientation of the crystallites within the powder and asymmetry in the peak shape can be declared, but we neglected these effects in our analysis. With the exception of the first item in the list (the space group and its related symmetry operations) all the other items are parameters that can be refined, accordingly to the space group constrains. The refinements of crystallographic and magnetic phase are performed at the same time, but no constrain is imposed by the software between the two phases, if any is required it must be given by the user. By constrain we mean, for example, that two refinable parameters belonging to the two phases have to be refined to the same value. We forced to the same values between the two phases the atoms' positions, the scale factor and the lattice parameters for all the refinements perfomed. For the other parameters we tested different possible configuration summurised in table 4.2. In zero combination the peak shapes and the B_{iso} between the two phases are forced to be the same.[4] In tp combination only the B_{iso} are forced to be the same. In biso all the parameters are free between the two phases. In these three combinations no use of B_{ov} has been made, because its usage is alternative to B_{iso}. In 1bov and 2bov, same and different B_{ov}, respectively, have been used, different peak shape parameters and B_{iso} have been kept to zero.

[4]Actually in the magnetic phase only the europium atom is present.

The agreement factors for the described refinements are presented in figure 4.7. In the upper panel the reduced χ^2_ν is presented. This factor decreases with μR for all the combinations presented. The highest values of χ^2_ν, which means the worst agreement between the observed and the calculated profiles, are shown by the 1bov combination, whereas the best agreement is shown by biso combination. This is far from being surprisingly because the biso combination leaves to FullProf the highest degree of freedom for the refinement, while the 1bov combination leaves the lowest.

The central and the bottom panel show the Bragg Factor R_B for the structural and magnetic phases. The Bragg factor for the structural phase remains in a range between 8.30 and 8.70 for all the combinations. On the other hand the Bragg factor for the magnetic phase shows a greater dependence from the combination chosen. For 1bov this agreement factor ranges from 34 to 38, wheras for biso it ranges from 20 to 24. The quality of the refinement of the magnetic phase strongly influences the quality of the overall refinement. In fact the worst magnetic agreements coincide with the worst global agreements and the best magnetic agreements coincide with the best global agreements.

However the agreement factors alone cannot suggest the strategy and indicate the best refinements. In figure 4.8 are shown the values of the individual isotropic thermal parameters for all the atoms in the cell. The values returned by the refinements are mostly non-sense values. First of all these parameters must be positive and secondly they usually are no greater than $5 \cdot 10^{-1}$ for temperature of a few Kelvin. For these reasons we decided not to refine B_{iso} and we restricted the description of the thermal motion to $B_{overall}$. In figure 4.9 the values of $B_{overall}$ for the 1bov and 2bov combinations are presented. The blue points correspond to 1bov, whereas the green and blue points correspond respectively to the crystallographic and magnetic B_{ov} of 2bov combination. The data show too high values for the B_{ov} of the magnetic phase, therefore we must opt for the 1bov configuration for all the refinements, despite of the fact that, among the ones proposed, is the one which leads to the worst agreement between the data and the refined profile. We particularly refer to the Bragg factor of the magnetic phase, because the variation of χ^2_ν is less then a 5%.

Further information can be found in the thermal parameters behaviour. Let us consider the μR dependence of those parameters, they all increase with the increase of the correction parameter μR. This can be explained comparing the dependence of the correction factor and the Debye-Waller factor from the scattering vector. For higher Bragg angles (larger scattering vectors) the Debye-Waller factor decreases, reducing the form factor. For higher μR the correction factor amplifies more the calculated profile at higher Bragg

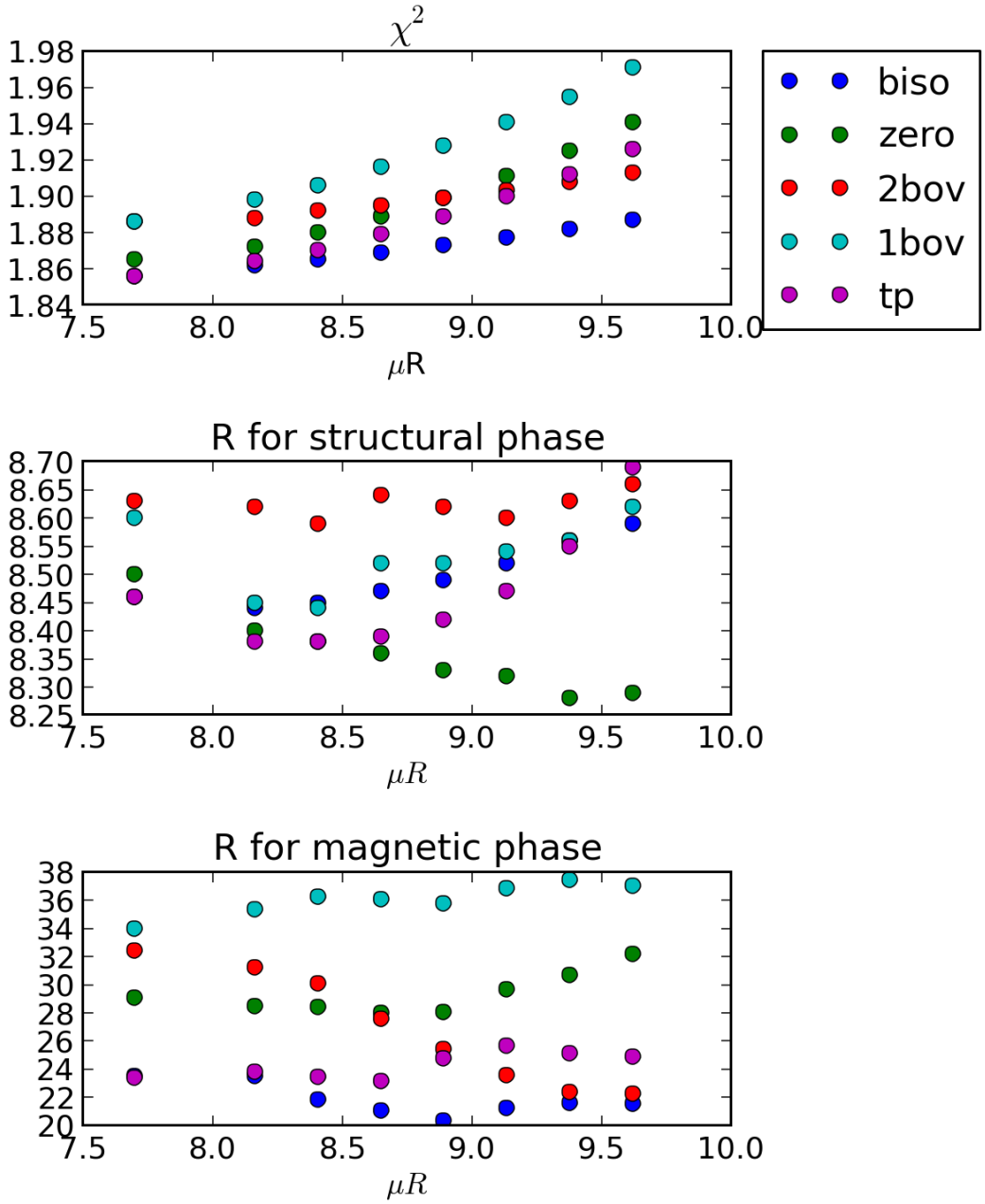

Figure 4.7: Agreement factors of the Rietveld refinements at 1.6 K for the absorption corrections proposed.

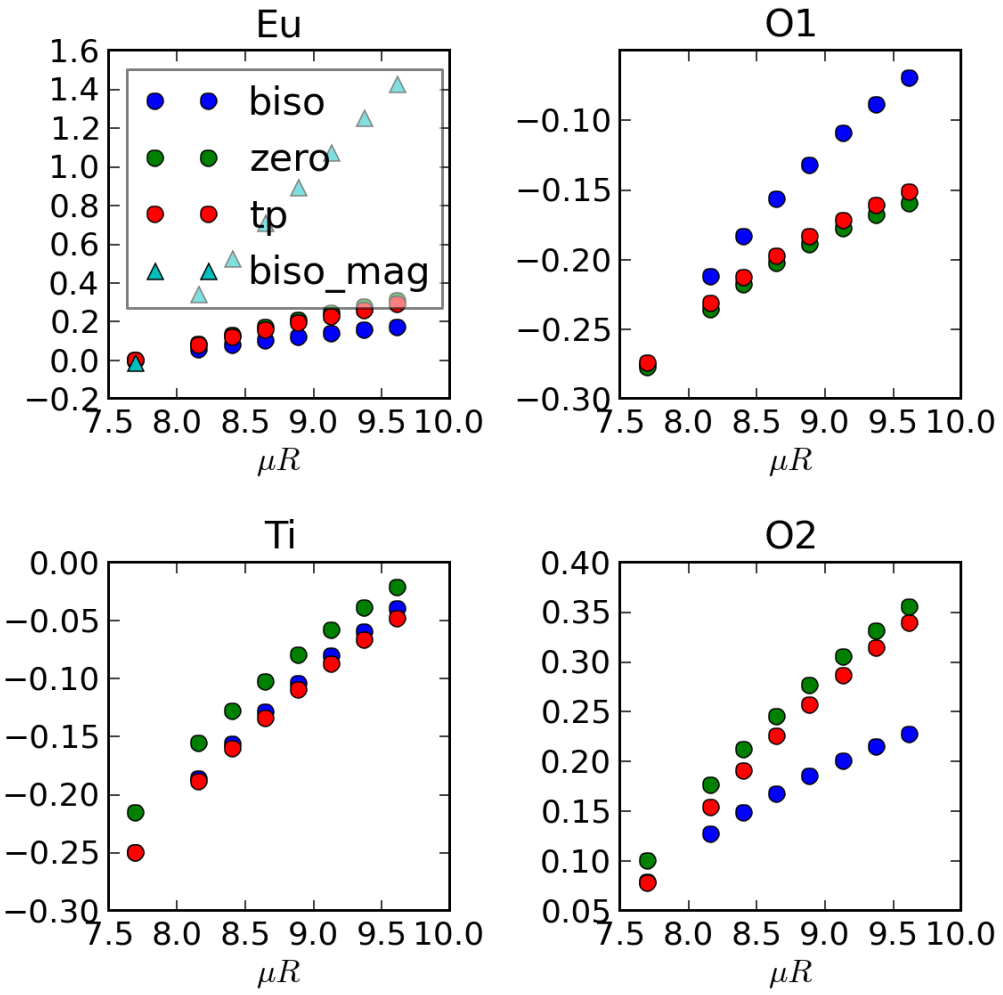

Figure 4.8: Refined individual thermal motion parameters at 1.6 K for the absorption corrections proposed.

angles with respect to lower Bragg angles. Therefore the most the correction enhances, for large scattering vectors, the calculated profile, the most the thermal parameters counteract this effect. The crystallographic phase is less sensible to this effect than the magnetic phase. In fact the structural Bragg factor for the 2bov combination is even higher than the one for the 1bov combination. On the other hand the magnetic phase is strongly affected by the binding of the overall thermal parameters between the two phases.

Let us consider the information on the thermal motion parameters together

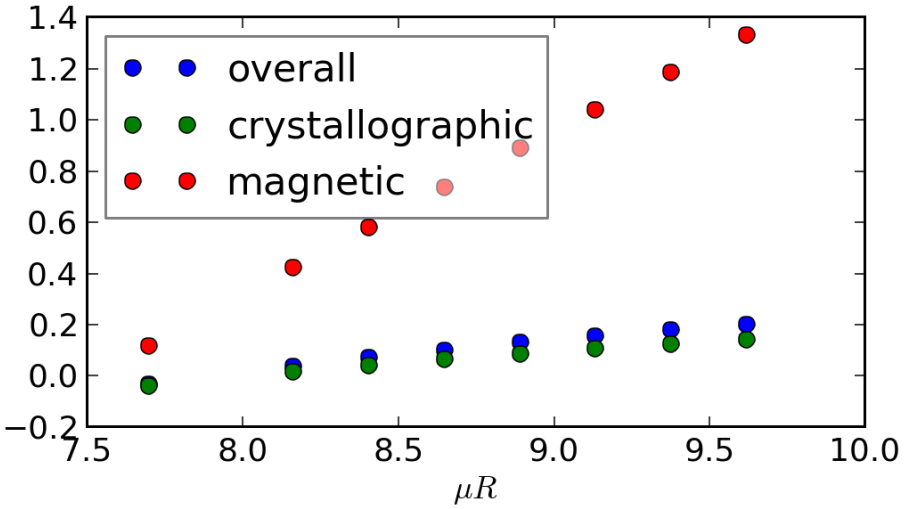

Figure 4.9: Refined overall thermal motion parameters at 1.6 K for the absorption corrections proposed.

with the behaviour of the magnetic moment depicted in figure 4.10. All the

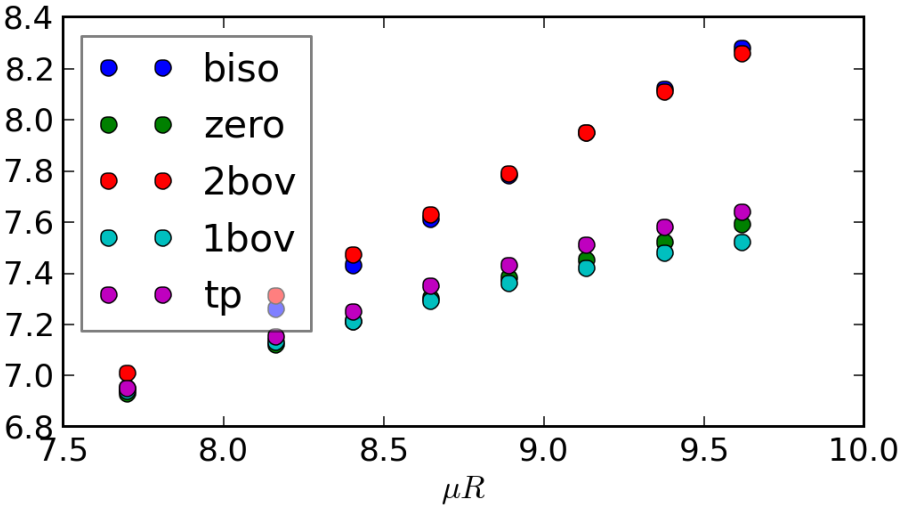

Figure 4.10: Refined magnetic moment at 1.6 K for the absorption corrections proposed.

combination are presented and for all of them the magnetic moment increases

with μR. This is coherent with the description above, in fact for higher μR the correction factor reduces the intensity of the peaks at low angles and higher magnetic moments counteact this effects. But if an higher magnetic moment is used to improve the quality of the refinement at low angles, then higher thermal motion parameters have to be used to improve the quality of the refinement at high angles.

The magnetic moment raises our attention also for its values. We must remember that the magnetic moment which is determined with a diffraction experiment is the mean value within the sample. In the case of an antiferromagnet the moment measured is referred to the average one on one of the two ferromagnetic sublattices which build the antiferromagnet.
The average magnetic moment is strongly temperature dependent. In fact it falls rapidly to zero when temperature approachs the Néel temperature, which is $T_N = 5.5$ K. We can calculate the expected value of the magnetic moment for T between 0 K and the Néel temperature with the critical exponent model[55]. The magnetic moment is given by

$$\mu(T) = \mu(0)\left(1 - \frac{T}{T_N}\right)^{\alpha} \tag{4.2}$$

We assume to be correct the value at 0 K proposed in literature[29] ($\mu = 7.0$ μ_B) and set $\alpha = 1/3$ (which is the value experimentally observed[55]). The magnetic moment at 1.6 K shoud be 6.24 μ_B, which is actually lower than the refined values which ranges from 7 μ_B to 8.2 μ_B. Looking at figure 4.10 is also clear the reason we decided to calculate the correction factor and perfomed the refinements for μR = 7.7, although this value is hardly compatible with the experimental uncertainty. The attemp was to bring the magnetic moment value closer to its theoretical value, however this leads to negative value the overall thermal motion parameters.

The value of the magnetic moment of the europium ion have been reported by several authors[29, 5], therefore we performed refinements in which the magnetic moment have been fixed to its theoretical value at 1.6 K. However with this constrain FullProf cannot reach the convergence. The result, for the nominal correction, is shown in figure 4.11. The red points are the observed intensities, the black line is the refined profile and the blue line is the difference between the observed and the calculated intensities. The peak at $2\theta = 20°$, which is purely magnetic, is strongly underestimated by a model in which the magnetic moment is not refinable. Due to the lack of convergence we let the magnetic moment refine.

We can now look at the main issue: compare the two possible magnetic structure. In figure 4.12 the refinement with Γ^9 magnetic structure is reported,

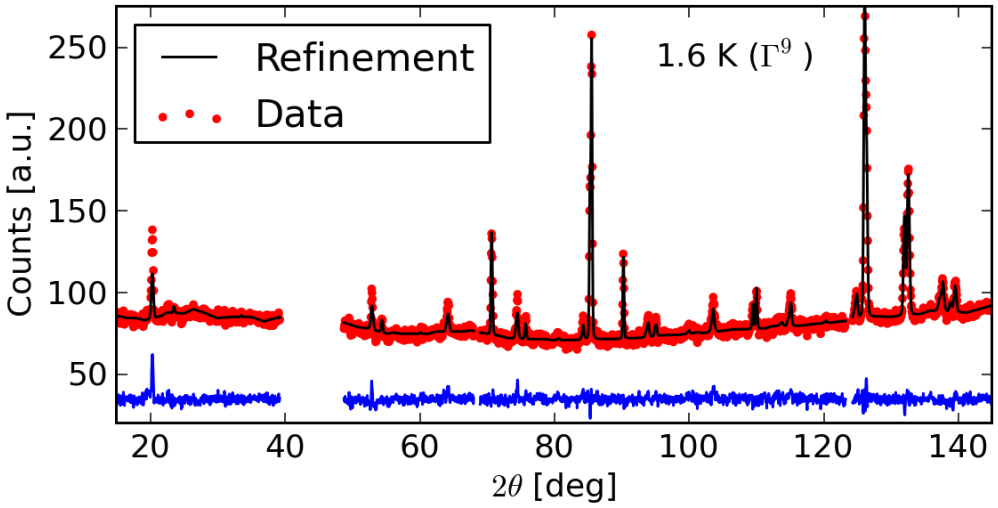

Figure 4.11: Rietveld refinement at 1.6 K with magnetic moment fixed to its theoretical value. The convergence is not reached and the magnetic contribution is underestimated as shown by the difference (blue line) between the observed intensities (red points) and the refined profile (black line).

whereas in figure 4.13 the refinement with Γ^6 magnetic structure is reported. Table 4.3 compare the most relevant refined paramenters. Both refinements are performed within the constrains defined previously: 1bov combination, magnetic moment refined, nominal correction. The agreement factors (global, crystallographic and magnetic) show a better agreement of Γ^9 representation than Γ^6 one. We can focus our attention to the magnetic Bragg factors, $R_{mag}(\Gamma^9) = 37.9$ and $R_{mag}(\Gamma^6) = 35.7$ which indicate a better agreement between the data and the spin ordering in plane. As explained in section 2.3, the differences between the intensity profile expected from the two different magnetic structure are mainly restricted to peaks located at 64° and 74°. In figure 4.14 and 4.15 the reflections of interest are shown. Consider the positions of the peaks at 64°. In the simulation presented in section 2.3 on page 16 it is shown that in the two proposed structures the positiosn of those peaks are shifted. In the case of spin ordering along the c-axis the peak is shifted on the left with respect to the case of a,b-plane ordering. Comparing the two refinements can be seen that in the Γ^6 representation the calculated profile is sistematically on the right with respect to the experimental data. This combined with the agreement factors analysis suggest that we are able to distinguish between the two magnetic structure. Moreover the results are

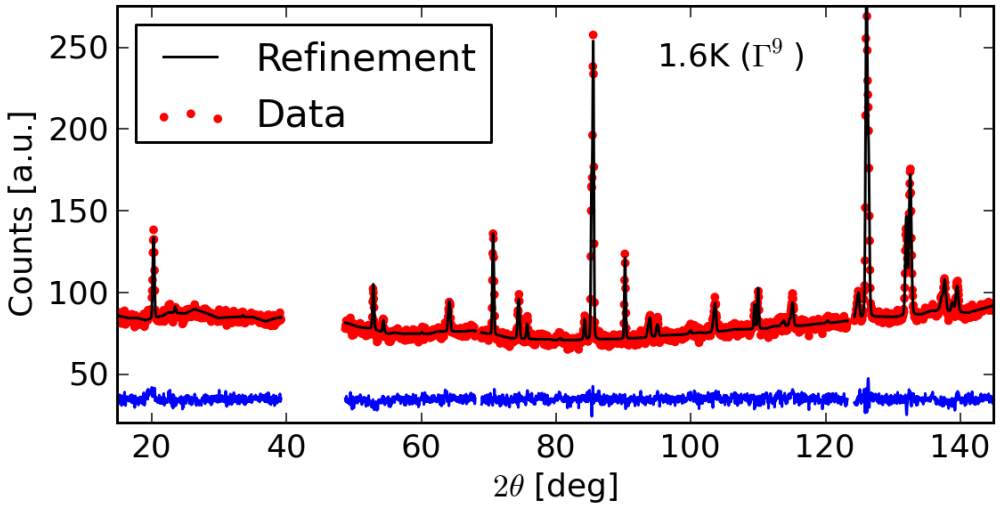

Figure 4.12: Rietveld refinement on $EuTiO_3$ powder diffraction at 1.6 K and Γ^9 ordering.

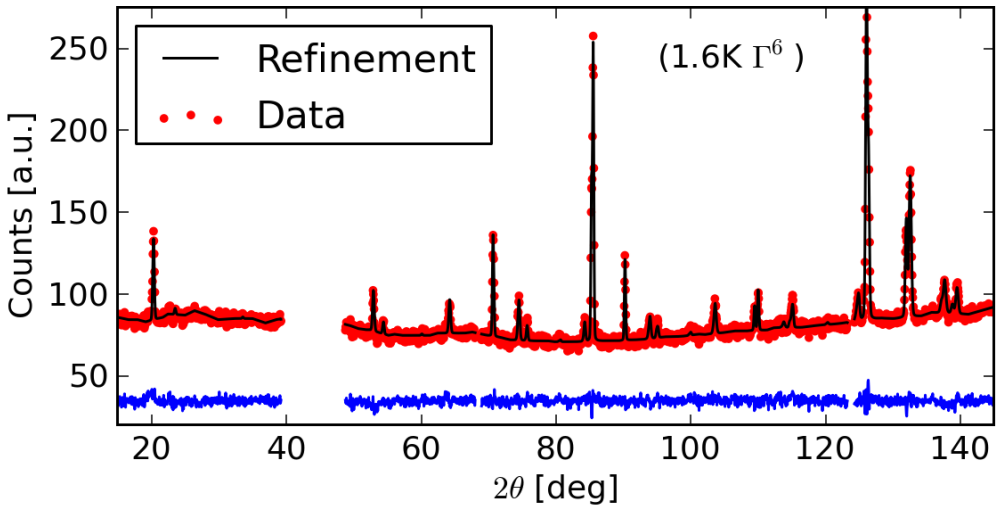

Figure 4.13: Rietveld refinement on $EuTiO_3$ powder diffraction at 1.6 K and Γ^6 ordering.

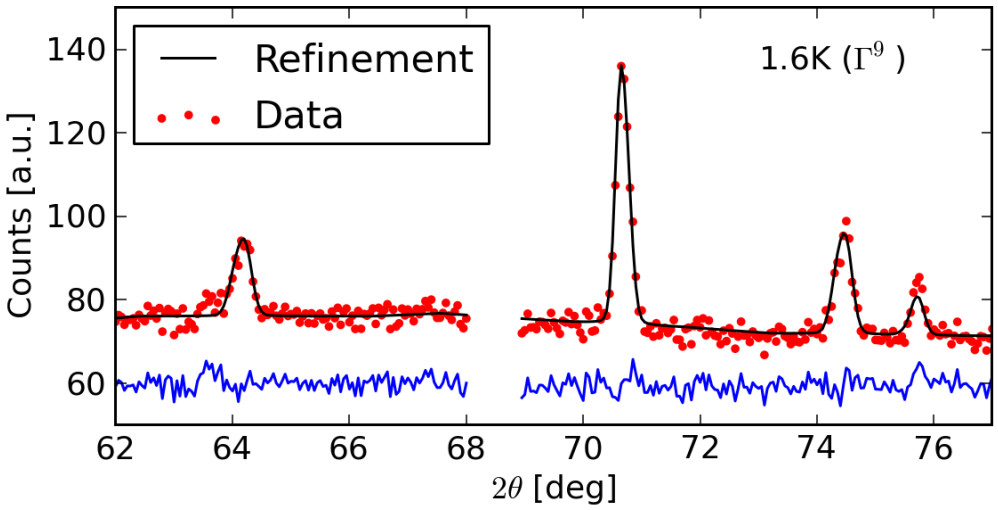

Figure 4.14: Rietveld refinement on $EuTiO_3$ powder diffraction at 1.6 K and Γ^9 ordering, enlargement on the region critical for the distinction between the two ordering model.

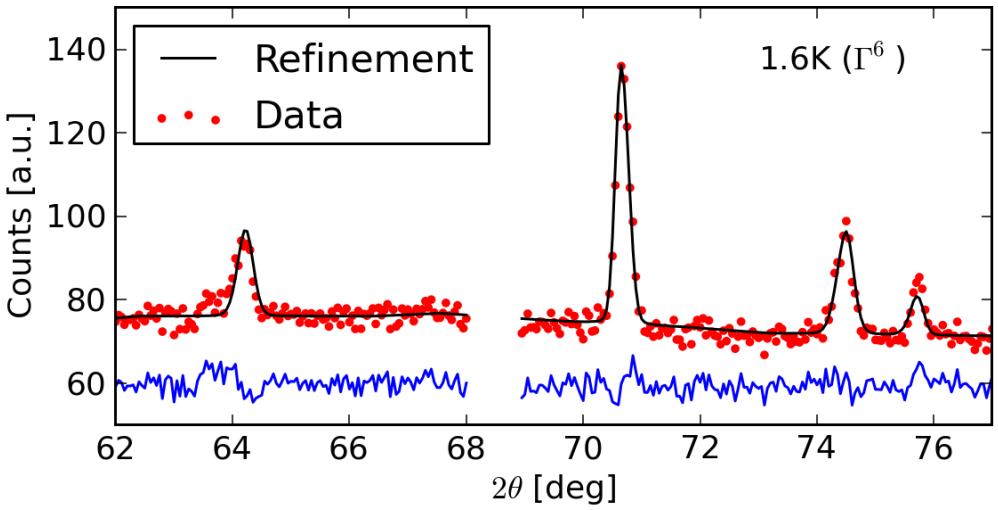

Figure 4.15: Rietveld refinement on $EuTiO_3$ powder diffraction at 1.6 K and Γ^6 ordering, enlargement on the region critical for the distinction between the two ordering model.

Magnetic structure	Γ^9	Γ^6
a (Å)	5.5069(3)	5.5077(4)
c (Å)	7.81298(5)	7.8141(5)
B_{iso} (Å^2)	0.12(3)	0.12(3)
$\mu(\mu_B)$	7.35	7.34
$R_B(cryst)$	8.48	8.60
$R_B(mag)$	35.7	37.9
χ^2_ν	1.83	1.88

Table 4.3: Refined structural and magnetic data of $EuTiO_3$, obtained from neutron powder diffraction at 1.6 K.

consistents with those reported in literature which all declare Γ^9 representation at 1.6 K.

4.3.3 3.5 K

We now discuss the 3.5 K data. In order to performe the refinements, we adopted the same strategies described for 1.6 K. We chose the 1bov combination and the nominal correction. The attempt of refining the data with the magnetic moment fixed at the value reported at 3.5 K failed ($\mu = 5.00\mu_B$)[5]. As shown in figure 4.16 the magnetic contribution is underestimated also at this temperature, therefore we let FullProf refine the magnetic moment. The Rietveld analysis has been performed for both the proposed spin ordering. In figure 4.17 and 4.18 the results are shown, whereas in table 4.4 the most important refined parameters are reported.

The overall agreement factor χ^2_ν shows a better agreement between the data and the Γ^9 model. The Bragg factor for the magnetic phase is lower for a, b-plane spin ordering than c-axis ordering. The bragg factor for the crystallographic phase are almost identical. The magnetic moment also in this case is higher than the expected value. Focusing again on the reflection located around 64° and 74°, shown in figure 4.19 and 4.20, we can see the better agreement between the calculated profile and the observed intesities in the case of Γ^9 model.

[5]The value of the magnetic moment at 3.5 K has been calculated as previously reported: assuming a critical exponent model and a value at 0 K equal to 7 μ_B

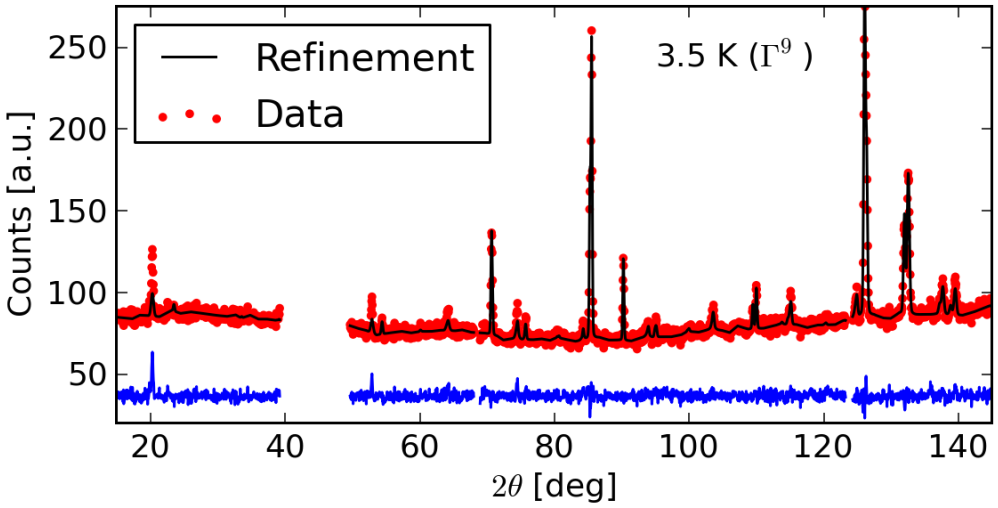

Figure 4.16: Retvield refinement at 3.5 K with magnetic moment fixed to its theoretical value. The convergence is not reached and the magnetic contribution is underestimated as shown by the difference (blue line) between the observed intensities (red points) and the refined profile (black line).

Magnetic structure	Γ^9	Γ^6
a (Å)	5.5056(3)	5.5063(4)
c (Å)	7.8110(5)	7.8120(5)
B_{iso} (Å^2)	0.17(3)	0.16(3)
$\mu(\mu_B)$	6.86	6.87
$R_B(cryst)$	6.17	6.18
$R_B(mag)$	23.6	25.7
χ^2_ν	1.46	1.49

Table 4.4: Refined structural and magnetic data of $EuTiO_3$, obtained from neutron powder diffraction at 3.5 K.

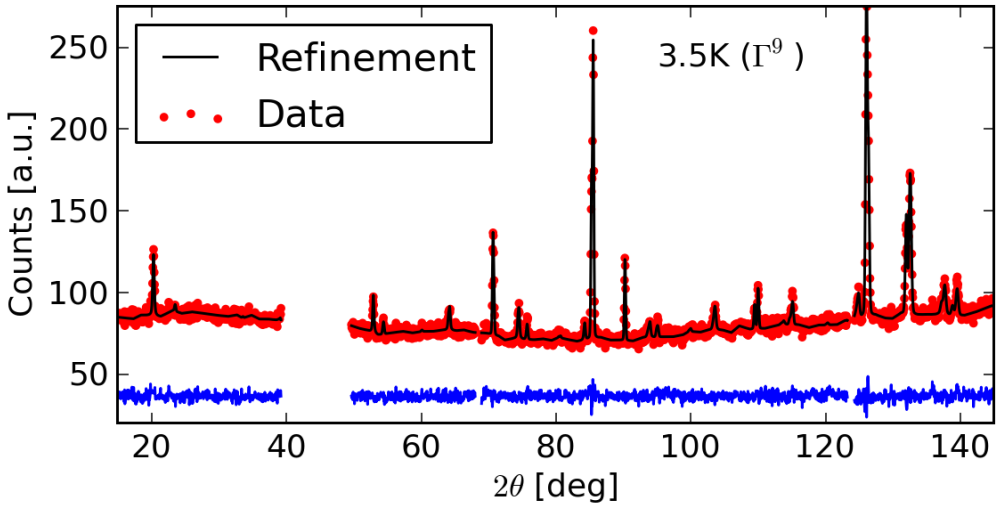

Figure 4.17: Rietveld refinement on $EuTiO_3$ powder diffraction at 3.5 K and Γ^9 ordering.

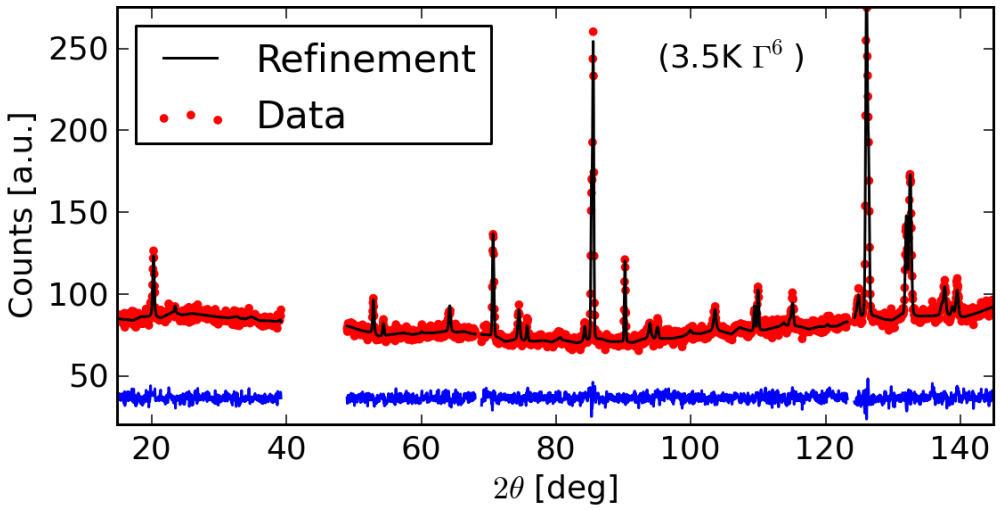

Figure 4.18: Rietveld refinement on $EuTiO_3$ powder diffraction at 3.5 K and Γ^6 ordering.

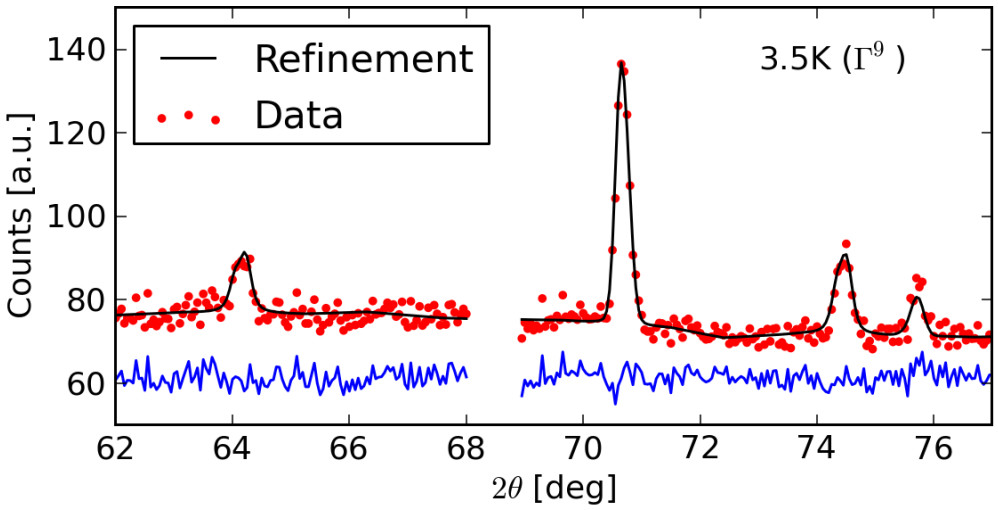

Figure 4.19: Rietveld refinement on $EuTiO_3$ powder diffraction at 3.5 K and Γ^9 ordering, enlargement on the region critical for the distinction between the two ordering model.

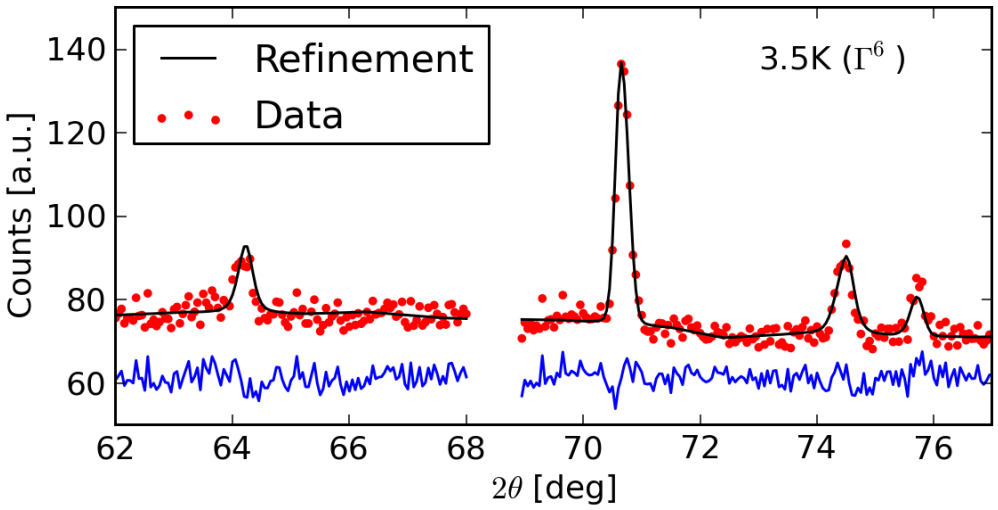

Figure 4.20: Rietveld refinement on $EuTiO_3$ powder diffraction at 3.5 K and Γ^6 ordering, enlargement on the region critical for the distinction between the two ordering model.

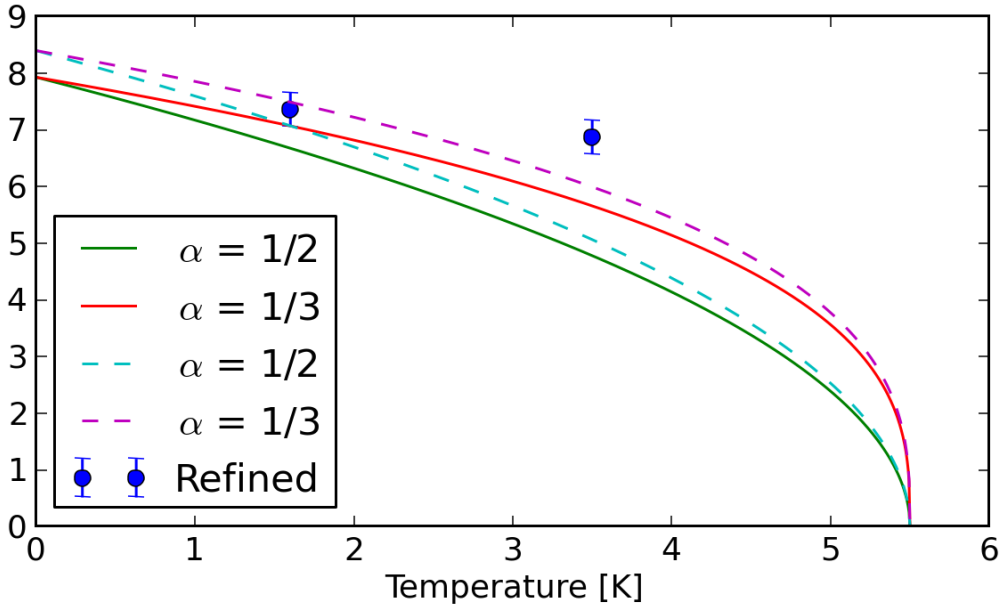

Figure 4.21: Refined and theoretical average magnetic moment as a function of temperature. Continuos lines are depicted assuming the value at zero temperature equal to the theoretical value ($7.93\mu_B$) and dashed lines assuming the value measured by SQUID ($8.4\mu_B$).

4.4 Magnetic moment temperature dependance

As previously discussed the magnetic moment obtained through the refinements are not consistent with those reported in literature. We systematically found values not compatible with a value of 7 μ_B at zero temperature. Despite of this, the magnetic characterization, reported at the beginning of the present chapter and the theoretical value calculated assuming a $4f^7$ configuration for the Eu ions with $S = 0$ and $J = \frac{7}{2}$, are consistent with the refined value. In figure 4.21 the comparison between the refined and the theoretical values are shown. The value of the magnetic moment at 0 K is set to $7.93\mu_B$ (theoretical value - continous line) and to $8.4\mu_B$ (SQUID value - dashed line), the Néel temperature (T_N) to 5.5 K. The curves of the magnetic moment are calculated for all the values between zero temperature and Néel temperature, accordingly to a critical exponent model. Two values for the critical exponent have been chosen: $\alpha = 1/2$ (mean field theory) and $\alpha = 1/3$ (experimentally observed)[55]. The black points indicates the refined values for the magnetic

moment at the two temperature studied. The refined values show a decrease of the magnetic moment with increasing temperature. While the magnetic moment at 1.6 K is in accordance with the model, the value at 3.5 K is higher. Only two points are unsufficient to determine the temperature dependence of the magnetic moment, but let us conclude that the value at zero temperature is around $8\mu_B$, and not, as previously reported, around $7\mu_B$.

Chapter 5

Conclusion and Prospect

$EuTiO_3$ raised our attention due to its magnetoelectric properties and a better understanding of these properties led us to study its magnetic phase diagram and especially to determine the magnetic structure in the case of zero applied magnetic field.

Neutron powder diffraction is still nowadays the most widely used technique to reveal the magnetic ordering in crystal, but in the case of our system the strong neutron absorption of Eu atoms had raised doubt on the possibility of using this technique. Despite of this we showed that NPD successfully allowed to determine the crystallographic and magnetic structure of $EuTiO_3$.

To overcome the absorption challenge, and reducing the counting time, we opted for a particular sample holder: the annular cylindrical sample holder. This geometry reducing the neutron path through the sample reduces the absorption and increases the signal detected. However this solution affects the intensity of the Bragg reflections with an angular dependence which is not implemented in the software used to solve the structure. This required the determination of a series of correction factors (as a function of the Bragg angle), which let the software correctly refines the data.

The absorption correction had been already studied and the results were known. The corrections were tabulated for discrete values of the absorption and geometrical parameters of the double walled sample holder, but the reported values does not fit our case. Therefore the correction factors tabulated had to be extended. We developed a new PYTHON code able to calculate the correction factors for absorption for any values of the parameters defining the case of the annular cylindrical sample holder. The code also generates a correction file which can be directly used as a FULLPROF input.

The code had been successfully applied to the case of $EuTiO_3$. However further developments can be suggested. The main limits of the solution we adopted are the computational time limit and the absence of an analytical form

of the correction as a function of the Bragg angle. Of course we performed a numerical calculation because the integration (which is the core of the absorption correction) cannot be carried out analytically. Despite of this the correction curves presented suggest the possibility of finding a suitable function which approximates the calculated correction. The code can now be used to investigate this possibility.

The absorption corrections obtained let us to perform a Rietveld refinements of the crystallographic and magnetic structure of $EuTiO_3$. We performed refinements using different correction curves compatible with the uncertainty on the parameters. We observed that a relatively small change in the absorption parameters could lead to a non negligible variation in the refined parameters, especially for those which strongly influence the angular dependence of the diffraction pattern, e.g. magnetic moment and thermal motion parameters. Therefore we conclude that the use of the correction for absorption must be done carefully. In order to reduce the uncertainty on the refined parameters it is crucial to reduce the uncertainty of the geometrical parameters of the double walled sample holder.

The Rietveld refinements on the neutron powder diffraction data confirm the crystal structure reported in literature (space group $I4/mcm$, at low temperature). The magnetic structure was investigated at 1.6 K and 3.5 K, in order to find confirmation of the proposed magnetic phase diagram. We found the data in agreement with a *in-plane* spin ordering at both temperature. We did not found any evidence of a spin ordering along the c-axis at 3.5 K.

The magnetic moment have been found higher than the value reported in literature, however the value obtain for $T = 1.6$ K is consistent both with the theoretical electronic configuration of Eu^{++} ion and the magnetic moment measured by SQUID.

We therefore showed that with the calculated absorption correction factors, the neutron powder diffraction technique, in a very high resolution mode, can be used to solve crystallographic and magnetic structure, also in the case of strongly neutron-absorbing sample.

Bibliography

[1] H. Wu and W.Z. Shen. Magnetoelectric effect in perovskite quantum paraelectric $EuTiO_3$. *Solid state communications*, 133(8):487–491, 2005.

[2] A. Bussmann-Holder, J. Köhler, R. K. Kremer, and J. M. Law. Relation between structural instabilities in $EuTiO_3$ and $SrTiO_3$. *Phys. Rev. B*, 83:212102, Jun 2011.

[3] Mattia Allieta, Marco Scavini, Leszek J. Spalek, Valerio Scagnoli, Helen C. Walker, Christos Panagopoulos, Siddharth S. Saxena, Takuro Katsufuji, and Claudio Mazzoli. Role of intrinsic disorder in the structural phase transition of magnetoelectric $EuTiO_3$. *Phys. Rev. B*, 85:184107, May 2012.

[4] Valerio Scagnoli, Mattia Allieta, Helen Walker, Marco Scavini, Takuro Katsufuji, Leyre Sagarna, Oksana Zaharko, and Claudio Mazzoli. $EuTiO_3$ magnetic structure studied by neutron powder diffraction and resonant x-ray scattering. *Phys. Rev. B*, 86:094432, Sep 2012.

[5] A. P. Petrović, Y. Kato, S. S. Sunku, T. Ito, P. Sengupta, L. Spalek, M. Shimuta, T. Katsufuji, C. D. Batista, S. S. Saxena, and C. Panagopoulos. Electric field modulation of the tetragonal domain orientation revealed in the magnetic ground state of quantum paraelectric $EuTiO_3$. *Phys. Rev. B*, 87:064103, Feb 2013.

[6] Kim Lefmann. Neutron scattering: Theory, instrumentation, and simulation. *University Course*, page 12, 2010.

[7] D2B website. `https://www.ill.eu/instruments-support/instruments-groups/instruments/d2b/description/instrument-layout/`.

[8] High-resolution diffractometers. `http://pd.chem.ucl.ac.uk/pdnn/inst3/diff1.htm`.

[9] Frederick Nye et al. *Physical properties of crystals.* Clarendon Press Oxford, 1964.

[10] Nicola A. Spaldin and Manfred Fiebig. The renaissance of magnetoelectric multiferroics. *Science*, 309(5733):391–392, 2005.

[11] W. Eerenstein, N.D. Mathur, and J.F. Scott. Multiferroic and magnetoelectric materials. *Nature*, 442(7104):759–765, 2006.

[12] A.J. Millis. Lattice effects in magnetoresistive manganese perovskites. *Nature*, 392(6672):147–150, 1998.

[13] Pierre Curie. Sur la symétrie dans les phénomènes physiques, symétrie d'un champ électrique et d'un champ magnétique. *J. Phys. Theor. Appl.*, 3(1):393–415, 1894.

[14] Dzyaloshinskii. On the magneto-electrical effects in antiferromagnets. *Zh. Eksp. Teor. Fiz.*, 37:881–985, 1959.

[15] D. N. Atrov. The magnetoelectric effect in antiferromagnetics. *Zh. Eksp. Teor. Fiz.*, 38:984–985, 1960.

[16] Hans Schmid. Introduction to the proceedings of the 2nd international conference on magnetoelectric interaction phenomena in crystals, MEIPIC-2. *Ferroelectrics*, 161(1):1–28, 1994.

[17] S. L. Hou and N. Bloembergen. Paramagnetoelectric effects in $NiSO_4 \cdot 6H_2O$. *Phys. Rev.*, 138:A1218–A1226, May 1965.

[18] H. Grimmer. The piezomagnetoelectric effect. *Acta Crystallographica Section A*, 48(3):266–271, May 1992.

[19] Sang-Wook Cheong and Maxim Mostovoy. Multiferroics: a magnetic twist for ferroelectricity. *Nature materials*, 6(1):13–20, 2007.

[20] Ram Seshadri and Nicola A Hill. Visualizing the role of bi 6s "lone pairs" in the off-center distortion in ferromagnetic $BiMnO_3$. *Chemistry of materials*, 13(9):2892–2899, 2001.

[21] T. Kimura, S. Kawamoto, I. Yamada, M. Azuma, M. Takano, and Y. Tokura. Magnetocapacitance effect in multiferroic $BiMnO_3$. *Physical Review B*, 67(18):180401, 2003.

[22] J.F. Scott, R. Blinc, et al. Multiferroic magnetoelectric fluorides: why are there so many magnetic ferroelectrics? *Journal of physics. Condensed matter: an Institute of Physics journal*, 23(11):113202, 2011.

[23] Isaac B. Bersuker. Pseudo jahn-teller origin of perovskite multiferroics, magnetic-ferroelectric crossover, and magnetoelectric effects: The $d^0 - d^{10}$ problem. *Phys. Rev. Lett.*, 108:137202, Mar 2012.

[24] T. Kimura, T. Goto, H. Shintani, K. Ishizaka, T. Arima, and Y. Tokura. Magnetic control of ferroelectric polarization. *Nature*, 426(6962):55–58, 2003.

[25] T. Katsufuji, S. Mori, M. Masaki, Y. Moritomo, N. Yamamoto, and H. Takagi. Dielectric and magnetic anomalies and spin frustration in hexagonal $RMnO_3$ (r=y, yb, and lu). *Phys. Rev. B*, 64:104419, Aug 2001.

[26] E.J.W. Verwey and P.W. Haayman. Electronic conductivity and transition point of magnetite ("Fe_3O_4"). *Physica*, 8(9):979–987, 1941.

[27] A.M.J.G. Van Run, D.R. Terrell, and J.H. Scholing. An in situ grown eutectic magnetoelectric composite material. *Journal of Materials Science*, 9(10):1710–1714, 1974.

[28] Ce-Wen Nan, M. I. Bichurin, Shuxiang Dong, D. Viehland, and G. Srinivasan. Multiferroic magnetoelectric composites: Historical perspective, status, and future directions. *Journal of Applied Physics*, 103(3), 2008.

[29] T.R. McGuire, M.W. Shafer, R.J. Joenk, H.A. Alperin, and S.J. Pickart. Magnetic structure of $EuTiO_3$. *Journal of Applied Physics*, 37(3):981–982, 1966.

[30] T Katsufuji and H Takagi. Coupling between magnetism and dielectric properties in quantum paraelectric $EuTiO_3$. *Physical Review B*, 64(5):054415, 2001.

[31] Hua Wu, Qing Jiang, and Wen Zhong Shen. Coupling between the magnetism and dielectric properties in $EuTiO_3$. *Phys. Rev. B*, 69:014104, Jan 2004.

[32] Koji Fujita, Naoki Wakasugi, Shunsuke Murai, Yanhua Zong, and Katsuhisa Tanaka. High-quality antiferromagnetic $EuTiO_3$ epitaxial thin films on $SrTiO_3$ prepared by pulsed laser deposition and postannealing. *Applied Physics Letters*, 94(6):062512–062512, 2009.

[33] Craig J. Fennie and Karin M. Rabe. Magnetic and electric phase control in epitaxial $EuTiO_3$ from first principles. *Phys. Rev. Lett.*, 97:267602, Dec 2006.

[34] June Hyuk Lee, Lei Fang, Eftihia Vlahos, Xianglin Ke, Young Woo Jung, Lena Fitting Kourkoutis, Jong-Woo Kim, Philip J Ryan, Tassilo Heeg, Martin Roeckerath, et al. A strong ferroelectric ferromagnet created by means of spin-lattice coupling. *Nature*, 466(7309):954–958, 2010.

[35] Farrel W Lytle. X-ray diffractometry of low-temperature phase transformations in strontium titanate. *Journal of Applied Physics*, 35(7):2212–2215, 1964.

[36] J. Brous, I. Fankuchen, and E. Banks. Rare earth titanates with a perovskite structure. *Acta crystallographica*, 6(1):67–70, 1953.

[37] D.L. Janes, R.E. Bodnar, and A.L. Taylor. Europium barium titanate—a magnetic ferroelectric compound. *Journal of Applied Physics*, 49(3):1452–1454, 1978.

[38] C.J. Howard and H.T. Stokes. Group-Theoretical Analysis of Octahedral Tilting in Perovskites. *Acta Crystallographica Section B*, 54(6):782–789, Dec 1998.

[39] Christopher J. Howard and Harold T. Stokes. Structures and phase transitions in perovskites – a group-theoretical approach. *Acta Crystallographica Section A*, 61(1):93–111, Jan 2005.

[40] E.F. Bertaut. Magnetic structure analysis and group theory. *Le Journal de Physique Colloques*, 32(C1):462, 1971.

[41] J Rodriguez-Carvajal. BASIREPS-a program for calculating non-normalized basis functions of the irreductible representations of the little group gk for atom properties in a crystal, 2004.

[42] Gordon Leslie Squires. *Introduction to the theory of thermal neutron scattering*. Cambridge University Press, 2012.

[43] Neil W. Ashcroft and N. David Mermin. Solid state phys. *Saunders, Philadelphia*, 1976.

[44] D.F. Johnston. On the theory of the electron orbital contribution to the scattering of neutrons by magnetic ions in crystals. *Proceedings of the Physical Society*, 88(1):37, 1966.

[45] A.W. Hewat. D2b, a new high resolution neutron powder diffractormeter at ill grenboble. In *Materials Science Forum*, volume 9, pages 69–80. Trans Tech Publ, 1986.

[46] E. Suard and A. Hewat. The super-d2b project at the ill. *Neutron News*, 12(4):30–33, 2001.

[47] H.M. Rietveld. A profile refinement method for nuclear and magnetic structures. *Journal of applied Crystallography*, 2(2):65–71, 1969.

[48] Juan Rodríguez-Carvajal. Recent advances in magnetic structure determination by neutron powder diffraction. *Physica B: Condensed Matter*, 192(1):55–69, 1993.

[49] T. Roisnel and J. Rodriguez-Carjaval. Fullprof manual, 2000.

[50] C.W. Dwiggins. Analytical solution for the x-ray absorption factor for cylinders in two special cases. *Acta Crystallographica Section A: Crystal Physics, Diffraction, Theoretical and General Crystallography*, 28(2):219–220, 1972.

[51] C.W. Dwiggins. Rapid calculation of x-ray absorption correction factors for cylinders to an accuracy of 0.1%. *Acta Crystallographica Section A: Crystal Physics, Diffraction, Theoretical and General Crystallography*, 31(1):146–148, 1975.

[52] D. Schmitt and B. Ouladdiaf. Absorption correction for annular cylindrical samples in powder neutron diffraction. *Journal of applied crystallography*, 31(4):620–624, 1998.

[53] Id15 website. `http://www.esrf.eu/UsersAndScience/Experiments/StructMaterials/ID15`.

[54] Jérôme Kieffer and Dimitrios Karkoulis. Pyfai, a versatile library for azimuthal regrouping. In *Journal of Physics: Conference Series*, volume 425, page 202012. IOP Publishing, 2013.

[55] Roberto Piazza. *Note di fisica statistica*. Springer, 2011.

Acknowledgments

La mia riconoscenza va innanzitutto al Prof. Giacomo Ghiringhelli, che primo mi ha accettato nel suo gruppo offrendomi l'opportunità di svolgere quel percorso che qui si compie. Al dott. Claudio Mazzoli, che mi ha accompagnato, vanno la mia stima ed il mio ringraziamento. Gli esperimenti insieme condotti, i confronti e la sua guida nel corso di questo cammino mi hanno permesso di scoprire un modo nuovo e diverso di imparare. Rivolgo un ringraziamento anche al dott. Marco Scavini ed a Mauro Coduri e Paolo Masala dell'Università degli Studi di Milano. Preziosi sono stati i loro consigli e formativo è stato collaborare con loro. Un ringraziamento è altresì destinato alla dott.ssa Emmanuelle Suard ed a tutto lo staff di D2B. Vorrei ringraziare inoltre la dott.ssa Chiara Pernechele per le preziose misure di magnetometria effettuate sul nostro campione. Infine vorrei rivolgere un attestato di stima a tutti coloro che ho incontrato in questo percorso e che, con la loro testimonianza, mi hanno insegnato cosa significhino la dedizione e la passione per la ricerca scientifica.

A mamma e papà. Alla mia famglia a cui questo lavoro è dedicato. Dall'infanzia mi hanno condotto per mano fino a questo traguardo. Ora sta a me.

Ai colleghi del Politecnico, amici con cui ho condiviso gioie e fatiche del percorso di vita e di studi in questi anni. Agli amici che mi hanno accompagnato ed alle guide che ho fino ad oggi incontrato. Grazie.